An Experimental Investigation of the Near Surface Flow Structure over Wind-Sheared Water Surface

Nasiruddin Shaikh

A Thesis

In the Department

Of

Mechanical and Industrial Engineering

Presented in Partial Fulfillment of the Requirements

For the Degree of Doctor of Philosophy (Mechanical Engineering) at

Concordia University

Montreal, Quebec, Canada

December 2008

Your file Votre référence
ISBN: 978-0-494-45678-1
Our file Notre référence
ISBN: 978-0-494-45678-1

ABSTRACT

An Experimental Investigation of the Near Surface Flow Structure over Wind-Sheared Water Surface

Nasiruddin Shaikh, Ph. D.

Concordia University, 2008

The study of airside flow structure and its interaction with water at the air-water interface is important in order to understand the exchange of momentum, heat and mass fluxes between the two mediums. The present dissertation deals with the quantitative investigation of the near-surface flow above wind-sheared water surface through a series of laboratory experiments conducted over a wind speed range of 1.5 m s^{-1} to 4.4 m s^{-1} and at a fetch of 2.1 m. The two-dimensional velocity fields were measured using particle image velocimetry (PIV). To compare the airflow structure over the water surface with that over solid wall, the measurements were also made over the smooth and wavy walls at the same location, under identical conditions.

The results show a reduction in the mean velocity magnitudes and the tangential stresses when gravity waves appear on the water surface. An enhanced vorticity layer was observed immediately above the water surface that extended to a height of approximately two times of the significant wave height. A novel approach is used to separate the wave-induced component from the instantaneous velocity fields. The flow structure was analyzed as a function of wave phase. The phase-averaged profiles of wave-induced

velocity, vorticity and Reynolds stress showed different behaviour on the windward and leeward sides of the wave in the near-surface region. The results also show that the turbulent Reynolds stress mainly supports downward momentum transfer whereas the wave-induced Reynolds stress is responsible for the upward momentum transfer from wave to wind.

This dissertation also provides first quantitative comparison of the mean, wave-induced and turbulent properties for the separated and non-separated flows over wind generated water waves. The maximum difference between the flow characteristics of the separated and non-separated flows is observed on the leeward side, within core of the separation region, where, higher magnitudes of the vorticity and turbulent properties were observed, indicating that the turbulence is significantly enhanced within the separation region.

The comparison of the flow over smooth and wavy water and solid surfaces showed that although the trends in profiles over water and solid surfaces are mostly similar, the relative magnitudes of turbulent properties and their level of enhancement towards the surface are different over water and solid surfaces. Thus, the models for the flow over solid surfaces may not accurately predict the flow properties over the water surface especially in the near-surface region.

AKNOWLEDGEMENTS

I consider myself extremely fortunate to have worked under the supervision of Dr. Kamran Siddiqui. He guided me through the difficult stages of this research. I have gained valuable research experience and significantly improved my technical skills under his supervision. I am truly thankful to him for all his ideas, support and enthusiasm for this work.

Thanks also go to my examining committee members, Dr. Abdel Razik Sebak, Dr. Wahid S. Ghaly and Dr. Marius Paraschivoiu for their questions, valuable suggestions and contribution to this thesis.

I also like to express the warmest thanks to my friends, Majid, Shaheen and Jamil, helped with numerous essential details along the way. The technical assistance provided by the department's technical staff specially, Brain Cooper, Gilles Huard and William Wong are also appreciated.

I sincerely thank my parents and wife for never-ending encouragement they have given to me. I could not have made it to the end without their help and support.

TABLE OF CONTENTS

LIST OF FIGURES

LIST OF TABLES

NOMENCLATURE

c	Wave-phase speed
L_1, L_2, L_3, L_4	Four segments of a wave
N_t	Total number of wave profiles
N_{zc-1}	Number of wave profiles having one zero crossing
N_{zc-2}	Number of wave profiles having two zero crossings
N_{zc-3}	Number of wave profiles having three zero crossings
N_{zc-m}	Number of wave profiles having more than three zero crossings
N_{zc-0}	Number of wave profiles having no zero crossing
N_{ph}	Number of wave profiles used to compute the phase averaged properties
N	Number of wave profiles contain crest-to-trough region,
$N_{0.6}$	Number of separated velocity fields having wave slope greater than or equal to 0.6
$N_{0.4-0.6}$	Number of velocity fields having wave slope greater than 0.4 and less than 0.6
$N_{0.4}$	Number of velocity fields having wave slope less than or equal to 0.4

$n_{0.4-0.6}$	Number of separated velocity fields having wave slope greater than 0.4 and less than 0.6
S_{max}	Maximum wave slope
U_{∞}	Free stream velocity
U_{10}	Velocity measured at a height of 10 m
U_s	Surface velocity
u	Instantaneous streamwise velocity
u_*	Friction velocity
$\tilde{u}$	Streamwise component of wave-induced velocity
$\tilde{v}$	Vertical component of wave-induced velocity
v	Vertical component of instantaneous velocity
$-\overline{u_f v_f}$	Total Reynolds stress
$-\overline{\tilde{u}\tilde{v}}$	Wave-induced Reynolds stress
$-\overline{u'v'}$	Turbulent Reynolds stress
$\frac{dU}{d\xi}$	Streamwise velocity gradient
$d\eta/dx$	Gradient of the wave surface displacement
u^+ and y^+	Non-dimensional wall coordinates

GREEK SYMBOLS

μ	Dynamic viscosity of air
ξ	Vertical coordinate with reference to the fluctuating water surface
λ	Wave length
θ	Wave phase angle
ε	Turbulent energy dissipation
σ	Standard deviation
ν_a	Kinematic viscosity of air
η	Water surface displacement
ω	Vorticity
τ_w	Wave-induced stress
τ_t	Turbulent stress
τ_s	Surface tangential stress
τ_v	Tangential stress
ε_u	Errors associated with the streamwise velocity.

CHAPTER 1

Introduction

The study of airside flow structure and its interaction with water at the air-water interface is important in order to understand the exchange of momentum, heat and mass fluxes between the two mediums. The physical interaction between air and water involves a number of complex phenomena, occurring on both air and water sides, in the close vicinity of the interface. The momentum transfer from air drifts the water current and produces surface waves and underwater turbulence. The wind-generated water waves are the distinctive feature at the air-water interface. The oscillatory motion of the waves generates wave field and turbulence in the near surface region on both sides of the interface which influence the wind and water fields. The modified near surface turbulence plays a significant role in transferring momentum, heat and mass across the air-water interface.

Understanding and proper parameterization of the exchange processes across the air-water interface are of obvious relevance for wave prediction models, climate modeling, weather forecasting, environmental impact studies, storm-surge modeling and many other important applications (Grachev and Fairall 2000, Janssen 1989). To-date, in the environmental applications, oceanographers and meteorologists often ignore the near surface turbulence and considered this region as a black box (Edson et al. 1999). They estimate the air-sea energy exchange from the airside properties measured at a reference height of 10 m above the mean water level and assume that there is no significant

variation in the air properties within this height (Qiu and Hacker 2004). This assumption is not realistic. Some of the studies focused on the near surface waterside flow, showed that the turbulence and other flow parameters change significantly within a region adjacent to the interface whose depth is of the order of 1 cm (Siddiqui et al. 2001). Furthermore, the variation of these flow parameters in this region is non-linear (Siddiqui and Loewen 2007). If the same analogy is applied on airside, then it can be argued that understanding of the influence of surface waves on the airflow structure immediately above the water surface is necessary to obtain reliable estimates of air-water fluxes (Chambers and Antonia 1980). This will also lead to the improvement of existing models for accurate forecasting of global climate.

The mechanism of momentum transfer within the boundary layer over the water surface is somewhat different from that over the solid wall (Hare et al. 1997). One of the major differences is the hydrodynamic boundary condition which is non-zero at the air-water interface and zero at the solid wall. Another difference is the dynamic wave field at the air-water interface. The surface waves create dynamic roughness over the water surface. It is obvious that the modified airflow structure over the fluctuating water surface is mainly due to the roughness created by the waves, but it has been difficult to relate the water surface roughness to the roughness of the solid wall. Does the blowing air behave the same over the water surface of variable roughness as it does over the solid surface of constant roughness? Our current knowledge is not sufficient enough to answer this question.

A substantial amount of experimental data exists for the turbulent flow over solid walls and has resulted in well developed empirical relations describing different turbulent characteristics in the near wall region. These relationships are often used to estimate the desired turbulent quantities over the water surface where direct measurement is very difficult. However the use of these empirical relations for the flow over the water surface is questionable (Perry et al. 1987). Csanady (1984) argued that the wall layer analogy can only be used outside the wave boundary layer where, the wave-induced effects are negligible.

Obukhov (1946) and Monin and Obukhov (1954) were the first to describe a similarity hypothesis. The similarity hypothesis states that various turbulent statistics, when normalized by the scaling parameters are universal function of the stability parameter. The application of Monin-Obukhov similarity theory to the water surface requires caution because the scaling parameters derived for the flow over solid surface, only accounts shear-driven and buoyancy-driven turbulence. As stated above, the fluctuating water surface creates oscillatory movement in the air. This vertical oscillation causes stretching and changes the direction of the turbulent velocity (Mete et al. 2002). Therefore, additional scaling parameters are required to describe turbulence over the water surface (Hidy and Plate 1966).

The study of the flow structure immediately above the wavy water surface is very challenging. One of the key issues is the accurate description of the waveform of individual waves that vary spatially as well as temporally. Although the study of the airflow structure over the water surface has been a subject for the last 50 years but the process of mass, heat and momentum exchange across the air-water interface is still not

well quantified. This is attributed to the measurement difficulties, especially in the near surface region between the wave crest and trough, where any particular spatial location lies sometimes in water and sometimes in air.

1.1. Background

Several laboratory studies have been conducted to study airside velocity fields above water waves. Majority of these studies used point measurement techniques which did not allow measurements within the fluctuating region of the air-water interface i.e. the region bounded between the crest and trough and thus, put limitations on capturing the near-surface dynamics. For example Banner and Melville (1976) and Mete et al. (2002) measured wind speed in laboratory experiments, at a height of 10 cm above the mean water surface, using a Pitot-static tube and hot-film anemometer respectively. Hidy and Plate (1966) measured the air velocity above wind waves at the height of 20 cm above the mean water level at wind speeds ranging from 6 m s^{-1} to 14 m s^{-1} and at various fetches ranging from 2.15 to 11.9 m. When the measurement probe is placed at a fix position, it measures the parameter (typically velocity, pressure and temperature) at a certain height from the mean water level. The surface values are typically obtained through linear extrapolation. However, due to the nonlinear behaviour of the waves, the airflow structure immediately above the interface exhibits high level of fluctuations as a result the measured parameters vary nonlinearly in this region. Therefore, the linear extrapolation could result in over or underestimation of the surface characteristics. This indicates that

the measurements taken far from the interface cannot provide accurate estimation of the near surface flow behaviour above the waves.

To avoid the uncertainty incorporated in the data extrapolated to the surface, some researchers had used wave-follower system and took the measurements at a constant height from the fluctuating water surface. The wave-follower typically consists of an over hanged platform that moves up and down with a water level sensor, installed at the lower end of the platform. The measuring probe is mounted on the platform. An electric motor gets the signals from the water level sensor and drives the platform such that it maintains a constant distance between the probe and the fluctuating water surface. The wave-follower system could provide quantitative measurements at a point within the crest-trough region at the fluctuating air-water interface. However when the instrumentation follows the surface other problems arise, which includes, mechanical vibration and acoustic waves. In addition, their point measurement nature makes full field velocity mapping very cumbersome. Kawamura and Toba (1988) reported that the wave follower could not perfectly follow waves especially at the forward face of the wave crest. Papadimitrakis et al. (1986b) observed that the wave follower generates acoustic waves that travel in both upstream and downstream directions, which contaminate the measured data. They concluded that neglecting the acoustic contamination leads to errors in the momentum and energy exchange between 18-32%.

Researchers have used flow visualization techniques to qualitatively describe the instantaneous spatial structure of the airflow field within and above the crest-trough region. The visual inspections showed that the airflow structure within the near-surface

region is different from the flow structure at greater heights. The dynamical processes in the near-surface region include airflow separation immediately adjacent to the water surface (Kawai 1981), coherent structures (Komori et al. 1993), a high shear layer and active bursting and sweeping phenomena (Kawamura and Toba 1988). However the evidence of the existence of these dynamical processes is mainly based on the qualitative observations.

With the availability of the state-of-the-art particle image velocimetry (PIV) technique, most of the difficulties associated with point measurement devices have been overcome. PIV is a non-intrusive, optical measurement technique capable of measuring velocities in a plane simultaneously at thousands of points in the flow field. Some researchers have used PIV technique to measure the instantaneous flow field within the crest-trough region of the wind-generated water waves. For example Peirson (1997), Peirson and Banner (2003), Siddiqui et al. (2001), and Siddiqui and Loewen (2007) described the waterside flow structure beneath wind waves. Whereas Reul et al. (1999), Veron et al. (2007), Reul et al. (2008) reported airside flow field immediately above the waves using PIV. A common observation in all of the above PIV studies is that the near surface flow dynamics are complex and significantly different from that observed at greater heights. The PIV studies above the waves discussed the dynamics of instantaneous velocity and vorticity structures in the near surface flow however they did not present the detailed mean and turbulent flow structure above the waves particularly in the near-surface region.

The present study is focused on conducting a detailed quantitative analysis of the airside flow structure above the wind-sheared water surface, especially within the crest-

trough region, to improve our knowledge of the flow dynamics in this region. PIV technique was used to measure the airside velocity field. To the best of our knowledge this is the first study, reporting the quantitative analysis of the airflow structure in the immediate vicinity of the air-water interface, which will lead to a better understanding of the air-water mass, heat and momentum exchange.

1.2. Literature Review

One of the challenging tasks in the field of fluid mechanics is the understanding of the flow dynamics above and below the fluctuating air-water interface especially in the presence of surface waves. Due to the challenging nature, not enough work has been done in the near surface region on both sides of the interface, especially on the airside. As a result no accurate model for the momentum, mass and heat transfer has been developed yet. Furthermore, the limited analytical and experimental work reported in the literature describing the airside processes shows large discrepancy in the results. In this section, the relevant literature on the different aspects studied in this dissertation is reviewed. The previous studies on the analytical, and experimental studies carried out in the field and laboratory are presented.

1.2.1. Theoretical investigations

Miles (1957) and Phillips (1957) were the pioneers in the field of wind-wave interaction. They presented physical models explaining the momentum and energy

exchange between waves and airflow. Miles (1957) proposed a quasi-laminar model that describes the process of momentum transfer from wind to waves. In his model, the turbulence in the air stream was neglected except in maintaining a prescribed parallel shear flow with the logarithmic velocity distribution. The model was tested through field and laboratory experiments and it was concluded that the momentum exchange process between the air and wind waves is somewhat different from Miles' (1957) model (Ichikawa and Imasato 1976). Phillips (1957) in his theoretical model described that the airside velocity and pressure fluctuations at the air-water interface are associated with the atmospheric turbulence and independent of the wave generation. However, this hypothesis failed for large amplitude waves (Lai and Shemdin 1971). Makin et al. (1994) introduced an analytical model that includes both the impact of waves and wind speed on the momentum flux, and covered the entire range from developing sea to fully developed wave. They used mixing length model to parameterize the turbulent stress whereas wave-induced stress was model by considering all undulations of the interface as waves. They concluded that gravity capillary waves have minor contribution to the momentum exchange and most of the momentum is transferred to the long waves. In continuation of Miles' theory, Janssen (1989) considered the effect of gravity waves and modeled the effect of air turbulence using mixing length model. He argued that young waves ($c < 5u_*$, where, c is the wave-phase speed and u_* is the friction velocity) have strong coupling with wind, while old waves ($c \geq 5u_*$) have no such coupling.

Theoretical models available in the literature show substantial disagreement. To date none of them are proved to be the true representative of the actual process of

momentum and energy exchange between the two mediums. For improved modeling of wind-wave interactions, additional experimental data especially in the near surface region is necessary.

1.2.2. Field Experiments

Benilov et al. (1974) simultaneously measured the fluctuations of wind velocity and wave-elevation using acoustic anemometer and resistance-wire wave gauge, respectively. The experiments were conducted in the Caspian Sea and the data was recorded at the mean wind speeds of 6 and 13 m s^{-1}. They analyzed the spectra of velocity fluctuations at a height of 2.45 m from the mean sea level and for different stages of the wave development. They observed 15% reduction in the downward momentum flux for the developed waves compared to the developing waves, and attributed this change to the wave-induced stress.Antonia and Chambers (1980) analyzed the spectra and co-spectra of streamwise and vertical velocity fluctuations that were measured in the Bass Strait, at a height of 5 m from the mean sea level. The measurements were performed at wind speeds ranging from 5.31 to 9.38 m s^{-1}. Hot-wire anemometer and an array of Gill propellers were used to measure streamwise and vertical velocity fluctuations respectively, whereas the instantaneous sea surface displacement was recorded using the resistance-wire gauge. When $c/u_* > 40$, they observed negative spikes in the cross-spectrum of streamwise and vertical velocity fluctuations and consider these spikes as upward momentum transfer from wave to wind. Wetzel (1996) reported wind velocity and wave height data that was measured in the North Pacific Ocean. The measurements were made at heights 8.7 m and

above the mean sea level at the mean wind speed of 15 m s^{-1} and mean waves height of 6 m. He observed a strong correlation between the horizontal component of the instantaneous wind velocity and the wave height. He also observed significant upward momentum transfer from decaying waves and downward momentum transfer to developing waves and concluded that the upward momentum transfer from waves to wind is only associated with fully developed waves. He also argued that the direction of momentum flux strongly depends on the wave age. Some other field observations also indicated an upward transport of momentum for the developed waves based on the spike in the co-spectra of horizontal and vertical velocity fluctuations observed around the peak frequency (e.g. Volkov 1970 and Davidson and Frank 1973).

1.2.3. Laboratory Experiments

The oscillatory motion of the waves modulates the structure of the airflow field above them and therefore, it is different from that over a solid surface. (Grachev and Fairall 2000). The wave-induced velocity quantifies the contribution of the wave motion to the flow field and provides fundamental understanding about the flow pattern induced in the near surface region, immediately above the waves. Wave-induced motion has been studied in several laboratory experiments. Harris (1966) was the first who reported that surface waves induce airflow in the region close the interface. He photographed the movement of smoke over mechanically-generated water waves in the absence of wind for three different tank sizes. The visualization through individual puffs of smoke showed that for all cases, the smoke puffs drifted slowly over the troughs and jumped quickly

over the crests. He also observed that the rate of dissipation of the individual puff was increased with the wave steepness and wave height. He concluded that the wave-driven wind is not the result of the viscous drag, and the underlying physical mechanism could be studied without considering the molecular viscosity. Kawamura and Toba (1988) visualized the airflow structure in the turbulent boundary layer over wind-generated waves using liquid paraffin mist that was introduced near the water surface. They observed large-scale ordered motion in the outer part of the boundary layer. They also observed the bursting phenomena and separation bubbles on windward and leeward sides of the wave crest. They attributed the airflow separation and large-scale motions of air bulges as the fundamental mechanisms for the bursting process. Komori et al. (1993) investigated the flow structure on both sides of the interface in a laboratory wind wave flume. To visualize the airflow, paraffin mist was fed over the waves. For the waterside flow visualization, fluorescent sodium dye was used. They observed organized motions in the airflow that appeared intermittently in front of the wave crest which generated an upward accelerated bulge of smoke. On the waterside, the surface renewal eddies were observed at the same location where the organized motion occurred in the air.

Point measurement devices such as hot-wire, hot-film, pitot tube, are used to measure the flow field above waves. Takeuchi et al. (1977) measured horizontal and vertical components of the airflow over mechanically-generated water waves at a fetch of 13 m, using a hot-film anemometer. Data were recorded at the heights ranging from 3.2 to 5 cm above the mean water level at wind speeds ranging from 1.5 to 5 m s^{-1}. They observed that the magnitude of the streamwise wave-induced velocity ($\tilde{u}$) at the lower wind speed was larger than that at the higher wind speed however the decay rate were

found to be equal. They also reported that the maximum magnitude of $\tilde{u}$ occurred at the wave crest and the minimum magnitude at the wave trough. Lai and Shemdin (1971) investigated the effect of wave propagation on the wind field over mechanically-generated water waves. The experiments were conducted at heights of 10.2 cm and above the mean water level using hot-film anemometer. The measurements were taken at various fetches ranging from 9.15 to 24.36 m and at wind speeds ranging from 1.95 to 10.66 m s^{-1}. They observed that the wave-induced velocity decays faster with height at higher wind speeds. They observed that at different fetches, the wave-induced velocity has same order of magnitude as the wave height and argued that the wave-induced velocity is independent of the fetch.

1.2.4. Measurements within crest-trough region

The literature shows that most of the measurements were taken at heights greater than the wave amplitude. Thus, it is difficult to capture the dynamics within the fluctuating region i.e. bounded between the crest and trough of a wave. To capture the flow dynamics within the crest-trough region, some researchers had used wave-follower system and conducted measurements at a constant height from the fluctuating water surface. Kawamura and Toba (1988) mounted hot-wire anemometer over the wave follower system and measured the airside velocity fluctuations at a height of 6.9 mm above the wind waves. The experiments were performed at a fetch of 6 m and at a wind speed of 5.75 m s^{-1}. They intermittently observed a sudden increase in the magnitudes of velocity fluctuations on the leeward side of the crest and attributed this change to the

existence of the separation bubble. They reported high shear region on the leeward side of the crest that was extended to the wave crest. Papadimitrakis et al. (1986a) investigated airside velocity field above mechanically-generated water waves of amplitude 2.54 cm. The measurements were taken at heights of 7.5 mm and above the fluctuating water surface using hot-film anemometer that was mounted on the wave follower system. The experiments were performed at a fetch of 13 m and at wind speeds ranging from 1.4 to 4 m s^{-1}. They observed a constant layer of turbulent Reynolds stress in the near surface region, whereas a decreasing trend was reported in the magnitudes of wave-induced Reynolds stress with height. They also observed positive and negative wave-induced Reynolds stress within the boundary layer and attributed this sign change to the upward and downward transfer of momentum. Hsu and Hsu (1983) mounted hot-film probe on a wave-follower to measure air velocities above mechanically-generated water waves in the presence of wind. They measured velocities at heights greater than or equal to 1.6 cm above the fluctuating water surface in the presence of 2.67 cm amplitude waves at wind speeds ranging from 1.37 to 2.92 m s^{-1}. They observed that the structure of wave-induced velocity field strongly depends on the parameter U_∞/c, where U_∞ is the wind speed. They argued that in the near surface region, the wave-induced Reynolds stress is produced from the stretching and vertical oscillation of the turbulent velocity with the waves. The wave follower system could provide quantitative measurements at a location within the crest-trough region.

1.3. PIV measurements

Reul et al. (1999) conducted experiments at a fetch of 5 m at a wind speed of 6 m s^{-1}. They observed separated flow region that started at a point close to the crest and reattached on the windward face of the following wave. They concluded that the dynamics of the separation region is similar to that of the flow over a backward facing step. Veron et al. (2007) presented a snap shot of the instantaneous airside velocity field, which shows the flow separation over a wind generated water wave. The experiments were performed at a fetch of 21.1 m and at a wind speed of 5.7 m s^{-1}. They computed the tangential stress at a height of 0.154 mm from the fluctuating water surface and reported that the maximum tangential stress occurred at the crest which approached zero within the separation region and then gradually increased to its maximum value at the next crest. They argued that at wave crest the tangential stress is the dominant component of the total wind stress. Reul et al. (2008) conducted experiments at a fetch of 4.5 m and at wind speeds ranging from 3.5 to 10 m s^{-1}. They presented instantaneous snapshots of velocity, vorticity, and streamline patterns at different stages of the wave-breaking process and observed airflow separation downwind of unsteady breaking crests and argued that the dynamics of the separated flow is correlated with the instantaneous geometry of the wave crest. They also observed strong patches of clockwise vorticity, dominant within the separated flow region downwind of the crest. They further argued that the vorticity field within the separated airflow region demonstrates the mechanism of re-entrainment of stress bearing fluid from the outer part of the shear layer to the interface. Reul et al. (1999) also evaluated the tangential stress, within a distance of 1.2 mm above the

mechanically-generated water waves. They compared the tangential stress of two instantaneous PIV velocity fields, for separated and non-separated flows. They reported that the tangential stress over the non-separated flow grows progressively on the windward side from its minimum value at the trough to the maximum value at the crest. Whereas, over the separated flow, they observed that the tangential stress decreased significantly within the separation region and then increased progressively to its maximum value at the next crest. It should be noted that Reul et al. (2008) and Veron et al. (2007) estimated the tangential stress from single instantaneous velocity field for the separated or non-separated condition. In addition, none of these studies were focused on the investigation of the wave-induced motions and their influence on the air-water transport processes which is mainly attributed to the challenges in extracting the wave-induced velocity component from the instantaneous velocity. Furthermore, the previous studies that measured the wave-induced velocity component using point measurement techniques were not able to fully capture the wave-induced motions over the spatial extent of the wave and thus, the influence of waves on the transport of momentum and energy is not well explored.

1.4. Motivation and Objectives

1.4.1. Problem Identification (Motivation)

Based on the literature review in the previous section, the shortcomings of the previous studies can be summarized as:

- Not enough experimental work was conducted to investigate the effect of airside turbulence on the complex mechanism of the surface wave generation.
- Climate models (that are used to calculate the global heat and mass transfer) are based on the bulk formulae in which air properties are measured at a height of 10 m above the water surface. The assumption that the air properties at 10 m height are good representative of the properties at the surface is questionable and leads to inaccurate flux estimates.
- As a result of the experimental difficulties, the majority of the laboratory experiments were conducted at a height ranging from 1 cm to 20 cm above the fluctuating water surface. Due to the coupling between wind and waves, the region immediately above the water surface plays a crucial role in controlling the fluxes of momentum, heat and mass. A detailed investigation of the flow structure in this region is vital in order to obtain the understanding of the fundamental transport processes.
- The empirical relations developed to estimate the turbulent characteristics in the near wall region are often used to estimate the desired turbulent quantities over the water surface. Whereas, qualitative visual investigations and some of the recent airside studies conducted within few millimeters from the interface show that the airflow adjacent to the water surface is significantly different from that over a solid wall.
- Due to the unavailability of the accurate measurements close to the surface the theoretical models available in the literature show substantial disagreement. For

improved modeling of wind-wave interactions, additional experimental data especially in the near surface region is necessary.

- Most of the researchers have used point measurement techniques in their measurements. Point measurement techniques can provide a time history of the flow but it is not capable of providing instantaneous spatial structure of the flow. In addition, this technique cannot be used for measurements in the region between the wave crest and trough.
- To-date no study reported the mean and turbulent properties within the crest-trough region, specifically in the separation zone, and the influence of airflow separation on the process of momentum transfer across the air-water interface.
- Some of the field measurements speculated that the upward momentum transfer occurs from wave to the wind. They attributed that the upward momentum transfer is associated with fully developed waves. None of the laboratory or field studies reported direct measurement of the upward momentum transfer.

1.4.2. Objectives

As highlighted in the previous section, due to the complexity of the flow field, the mechanism of momentum, heat and mass exchange between air and water in the presence of wind is not well understood. Without deep insight into the turbulent structure of the flow, better understanding of the momentum transfer mechanism is difficult to achieve. With the availability of the state-of-art PIV measurement system, most of the difficulties associated with previous experimental studies will be overcome. This research is a step

towards the improved understanding of this complex flow field. Especially the investigation of the airflow structure into the region immediately above the fluctuating water surface which to the best of our knowledge, is the first attempt to study the detailed flow characteristics in this region. The specific objectives of the research are:

- Quantitative determination of the instantaneous and mean flow characteristics over wind generated water waves, especially within the crest-trough region.
- Detailed investigation of various turbulent and wave-induce properties in the close vicinity of the wave and their variation with respect to the phase and height.
- To investigate the impact of flow separation on the near-surface flow behaviour.
- Quantitative comparison of mean and turbulent characteristics over wind-sheared water surface with that over smooth and wavy walls.

1.5. Thesis Layout

In this dissertation, the research was focused on the study of the airflow structure over wind generated water waves, especially within the crest-trough region. In Chapter 1, a general introduction was provided, followed by the literature review and the motivations for this research. A complete description of the experimental setup and various data processing techniques were provided in Chapter 2. In Chapter 3, the instantaneous, mean and turbulent flow characteristics were described immediately above the wind-sheared water surface in the presence and absence of the surface water waves. In Chapter 4, various turbulent and wave-induced properties were described as a function of phase and height in the immediate vicinity of the waves. In Chapter 5, quantitative

comparison of different flow properties for the separated and non-separated flows over wind generated water waves was presented. In Chapter 6, detailed quantitative comparison was presented between the airflow structure immediately over the water and solid surfaces. In Chapter 7, the main results of the present research are summarized along with recommendations for future work.

CHAPTER 2

Experimental setup and methods

The experiments were conducted in a wind-wave flume 0.45 m wide, 0.9 m high and 3 m long. The sidewalls and the bottom of the flume were made of ¼ in. and 1/2 in. thick glass sheets, respectively. The top was covered by a removable ¼ in. thick Plexiglas sheet. Since, the present study includes the comparison of airflow structure over the water surface with that over the smooth and wavy walls. Therefore, the experiments were carried out in the same wind wave flume for three different configurations. In the first configuration, the tank was filled with clean tap water, and the mean water depth was maintained at 0.45 m (see figure 2.1a). In the second configuration, the lower half of the flume (i.e. 0.45 m from the bottom floor) was covered with a 5 mm thick hardboard panel, which was considered as a smooth wall (see figure 2.1b). In the third configuration, a corrugated plastic sheet with wave height of 1.5 cm was place on the hardboard panel, which was considered as the wavy solid wall. At the wind speed of 4.4 m s^{-1}, the significant wave height of water waves was about 1 cm with the maximum wave height of about 1.6 cm. Thus, the wave heights at the solid and water surfaces are quite comparable. For all three configurations, the measurements were made at same wind speeds ranging from 1.5 m s^{-1} to 4.4 m s^{-1}, and at the same measurement location (2.1 m from the inlet of the test section). The air was introduced in the upper half portion by an axial fan installed at the upstream end of the flume.

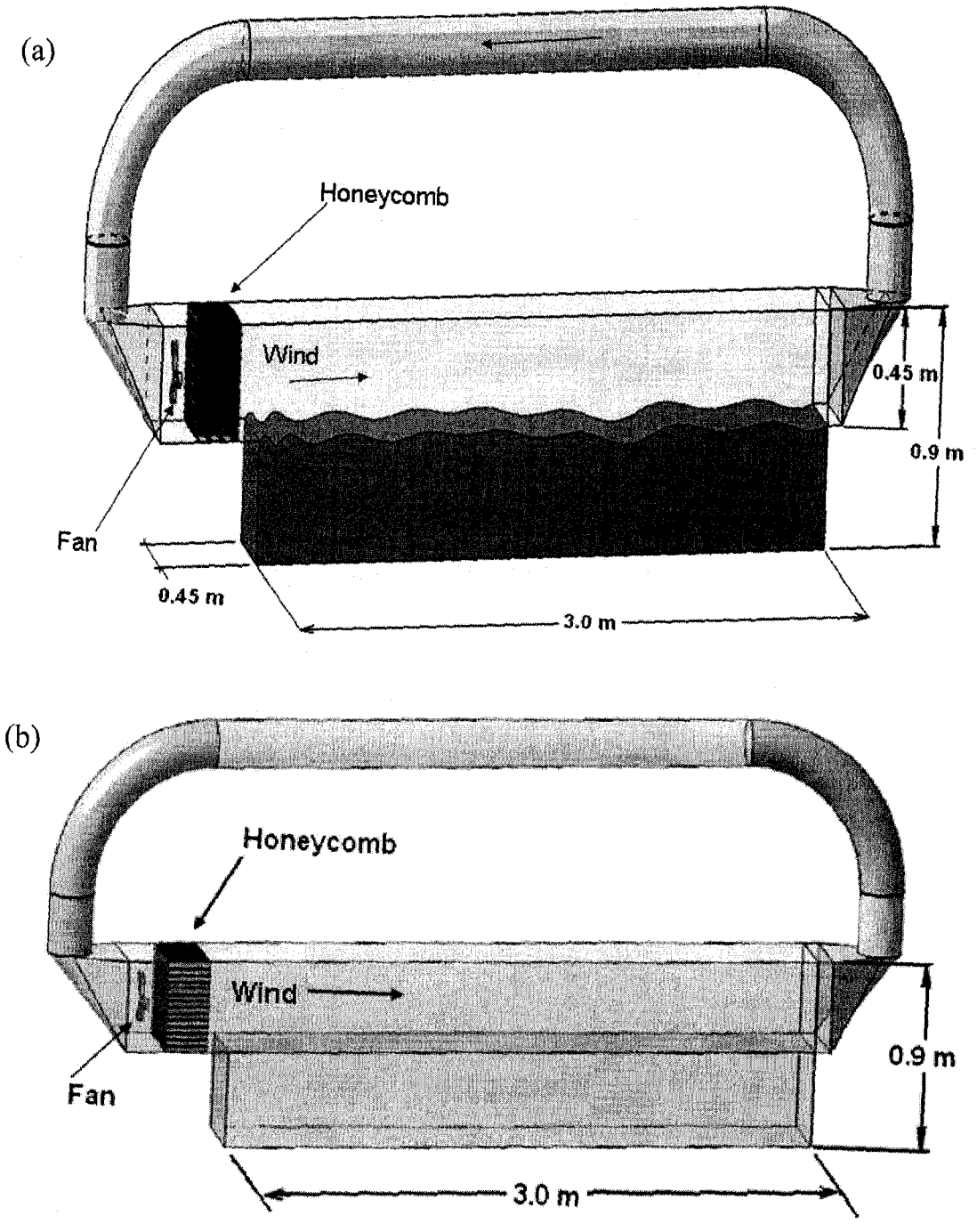

Figure 2.1: Isometric view of the test facility for measurements above, (a) water surface, (b) solid wall

The fan was driven by a 1.5 hp electric motor equipped with a variable frequency drive to vary the air speed from 0 to 5 m s^{-1}. A honeycomb of fine square tubes is installed downstream of the fan and upstream of the flume to allow uniform air flow into the flume. The flume is completely sealed and the air was re-circulated via an aluminum duct (see figure 2.1). The diameter of the recirculation duct is 30 cm, which is sufficiently large to maintain zero pressure drift at the suction of the fan. For the first configuration, a horsehair beach was placed at the downstream end of the flume to absorb wave energy.

Particle image velocimetry (PIV) was used to measure two-dimensional instantaneous airside velocity fields in a plane parallel to the airflow along the centerline of the flume. The PIV setup is shown in figure 2.2. A 25 mJ Nd:YAG laser was used as the light source, a four-channel digital delay generator (555-4C, Berkeley Nucleonics Corporation, San Rafael CA) was used to control the timing of the laser light pulses, and a CCD camera with the resolution of 1600 × 1200 pixels was used to image the flow field. The camera was mounted in the vertical position to allow measurements to a greater height. That is, the images were acquired with the dimensions of 1200 pixels in horizontal and 1600 pixels in vertical, with respect to the flow field. The fields of view of the camera for the three configurations are presented in Table 2.1. For the first configuration, the vertical position of the camera was set in a way that the lower edge of the image was located 1.8 cm below the interface to ensure that in all configurations the interface was clearly visible in all PIV images, at all wind speeds. For the third configuration, the field of view of the camera was set in a way to capture two complete wave profiles of the solid wall.

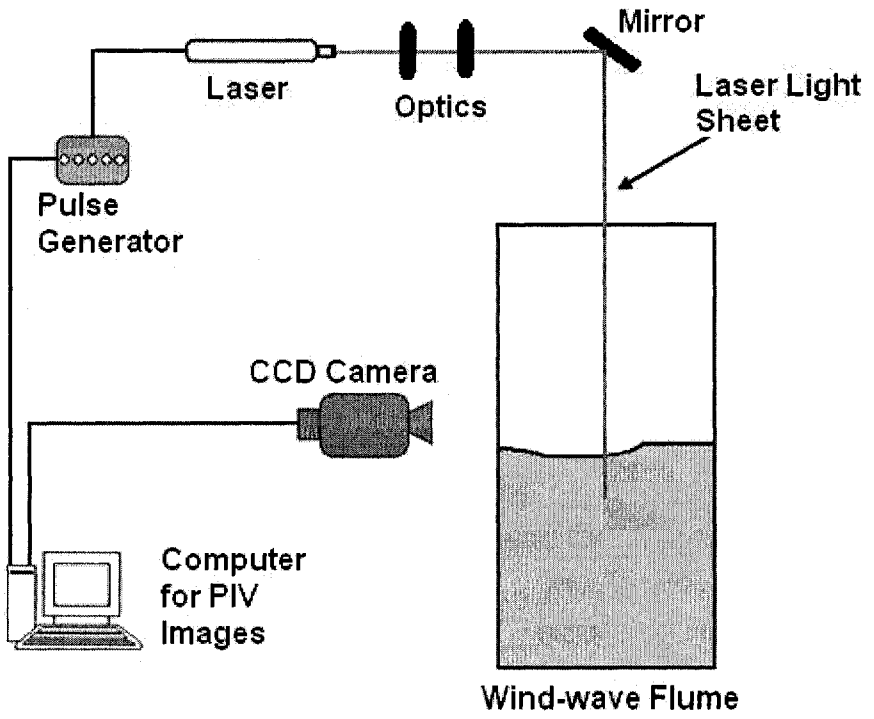

Figure 2.2: Schematic of the experimental setup and instrumentation

The camera was connected to a PC equipped with a frame grabber (DVR Express, IO Industries, London, ON, Canada) that acquires 8-bit images at a rate of 30 Hz. For the first configuration, the air was seeded with olive oil mist of mean diameter of 1 μm, whereas for the second and third configurations the air was seeded with BIS (2-ETHYLHEXYL) SEBACATE mist with the mean diameter of 0.5 μm. The reason for switching to SEBACATE was due to its better performance in wind tunnel PIV measurements. An Aerosol generator (Lavison GmbH) was used to produce the mist. The mist was introduced into the flow upstream of the fan to allow effective mixing into the air. For each experimental run the fan was started at the given rpm. Approximately 20

minutes later the seed particles were injected into the air stream. The data acquisition was started approximately 10 minutes after injecting the seed to ensure homogenous seed distribution throughout the air loop. The sequence of experiments was according to the configuration. That is, the first set of experiments was conducted with the first configuration i.e. above air-water interface, the second set of experiments with the second configuration i.e. above the smooth wall, and the third set of experiments with the third configuration i.e. the wavy solid wall. For each experimental run (i.e. each configuration at a given wind speed), 9000 images were acquired at a rate of 30 Hz. The reference wind speeds used in the present study were based on the average free-stream velocities at a distance of 33 cm above the undisturbed water or solid surface. For this purpose, the camera was moved vertically up in the free-stream region and PIV images were acquired at all given wind speeds. In order to keep reasonable particle shifts, the time separation between the two images of an image pair was varied from 0.5 ms at the lowest wind speed to 0.05 ms at the highest wind speed. The velocity fields were obtained by cross-correlating the interrogation region in the first image with the corresponding search region in the second image of an image pair. The size of the interrogation region was set equal to 32 × 32 pixels and the size of the search region was set equal to 64 × 64 pixels. A 50% window overlap was used in order to increase the resolution of the velocity field to 16 × 16 pixels. The spatial resolution of the velocity field was different for each configuration due to the difference in the camera's field of view. The spatial resolution of the velocity field of each configuration is given in Table 2.1.

TABLE 2.1: Camera field of view, spatial resolution of the velocity field and uncertainty in velocity measurements for the three configurations

Configuration	Camera field of view	Spatial resolution of the velocity field	Uncertainty in velocity measurements
Flow over water surface	10.7 cm × 8 cm	1.06 mm × 1.06 mm	7%
Flow over smooth wall	10.4 cm × 7.8 cm	1.03 mm × 1.03 mm	5%
Flow over wavy wall	16 cm × 12.2 cm	1.63 mm × 1.63 mm	6%

2.1. Interface detection

As mentioned in the previous section, for the measurements in the near-surface region, the camera position was set in a way that for all three configurations, the interface was visible in all PIV images. To obtain reliable estimates of the near surface velocity, it was necessary to locate the interface position accurately. For the airflow over the water surface, the contrast between the air and water was improved by dissolving dark blue food color in the water prior to the experiments. This resulted in the uniform gray-scale value in the waterside regions of the PIV images, which facilitated the implementation of an image processing technique to locate the air-water interface. A raw PIV image taken at a wind speed of 3.7 m s^{-1} is shown in figure 2.3a. The dark waterside region with almost uniform gray-scale values is also visible in the image.

For the airflow over the water surface, at wind speeds of 1.5, 2.1 and 3.0 m s^{-1}, the amplitude of water ripples was so small that the air-water interface appeared as a smooth horizontal surface in the PIV images and the location of the interface was a relatively easy task. To locate the interface position in each of these datasets, 10 images were selected from the beginning and end of the dataset. In each of the selected images, the interface position was recorded in the right, left and central regions of the image by visual detection. The interface positions recorded in each image were then compared. It was found that the vertical variation in the interface position from the beginning to the end of the data acquisition (i.e. over five minute duration) and from left to right was on average within 2 pixels (130 μm). As a conservative estimate, the highest position of the interface from the sample images was taken as the interface location for all images in the given dataset. As the solid smooth wall was fixed, the same process was repeated to detect the interface location for the second configuration as well.

For the airflow over the water surface, waves were observed in the PIV images acquired at wind speeds of 3.7 and 4.4 m s^{-1}(see figure 2.3a). In order to obtain accurate estimates of the near surface velocity fields, it was necessary to detect the exact locations of the fluctuating water surface in the PIV images. A threshold-based image processing scheme similar to that reported by Siddiqui et al. (2001) was developed to detect and locate the fluctuating water surface in PIV images. This technique was based on the difference in the gray-scale values in the air and water sides, where the former has higher gray-scale values due to the presence of illuminating seed particles. Due to the Gaussian distribution of the light sheet intensity, the gray-scale values near the right and left edges in all images were relatively lower, which resulted in a low contrast between the airside

and waterside gray-scale values. The contrast was adjusted in these regions prior to the implementation of the detection scheme. In the detection scheme, a threshold was applied to segment the image. The mean gray-scale value on the waterside was selected as the threshold. All pixels with gray-scale values greater than the threshold were assigned 1's (i.e. white) and all pixels less than or equal to the threshold were assigned 0's (i.e. black). A series of morphological operations were performed next on the binary image. The sequence of these operations is as follows. A dilation operation with a mask of 2 × 2 pixels was performed, which was followed by a flood-fill operation, to remove tiny black objects appeared on the airside of the binary image. Finally, a dilation operation followed by an erosion operation was performed with a mask of 6 × 6 pixels. Figure 2.3b shows the binary image obtained after applying the detection scheme to the image shown in figure 2.3a. Once the binary image was obtained, the air-water interface was detected based on the jump in the binary values at the interface. The horizontal and vertical coordinates at all interface locations in each image were recorded. To check the accuracy of the detection scheme, each detected surface profile was plotted over the corresponding original PIV image for visual inspection (i.e. 9000 profiles at each wind speed were checked visually). It was found that in 90% of the images, the detected profile accurately followed the actual interface throughout the image. In 10% of the images, small deviations were observed sporadically at one or two locations in an image, which was corrected by manual editing. To quantify the accuracy of the detection scheme, the surface profile was plotted over the PIV image. The image was magnified and the maximum deviation between the actual and computed water surface was recorded. This process was repeated on 50 images taking from the beginning and end of each dataset.

The uncertainty in locating the water surface was estimated to be within $\pm$ 250 μm. The surface profile computed from figure 2.3b is shown plotted over the PIV image in figure 2.3c.

The surface profile data were used to compute wave properties. For this purpose, time series were extracted at 72 spatial locations along the profile. Dominant wave frequency, significant wave height (i.e. the average height of the highest one-third waves) and the RMS wave height were computed from each time series and then averaged. These values at 3.7 and 4.4 m s^{-1} wind speeds are presented in Table 2.2. As mentioned earlier, mist was used as the tracer particles. Although the volumetric concentration of the mist was very low, but a small fraction of the mist was deposited on the water surface during the experiments, which acted as a surfactant and modified the hydrodynamic boundary condition. This would tend to reduce the wave amplitude and dampen the small-scale capillary waves.

TABLE 2.2: Summary of wave characteristics computed from the wave profile data at the two highest wind speeds.

Wind speed (m s^{-1})	RMS wave height (cm)	Significant wave height (cm)	Dominant wave frequency (Hz)	Dominant wavelength (cm)
3.7	0.27	0.59	5	5.9
4.4	0.46	0.974	4.2	9.0

For the third configuration, the wavy wall was detected in one of the raw PIV image, taken at wind speed of 4.4 m s^{-1}, using the scheme similar to the one used to detect the fluctuating air-water interface. As the solid wavy wall was fixed, the same surface profile was used for the entire dataset.

2.2. Velocity field computation

For the two data sets recorded over the wavy water surface at wind speeds of 3.7 and 4.4 m s^{-1}, the procedure for the computation of the velocity fields is as follows. First the velocity field was computed by cross-correlating the raw PIV image pairs. Since there were no seed particles on the waterside, in the interrogations windows that contain waterside region, false velocity vectors were computed. In the next step, the corresponding surface profile data was imported in each velocity field and all velocity vectors below the water surface were removed.

For the third configuration, first the raw images were preprocessed before velocity computation. In the preprocessing step, the surface profile was imported in each of the image and the portion of the images below the solid wave was assigned a constant gray scale value equal to the mean gray-scale value of the background. In the present study, this value was set equal to 100. The reason for this was to increase the accuracy of the velocity vectors computed in the region immediately above the solid surface. The velocity fields were computed by cross correlating these preprocessed image pairs. The computed velocity fields over the solid wave also contain false velocity vectors below the interface. Therefore, the computed surface profile was imported in each of the velocity field and all

of the velocity vectors below the solid wave were removed. For the flow over the smooth air-water and air-solid interfaces, the raw PIV images were also preprocessed before velocity computation. In the preprocessing step, the computed co-ordinates of interface were imported in each of the raw PIV image and the portion of the images below the interface was chopped off, leaving only the airside portion in each image. The velocity fields were obtained by cross correlating these preprocessed image pairs.

The grid points nearest to the interface were located between 0 and 1 mm from the water waves and between 0 and 1.6 from the solid waves, in the vertical directions. Thus, on average, the nearest velocity vectors were located at a height of 0.5 and 0.8 mm from the water and solid waves, respectively. Whereas, for the flow over the smooth solid or water surface, the nearest grid point was located at a height of 2 mm from the interface. Finally, for all three configurations, the spurious velocity vectors within the airside velocity field were identified and replaced with the local median value (i.e. the median of the eight neighboring values) using the technique described in Siddiqui et al. (2001). Typically, less than 0.5% of the velocity vectors were found spurious in the velocity field. Figure 2.3d shows the corrected instantaneous airside velocity field obtained from the image pair in figure 2.3a. The detected surface profile is also plotted in the figure.

The total error in the PIV velocity measurements is the sum of errors due to velocity gradients, particle density, particle diameter, out-of-plane motion, dynamic range, peak locking and AGW interpolation (Cowen and Monismith 1997). For the present conditions these errors were computed by using results from Cowen and Monismith (1997) and Prasad *et al.* (1992).

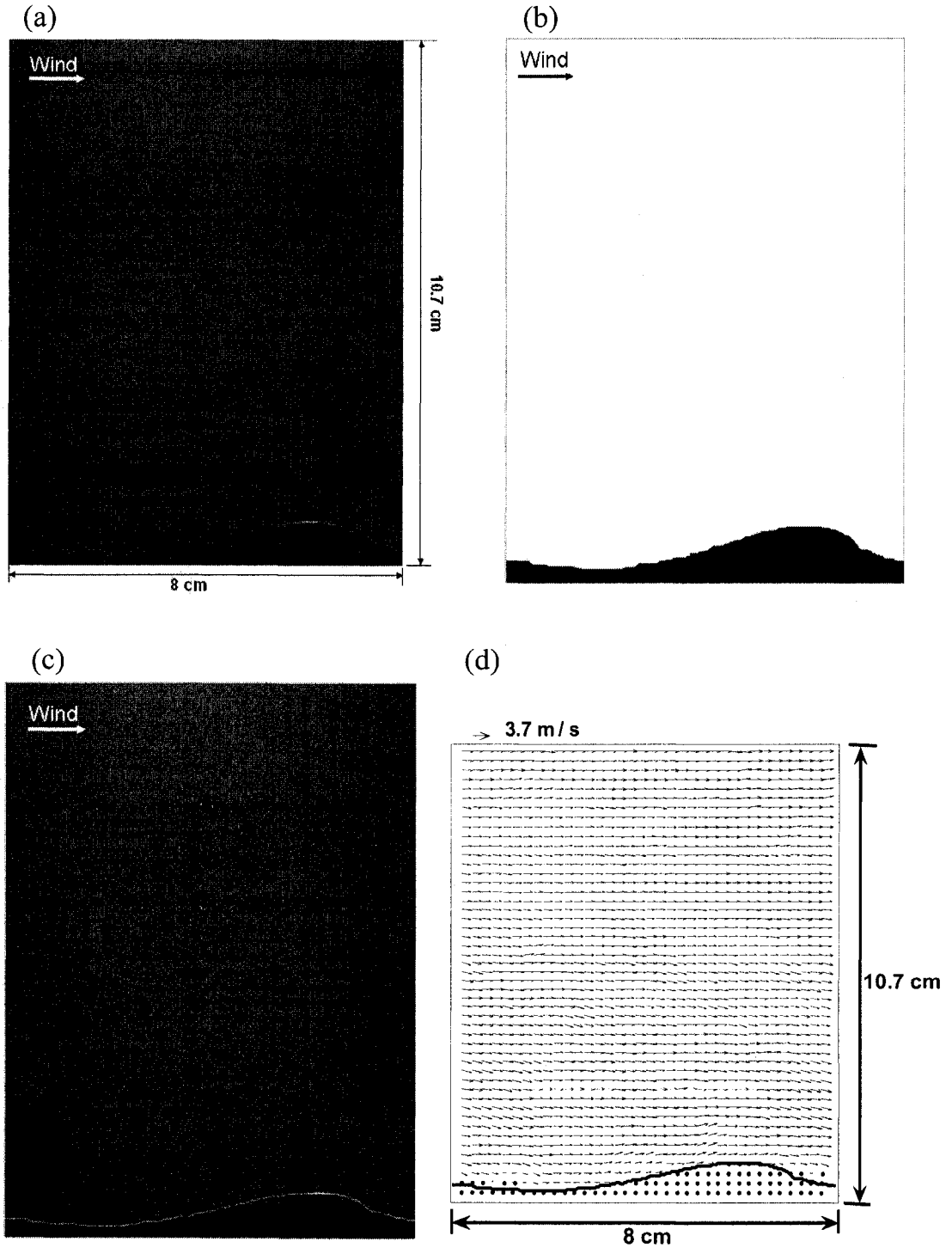

Figure 2.3: (a) A raw PIV image of dimensions 8.0 × 10.7 cm at a wind speed 3.7 m s^{-1}; (b) Binary image obtained after applying the detection scheme to the PIV image in (a); (c) PIV image with the computed surface wave profile; (d) Instantaneous airside velocity field obtained from the corresponding PIV image pair

The uncertainty in velocity measurements based on these errors is presented in Table 2.1 for all three configurations. The complete error analysis is provided in Appendix I.

In order to compute the mean velocity, the measured instantaneous PIV velocity fields were transformed from fixed Eulerian coordinate system to a wave-following Eulerian system using the technique described in Hsu et al. (1981). In this transformation, the velocity vectors were arranged with reference to the water surface using a new vertical coordinate ξ, such that $\xi = 0$ at the instantaneous water surface and the positive ξ-axis pointing upward. Note that the horizontal coordinate remains the same. This coordinate transformation scheme was also applied to the instantaneous velocity fields measured above the solid waves. The mean velocity field was computed by averaging the velocity data temporally at each grid point.

PIV measurements provide instantaneous velocity fields. Conventionally, the instantaneous velocity comprised of two components; mean and turbulent. However, in the presence of waves, a third component is also induced which is known as the wave-induced velocity (Hussain and Reynolds 1970). Thus, the instantaneous velocity over the waves can be decomposed as,

$$u(x,y,t) = \overline{u}(x,y) + \widetilde{u}(x,y,t) + u'(x,y,t) \tag{2.1}$$

where, u is the instantaneous velocity, $\overline{u}$ is the time-averaged velocity, $\widetilde{u}$ is the wave-induced velocity, and u' is the turbulent velocity. As described in the introduction section, for the flow over the water waves, the wave induced component of the instantaneous

velocity plays significant role in the momentum exchange across the air-water interface. Whereas, for the flow over the solid waves, the influence of wave induced variation to turbulent velocity fluctuations is negligible (Frederick and Hanratty 1988). Furthermore spatial averaging of different turbulent properties nullified the wave induced effects of stationary waves (Perry et al. 1987). As stated above, in the first configuration waves were observed only at wind speeds of 3.7 and 4.4 m s^{-1}, therefore for these two wind speeds, both the wave-induced and turbulent velocities were computed at each grid point, using a novel technique described below. However, for the flow over smooth water surface and for the second and third configurations, the turbulent velocity was computed by subtracting the mean velocity from the instantaneous velocity. The following section describes the technique used to compute the wave-induced and turbulent velocity fields, using the instantaneous velocity fields and surface profiles.

2.3. Phase Computation

As mentioned above, the velocity vectors in the computed velocity fields are 1.06 mm (16 pixels) apart, in the horizontal and vertical directions. Phase averaging of the velocity data will only be meaningful if there is sufficient number of data points along a given wave. Therefore, prior to phase averaging, the wave profile data was spatially low-pass filtered with a cutoff wavelength of 8.5 mm to eliminate small waves that have less than eight velocity vectors along the wavelength. That is, at least one velocity vector for every 45 degree phase change. In order to compute the phase at each pixel along the measured surface wave profiles, a given wave is divided into four segments,

$$\lambda = L_1 + L_2 + L_3 + L_4 \tag{2.2}$$

Where, λ is the wave length and L_1, L_2, L_3, L_4 represent different segments of the wave (see figure 2.4). The local maxima were defined as the wave crests with a phase of zero degree and the local minima were defined as the wave troughs with a phase of 180 degree. Zero crossings were defined as locations where the wave profile crosses the mean water level. Zero crossings were assigned either a phase of -90 degree or +90 degree depending on whether they were located on the windward or leeward face of the wave, respectively.

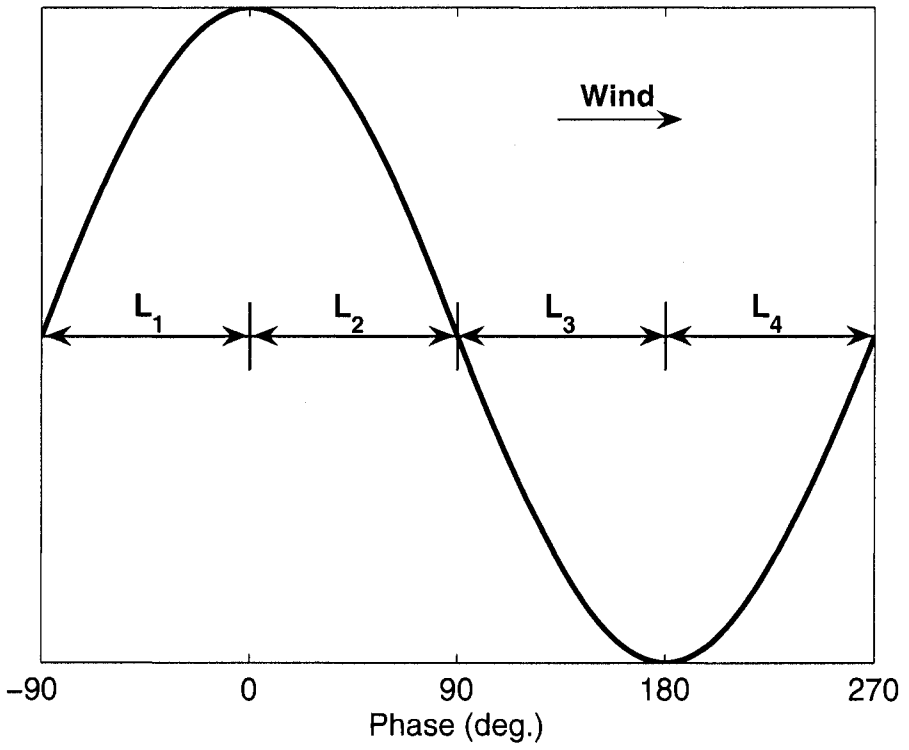

Figure 2.4: Schematic showing four segments L_1, L_2, L_3 and L_4 of a wave that are used for the phase-averaging scheme

As mentioned earlier, the field of view of the PIV images were set 8 cm horizontal and 10.7 cm vertical, therefore the waves with wavelength greater than 8 cm were only partially visible within the image. In the images where the entire wave was visible, phase computation along the wave was straightforward. The images in which partial wave was visible, computation of the phase was quite challenging. An algorithm was developed to compute the phase at each pixel using the surface wave profile data. It should be noted that in the PIV technique, two successive images (an image pair) were used to compute a velocity field. Since the time delay between the two images of an image pair was very small (less than 75 μs), there was no significant difference in the position and shape of the surface profiles in both images of the image pair. Thus, the mean profile of each image pair was used for the phase computation.

In the first step of this algorithm, all surface wave profiles were categorized based on the number of zero-crossing. The number of zero crossings appeared in a wave profile depend on the wavelength and the position of the given wave with respect to the camera field of view (FOV). Wave profiles with more than three zero crossings in an image were excluded from the phase computation, because these profiles typically comprised of waves with wavelengths significantly smaller than the dominant wave. At wind speeds of 3.7 and 4.4 m s^{-1}, the wave profiles having more than three zero crossing were found less than 8% and 2%, respectively.

In each profile, the locations of all zero crossings and the locations of wave crest or trough that appear in the profile were recorded. Next the phase change per pixel for any of the four segments fully visible in the profile was computed by dividing 90 degree

by the length (in pixels) of the corresponding segment. This value of phase change per pixel was then used to compute the phase corresponding to each pixel of the segment. The crest or trough location, and the zero crossing were used as the reference points for computing the phase. The segments that were partially visible in the profiles were sub-divided into two categories. The first category comprised of the profiles in which the segments were chopped off by the edge(s) of the image before reaching their respective zero crossing (see segment L_2 in figure 2.5a). The second category comprised of the profiles in which the segments were chopped off by the edge(s) of the image before reaching their respective crest or trough (see segment L_4 in figure 2.5a). For the first category, the angle (θ) at the end of the segment was computed using the right-angle triangle as shown in figure 2.5a, and the phase change per pixel was computed by dividing $(90-\theta)$ degrees with the length of the partially visible portion of the corresponding segment. The segments that fell under the second category were excluded from the further analysis. These excluded segments were only 4% and 7% of the total segments at the wind speeds of 3.7 and 4.4 m s^{-1}, respectively.

The technique is explained based on the three cases discussed below. The first case is the one in which a given profile has one zero crossing. Only one zero crossing in a profile indicates that either the leeward or the windward face of the wave is prominent within the image. Figure 2.5a shows a wave profile with one zero crossing, in which the windward face of the wave is prominent. The zero crossing is assigned a phase of -90 degree. The segment L_1 is fully visible in the figure therefore the phase change per pixel for this segment is computed by dividing 90 degree by the length L_1. The phase at each pixel in this segment is varied from -90 to 0. The segments L_2 and L_4 are partially visible.

The segment L_2 falls under the first category and the phase per pixel for this segment is computed using the method described above. The segment L_4 falls under the second category and therefore excluded from the further analysis.

The wave profile with two zero crossings shows either a complete wave crest or trough in the image. Figure 2.5b shows a wave with two zero crossings. The segments L_1 and L_2 are fully visible in the plot therefore, the phase change per pixel and subsequent phase at each pixel is computed in both segments. The segments L_3 and L_4 are partially visible and fall under the second category therefore, excluded from the further analysis.

Profiles with three zero crossings contain complete wave crest and wave trough regions. Figure 2.5c shows a wave profile with three zero crossings, which contain all four segments fully visible. The phase change per pixel was computed for each of these segments. Figure 2.5c also shows partially visible segments L_1 and L_4 that fall under the second category. There were some profiles with no zero crossings. These profiles have either the crest or trough region of a wave within the FOV. These waves have wavelength greater than 16 cm. These profiles fall under the first category and the phase per pixel was computed using the method described above. At wind speeds of 3.7 and 4.4 m s^{-1}, the wave profiles with no zero crossing were found to be 0.6% and 1.5%, respectively.

The number of profiles in which the phase was computed (fully or partially) is presented in Table 2.3. The values indicate that at wind speeds of 3.7 and 4.4 m s^{-1}, the phase was computed in 88% and 96% of the total wave profiles, respectively.

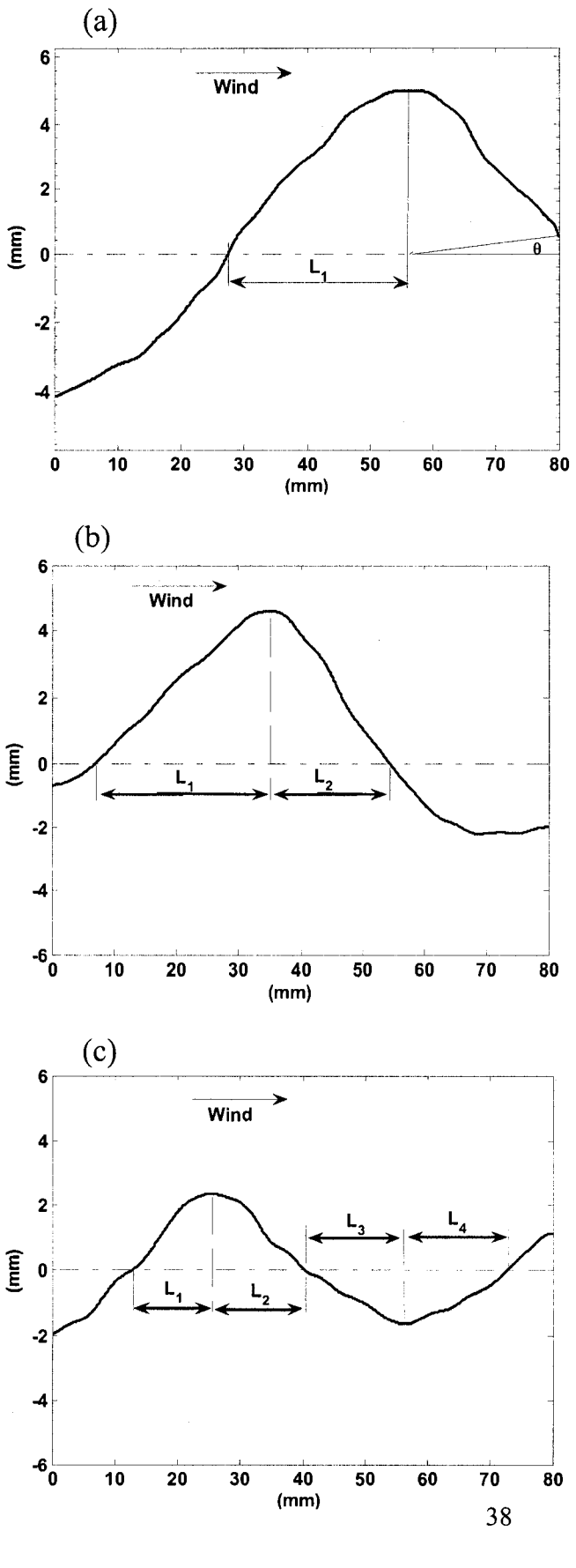

Figure 2.5: Surface wave profiles at a wind speed of 4.4 m s^{-1} showing different categories; (a) One zero crossing, (b) Two zero crossings, (c) Three zero crossings.

TABLE 2.3. Summary of number of wave profiles (N_t total number of wave profiles, N_{zc-1} number of wave profiles having one zero crossing, N_{zc-2} number of wave profiles having two zero crossing, N_{zc-3} number of wave profiles having three zero crossing, N_{zc-m} number of wave profiles having more than three zero crossing, N_{zc-0} number of wave profiles having no zero crossing N_{ph} number of wave profiles used to compute the phase averaged properties.

U_∞ (m s^{-1})	3.7	4.4
N_t	4500	4500
N_{zc-1}	573	2142
N_{zc-2}	2483	1924
N_{zc-3}	861	183
N_{zc-m}	362	84
N_{zc-0}	27	67
N_{ph}	3942	4314

At wind speeds of 3.7 and 4.4 m s^{-1}, most of the wave profiles contain one or two zero crossing with the wavelength of about 6.7 cm and 9.5 cm, respectively, which is close to the dominant wave length (see Table 2.2). In order to show that the conditionally sampled profiles provide accurate representation of the measured wave fields, the probability density functions (PDF) of the surface displacement (η) for the conditionally sampled profiles and all profiles were computed. The results are shown in figure 2.6.

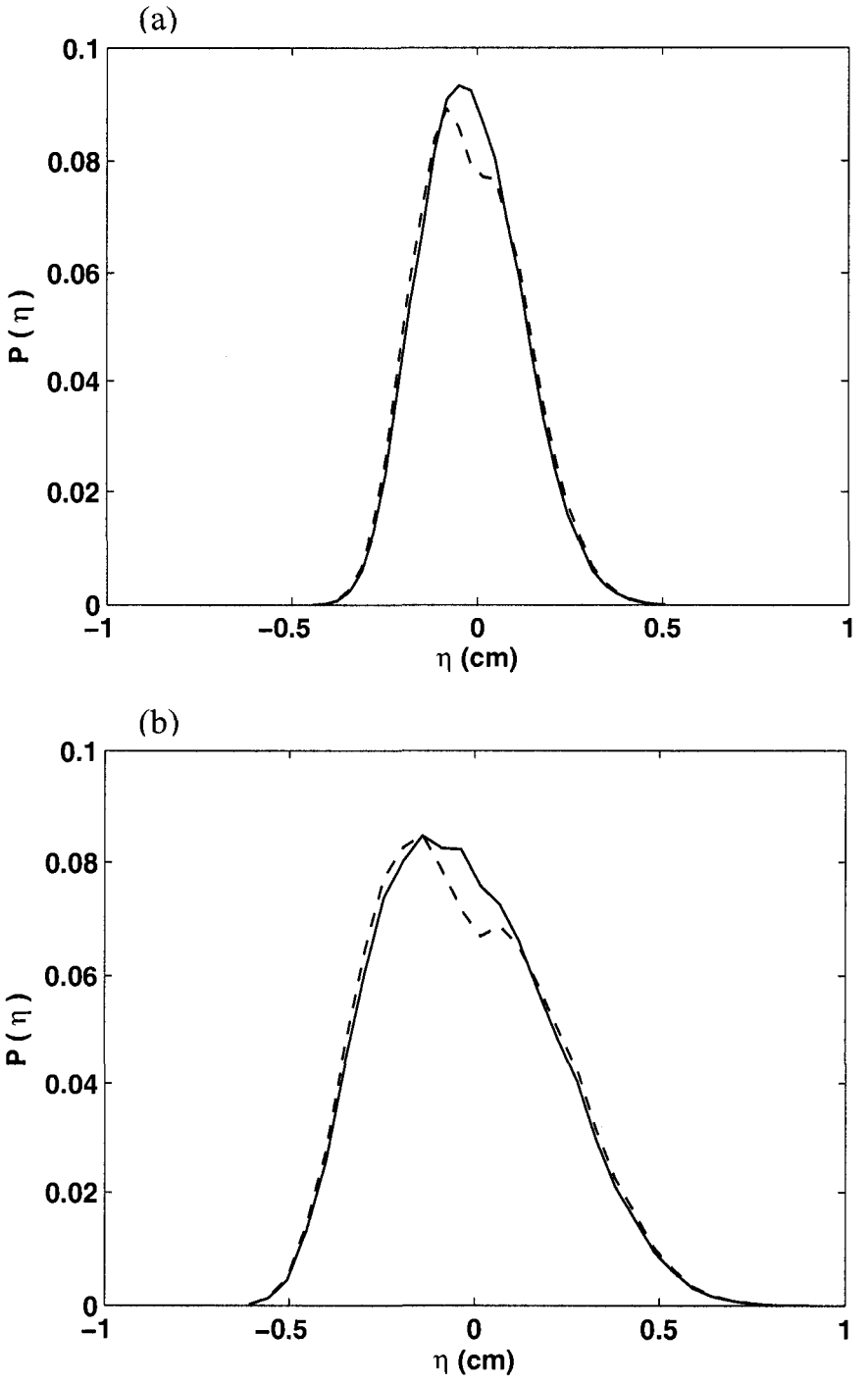

Figure 2.6: Probability density function (PDF) of conditionally sampled wave profiles (dashed line) and all wave profiles (solid lines), (a) at wind speed of 3.7 m s^{-1}, (b) at wind speed of 4.4 m s^{-1}

The plots show that at both wind speeds, the PDF of the conditionally sampled data is almost identical to the PDF of the entire data except in a narrow band around $\eta = 0$, which is due to the low-pass filtering of the conditionally sampled data. These results demonstrate that at a given wind speed, the profiles used for the phase analysis represent the wave population at that wind speed.

2.4. Phase Averaging and Velocity Decomposition

As described earlier, in PIV velocity fields, the velocity vectors were computed at fixed grid points which were 1.06 mm (16 pixels) apart, in the horizontal and vertical directions. For each wave profile, the phase at each grid point was computed and then the velocity data and wave amplitudes were binned according to the phase and height. The bin size was set equal to 5^{o}. The phase-averaged values are then obtained by averaging the data in each bin at each height. The phase-averaged velocity field at a wind speed of 4.4 m s^{-1} is presented in figure 2.7 along with the phase-averaged wave amplitude. The plot shows that the magnitude of the phase-averaged velocity $\langle u \rangle$ at any given phase increased with the distance from the water surface. The plot also shows that in the near surface region, at a given distance from the water surface, $\langle u \rangle$ is maximum at the wave crest which decreased towards the trough. It is also observed that in the near surface region, the magnitude of $\langle u \rangle$ is higher on the windward face compared to the leeward face. This issue will be discussed later.

Figure 2.8 shows a spatial series of the instantaneous velocity data along with the mean velocity and phase-averaged velocity profile at a height of 5 mm above the water surface. The plot clearly shows the decomposition scheme used to separate the turbulent and wave-induced velocity components from the instantaneous velocity. As shown in the figure, the turbulent velocity is computed at each grid point, as the difference between the instantaneous velocity and the corresponding phase averaged velocity (Hsu and Hsu 1983, Mastenbroek et al. 1996). That is,

$$u'(x,y,t) = u(x,y,t) - < u(x,y) > \tag{2.3}$$

The wave-induced velocity is computed at each grid point in a two dimensional spatial plane as:

$$\tilde{u}(x,y,t) = u(x,y,t) - \bar{u}(x,y) - u'(x,y,t) \tag{2.4}$$

An instantaneous wave-induced velocity fields at a wind speed of 4.4 m s^{-1} is plotted in figure 2.9.

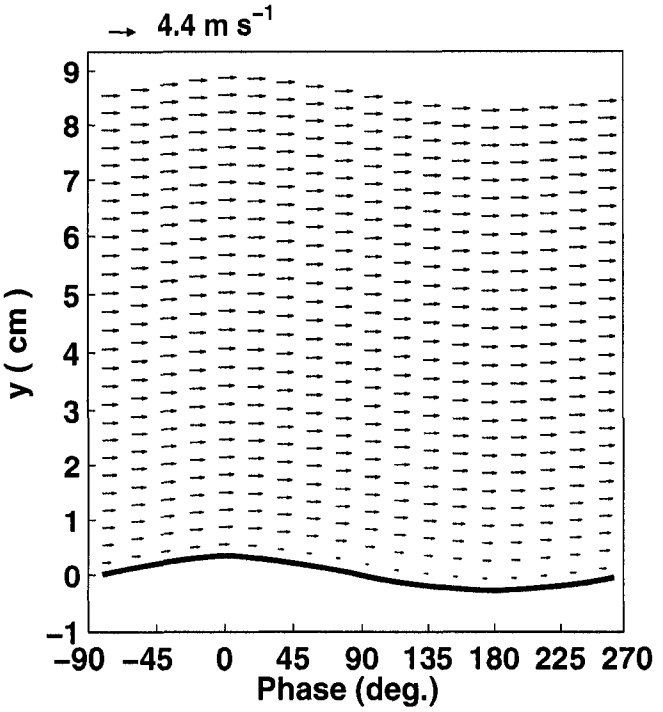

Figure 2.7: Phase-averaged velocity field at a wind speed of 4.4 m s^{-1}. The phase-averaged wave amplitude at 4.4 m s^{-1} is also plotted. y is the distance from the mean water level

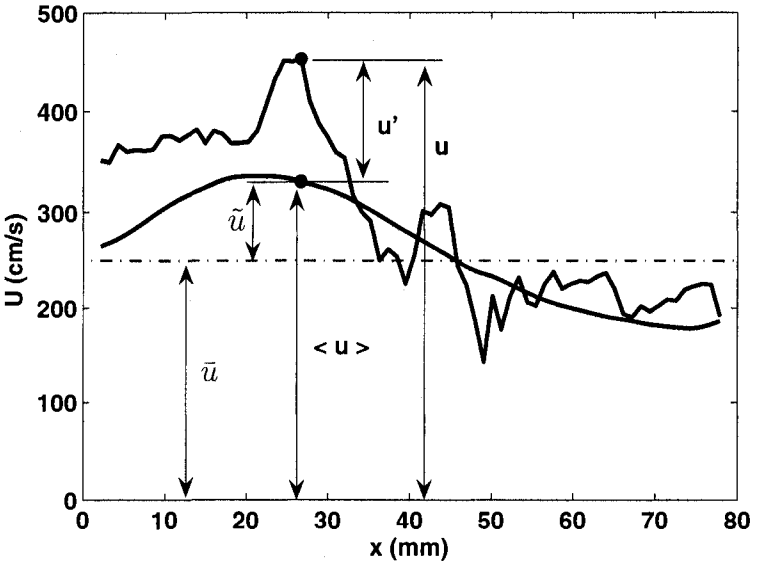

Figure 2.8: Schematic diagram illustrating the procedure to compute wave induced velocity

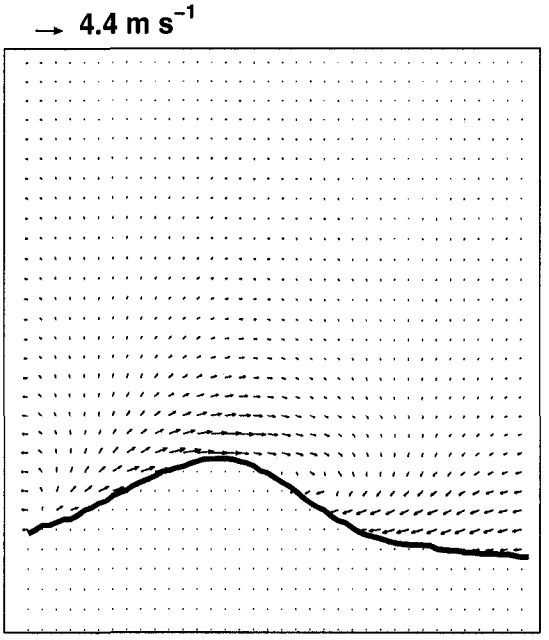

Figure 2.9: An instantaneous wave induced velocity field at a wind speed of 4.4 m s^{-1}

CHAPTER 3

Flow characteristics over wind-sheared water surface

In this chapter the instantaneous, mean and turbulent flow characteristics are described immediately above the wind-sheared water surface in the presence and absence of surface water waves.

3.1. Instantaneous Velocity and vorticity Fields

The high resolution PIV data in the present study is capable of capturing small-scale structures within and above the crest-trough region, which is very crucial to improve our understanding of the dynamical processes in this region. Figure 3.1 shows a series of three consecutive instantaneous velocity fields at a wind speed of 4.4 m s^{-1}. The time interval between the successive velocity fields is 1/15 s, and the total time spanned by these three velocity fields is equal to 1/5 s. During this time period, two consecutives wave crests appeared in the field of view of the camera. A wave crest within the camera field of view is shown in figure 3.1a. On the windward face of the wave, a burst is observed that is ejected from the surface. The bursting process is a characteristic feature of wall bounded flows. Willmarth and Lu (1972) studied the bursting process above a solid wall and described it as follows. The bursting process begins with a lifting motion of a streak of low speed fluid from a region near the solid wall. The burst rises upward until the streamwise velocity component starts to increase and eventually the burst merges into the free stream flow. During breakup of the burst, significant chaotic motion occurs in the fluid. The region occupied by the burst is long and narrow, and appears to grow as it

proceeds downstream. The burst observed in figure 3.1a is qualitatively similar to that described over a solid wall, indicating that the bursting process similar to that over a solid wall occurs above the air-water interface in the presence of wind. Komori et al. (1993) proposed bursting process on the windward side of the wave. They argued that the bursting process above the wind-sheared air-water interface would be different from that observed near the solid wall as the intermittent bursts are always observed on the windward side of the wave. Reul et al. (2008) reported low speed burst only at the reattachment point of the separation bubble. In the present study, however, the bursting is observed mostly on the windward side of the wave crest. Figure 3.1a also shows the flow separation on the leeward side of the wave.

In figure 3.1b, the crest is propagated downwind and the successive wave trough is within the field of view. The flow separation due to the wave crest upwind of the given wave trough (i.e. outside the camera field of view on the left side) is visible in the plot. This separated flow is attached downwind of the wave trough. The wave crest upwind of the camera field of view in figure 3.1b is propagated into the camera field of view in figure 3.1c. The flow separation is clearly visible in the plot. Reul et al. (2008) also reported that the flow separation systematically occurs downwind of the wave. They argued that the flow separation is a strongly unsteady phenomenon and requires a maximum local wave slope of 35^{o} which is in agreement with the critical slope for the airflow separation of 0.6 reported by Kawai (1982). Another interesting feature observed in the plot is the sweeping process in the region where the flow re-attaches. This sweeping process is also a characteristic feature of wall bounded flows (Willmarth and Lu, 1972). When bursts are ejected from the wall, the sweeping process replenishes the mass of fluid.

(a)

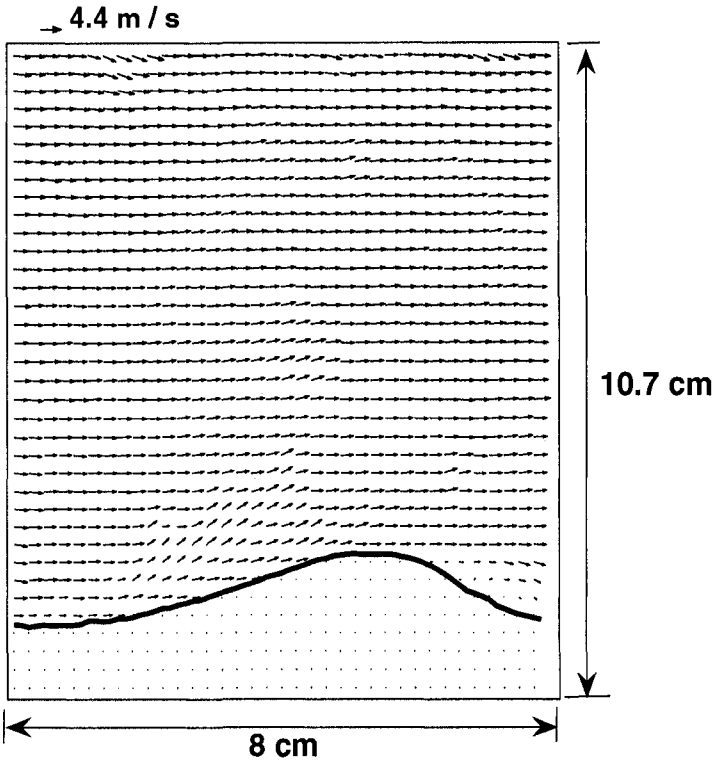

(b)

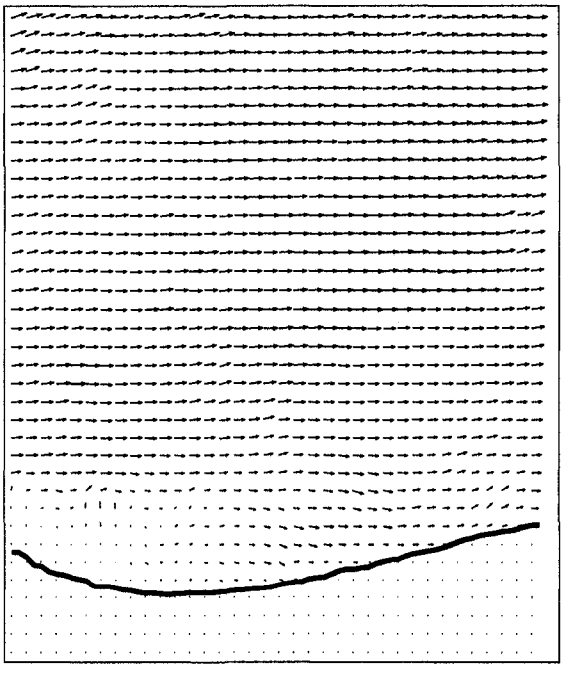

(c)

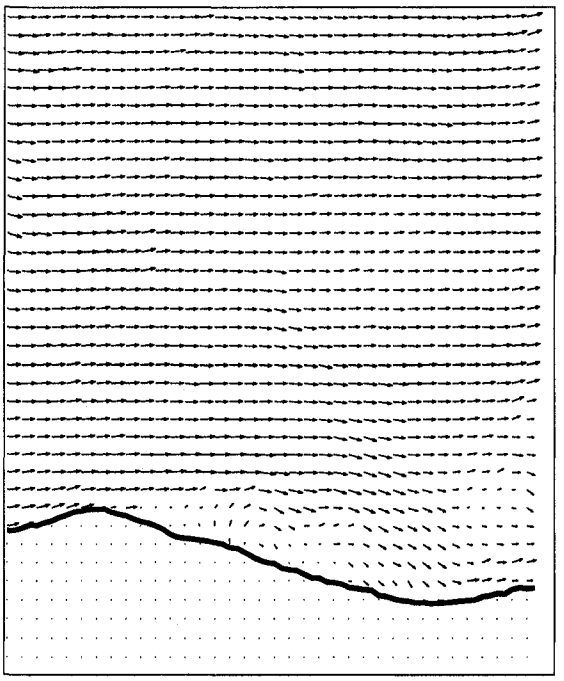

Figure 3.1 (a-c): A sequence of instantaneous velocity fields at a wind speed of 4.4 m s^{-1}

The present results indicate the occurrence of a similar process above the air-water interface. That is, the bursting process (figure 3.1a) is followed by a sweeping process (figure 3.1c). Kawamura et al. (1981) found spikes of large negative values in the time series of the product of the horizontal and vertical velocity fluctuations (i.e. $u(t) \times v(t)$). They attributed these spikes as the ejection and sweep phases of the bursting phenomenon which is consistent with the present study. Reul et al. (2008) observed rising burst of low speed fluid from the reattachment point of the separation bubble but they did not report the sweeping phenomena over the wave. The bursting and sweeping processes similar to the present study are also observed in the field. Donelan et al. (2006) reported the detachment of airflow over the crests and its reattachement on the windward face under

strong wind forcing. The sequence in figure 3.1 provided good qualitative and quantitative insight into the flow dynamics in the crest-trough region. The plots show that the flow separates off the wave crest creating a separated zone on the leeward side of the wave. On the windward side, the flow re-attaches. The bursting and sweeping processes were also observed on the windward and leeward sides of the wave.

The vorticity was computed using the central difference scheme at each grid point in the PIV velocity field, except the grid points adjacent to the boundaries, where the vorticity was computed using the difference between the two adjacent grid points. Figure 3.2 shows the contour plots of the vorticity field computed from the corresponding velocity fields shown in figure 3.1. The vorticity plots illustrate the kinematics of the flow structures observed above the wind waves. Figure 3.2a shows the difference between the vorticity structures observed within the attached and the separated flow regions. The attached flow contains a thin layer of strong clockwise vortices (thick contours) that can be seen along the windward side of the wave crest. The thickness of this vorticity layer is approximately 4.5 mm. The maximum magnitude of vorticity is approximately 560 s^{-1} close to the water surface that has decreased to 105 s^{-1} at the upper edge of the layer. This vorticity layer indicates the presence of strong shear flow over the water surface. At the downwind side of the crest i.e. within the separated flow region, a thick vorticity layer was observed. The average magnitude of the vorticity in this layer is approximately 200 s^{-1}. The plot also shows the ejecting bursts from the windward face of the wave, as was observed in figure 3.1a. The plot indicates that the bursts eject in the form of a series of counter-rotating vortices. Figure 3.2b shows the vorticity structure over the wave trough. As described in figure 3.1b, a prominent separated flow was observed over this wave trough. The plot shows that the thickness of the separated layer is comparable to the wave

height. The plot also shows that strong localized counter clockwise vortices (thin contours) are generated within the separation region that are bounded from the top and bottom by the layers of clockwise vortices. The maximum magnitude of the counter-clockwise vortices within the separated flow is approximately 500 s^{-1} while, the maximum magnitude of clockwise vortices within the top and bottom layers of clockwise vortices is approximately 900 s^{-1} and 400 s^{-1}, respectively. The flow separation process is more clearly visible in figure 3.2c where the upwind crest is moved within the camera field of view. The plot shows that the vortices are shed from the apex of the crest creating a separation region. As expected, the vortices shed from the wave crest are clockwise. The vortex dynamics associated with the sweeping process is also visible in the plot. The plot shows that the sweeping vortices are predominantly clockwise. The plot also indicates that the interaction of sweeping and separated vortices results in the vortex breakdown.

(a)

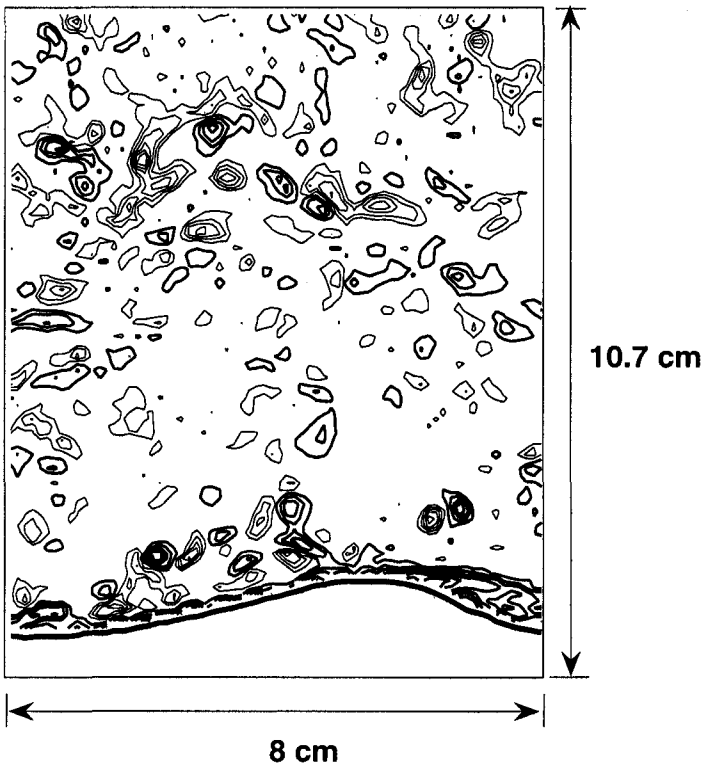

(b)

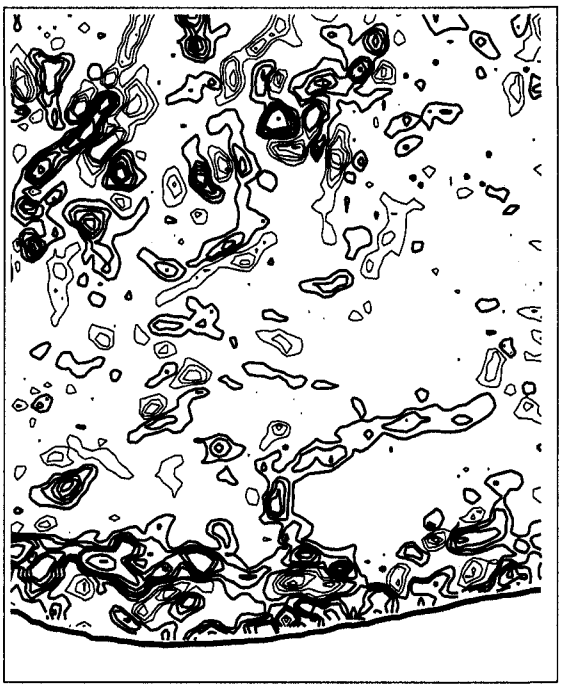

(c)

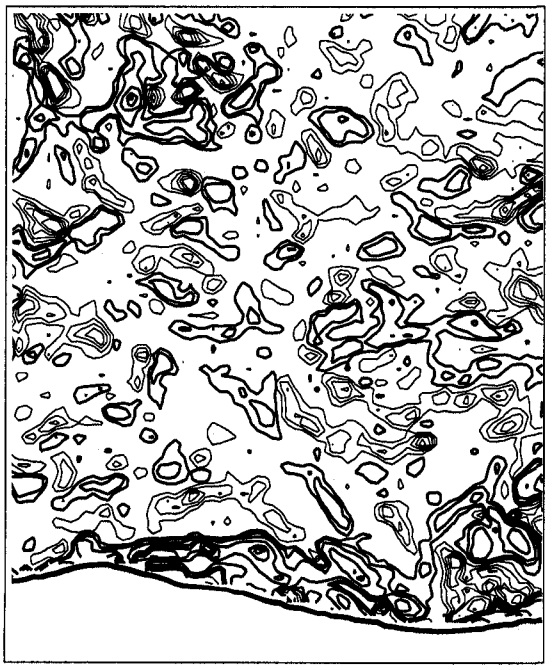

Figure 3.2(a-c): Contour plots of the instantaneous vorticity corresponding to the velocity fields shown in figure 3.1. Clockwise vorticity (thick), counterclockwise vorticity (thin)

Kawamura and Toba (1988) observed that the air bulges over the waves have a horizontal length scale corresponding to the wavelength of the waves. They also described the vertical evolution of the low speed air bulges while moving ahead with the free stream flow and argued that the source of these low speed air bulges could be the separated flow observed downwind of the wave crest. Reul et al. (1999) also observed airflow separation immediately downwind of the crest of a mechanically-generated breaking wave. They found that the separated flow was bounded by a high shear layer dominated by strong patches of clockwise vorticity. They argue that the vorticity field within the separated airflow region demonstrates the mechanism of re-entrainment of stress bearing fluid from the outer part of the shear layer to the interface.

Previous studies using point measurement techniques above the crest indicated the bursting and sweeping processes based on the spikes in the turbulent velocity data. These measurements however, cannot capture the dynamics of these processes. As shown in figure 3.1 and 3.2, the PIV technique due to high spatial resolution captures the bursting and sweeping motions spatially and temporally. This allows a good perception and deeper insight into these processes, which leads to a better understanding of the bursting and sweeping mechanisms and their overall impact on the flow field. In addition, the PIV measurements also provide a deep insight into the separation process observed very often above the wave field.

3.2. Mean Velocity and vorticity

The mean streamwise velocity was computed by time-averaging five minutes of the velocity data at each grid point and then by spatially averaging the time-averaged

velocity at each height. Figure 3.3a shows the vertical profiles of the mean streamwise velocity at different wind speeds. The plot shows that the magnitude of the streamwise velocity increased with wind speed and decreased monotonically towards the interface, as expected. As mentioned earlier, waves were observed only at wind speeds of 3.7 m s^{-1} and 4.4 m s^{-1}. At the lower wind speeds, very small ripples appear on the surface that could not be resolved within the given PIV measurements. Thus, we can consider the velocity fields at the two higher wind speeds as the flow over wavy surface and for the remaining lower wind speeds as the flow over relatively smooth surface. The plot in figure 3.3a shows differences between the velocity profiles over two different types of water surfaces. For wavy water surface the shearing effects are observed up to a greater distance from the interface. However, for the smooth water surface, these effects are restricted to a relatively shorter distance. For the wind speeds range from 1.5 m s^{-1} to 3 m s^{-1}, the magnitudes of mean streamwise velocities are higher near the water surface. For this wind speed range, the wind stress is almost entirely consisted of the tangential stress. As the wind speed further increased to 3.7 m s^{-1}, waves appeared on the water surface and the mean streamwise velocity near the interface was reduced by 15% compared to that at 3.0 m s^{-1}. When waves form on the water surface, the wind stress is partitioned into tangential and wave components. The reduction in the mean velocity at 3.7 m s^{-1} is due to the reason that the magnitude of the tangential stress is decreased because of the wave formation at this wind speed. The mean streamwise velocity again started to increase with an increase in the wind speed. At 4.4 m s^{-1}, the mean velocity is increased by 10% compared to that at 3.7 m s^{-1}, however, it is still lower than that at 3.0 m s^{-1}. Banner and Peirson (1998) measured the total and tangential stresses beneath the water surface. They found that at short fetches and lower wind speeds, the tangential

stress constitutes almost 50% of the total stress. They further observed that this fraction decreases with an increase in fetch and wind speed. Kudryavtsev and Makin (2001) investigated the impact of airflow separation on the drag of the sea surface and argued that at low wind speeds, the tangential stress dominates the surface drag while the role of the waveform drag is negligible. With an increase in the wind speed, the role of the waveform drag becomes pronounced. At wind speed $U_{10} > 10$ m s^{-1}, the surface drag is mainly supported by the wave induced and turbulent stresses. This fact is due to enhanced surface roughness which creates turbulence and decreases the relative speed of the air flow within few centimeters above the waves. The mean velocity profiles on the semilog scale are shown in figure 3.3b. The profiles show the logarithmic behaviour in the near surface region which is consistent with the previous studies (e.g. Wu 1975).

The mean vorticity was computed by averaging the vorticity data at each height temporally and spatially. The vertical profiles of the mean vorticity are plotted in figure 3.4a as a function of height. The plot shows that the magnitude of vorticity is largest near the water surface which decreased with height and became almost negligible 3-4 cm above the water surface. From a height of 2 cm to the water surface, the vorticity was enhanced by approximately an order of magnitude at all wind speeds. This indicates that the enhanced vorticity layer is confined to a small region immediately adjacent to the water surface. The plot also shows that the enhancement of vorticity in the presence of waves is significant compared to that over relatively smooth surfaces.

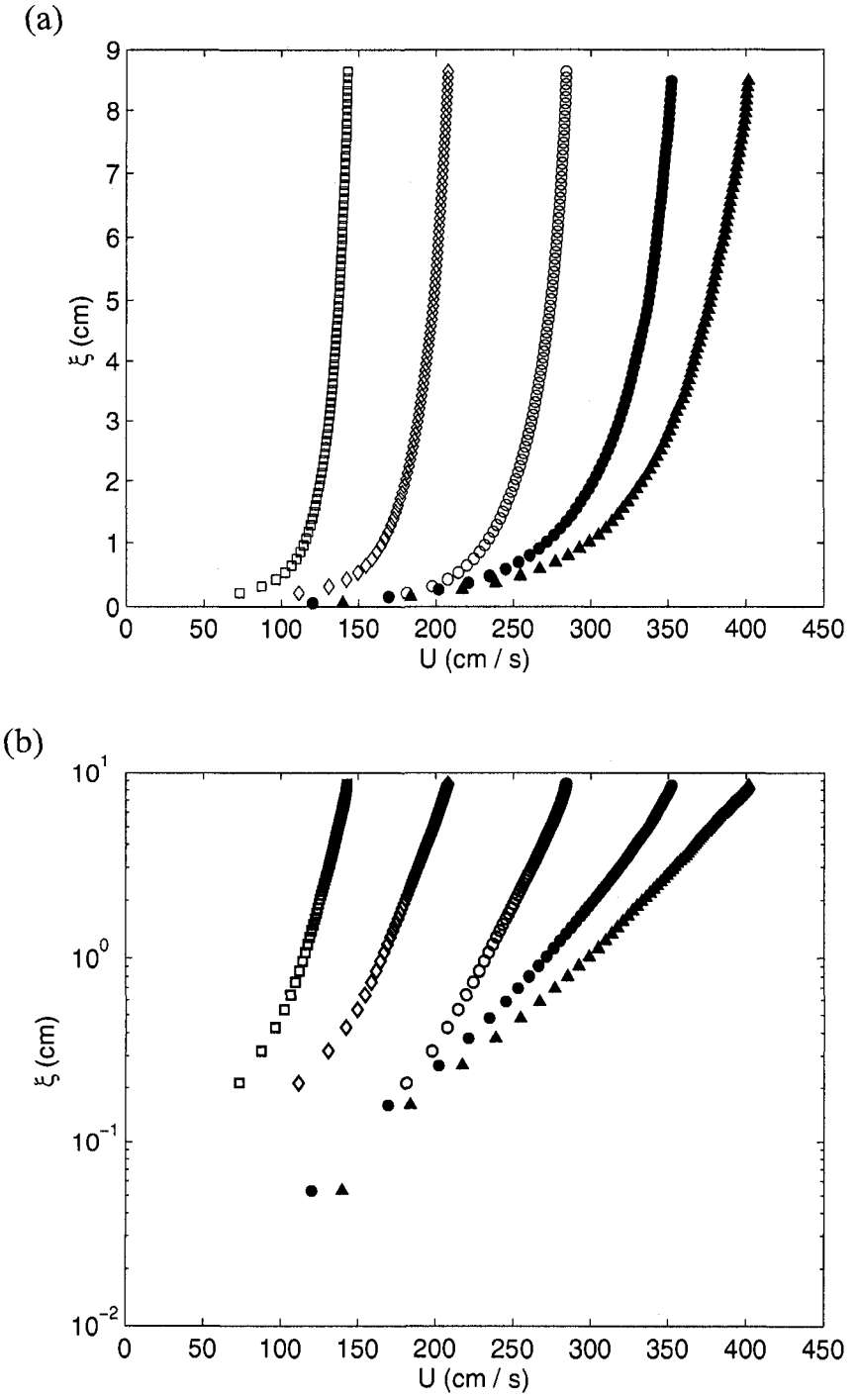

Figure 3.3: Vertical profiles of the mean horizontal velocity at different wind speeds, (a) normal scale (b) semi-logarithmic scale (symbols: ▲, =4.4 m s^{-1}; ●, =3.7 m s^{-1}; ○, =3 m s^{-1}; ◊, =2.1 m s^{-1}; □, =1.5 m s^{-1}). The values are averaged over 5 minutes of data

For the smooth surface, as the wind speed increased from 1.5 m s^{-1} to 3 m s^{-1}, the mean vorticity immediately above the interface increased by 86.5 s^{-1} whereas, in the presence of waves when the wind speed increased from 3 m s^{-1} to 4.4 m s^{-1}, the mean vorticity at the interface was increased by 215 s^{-1}.The enhanced vorticity in the presence of waves could be due to the increase in the surface roughness and flow separation. The higher vorticity magnitude near the interface indicates the presence of strong vortices, which implies the presence of strong turbulence in the near surface region. These vortices also disrupt the concentration and thermal boundary layers thus enhancing the transfer of mass and heat across the interface. The plot also shows that at all wind speeds clockwise vorticity is dominant.

The vertical profiles of mean vorticity on the logarithmic scale are plotted in figure 3.4b. All profiles (with and without waves) show similar height dependency within the height from approximately 3 mm to 30 mm, where the mean vorticity decays as $\xi^{-1.25}$. However, at lower heights, the mean vorticity found to be almost constant in the presence of waves. For no wave cases this trend cannot be described in this region due to the unavailability of the data.

As described in the introduction section, most of the previous studies used point measurement techniques to measure airside velocity field. They typically installed measuring probes at heights ranging from 4 cm to 20 cm above the fluctuating water surface. At this height, the vorticity magnitude is expected to be very small. This could be the reason why previous airside studies did not observe enhanced vorticity layer in the measured velocity fields in the near surface region above the air-water interface. The studies using flow visualization techniques to investigate the flow structure in the near-surface region, however, indicated the presence of high vorticity layer.

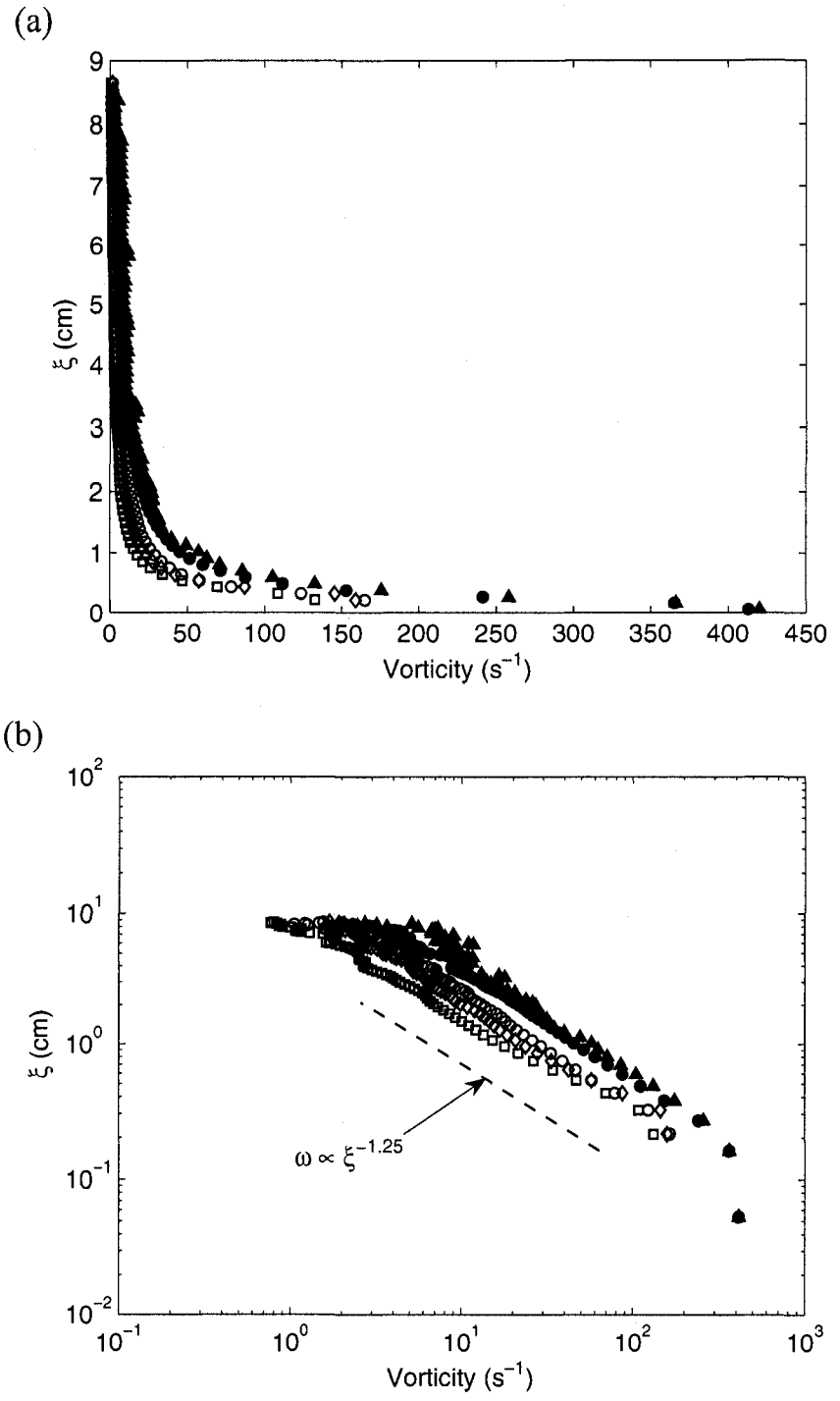

Figure3.4: Profiles of the mean vorticity at different wind speeds, (a) normal scale (b) logarithmic scale (symbols: ▲, =4.4 m s^{-1}; ●, =3.7 m s^{-1}; ○, =3 m s^{-1}; ◊, =2.1 m s^{-1}; □, =1.5 m s^{-1}). The values are averaged over 5 minutes of data

Kawamura and Toba (1988) and Komori et al. (1993) qualitatively described the layer of high vorticity as organized flow patterns immediately above the waves. Through the snapshots of the instantaneous fields, Reul et al. (2008) also showed the presence of high vorticity layer in the near-surface region. They observed that the vorticity layer departs from the interface at a point slightly downwind of the crest and reattached around the wave trough. To the best of our knowledge, the present study is the first to quantify the high shear layer immediately above the wind-sheared water surface. The results presented in figure 3.4 show the significance of near surface dynamics.

3.3. Turbulent Flow Characteristics

PIV measurements provide instantaneous velocity fields. Conventionally, the instantaneous velocity comprised of two components; mean and turbulent. However, in the presence of waves, a third component is also induced which is known as the wave-induced velocity. Therefore, instantaneous velocity over the wavy water surface is the sum of mean, wave-induced and turbulent velocities. The computation of the wave-induced velocity component is a challenging task, which is obtained by subtracting the time-averaged mean velocity from the phase-averaged mean velocity (Hussain and Reynolds 1970). In the studies of airflow over wavy water surfaces, one group of researchers have computed all three velocity components (e.g. Hussain and Reynolds 1970, Hsu and Hsu 1983, Mastenbroek et al. 1996, Mate et al. 2001), while the other group of researchers used the conventional method and computed the so-called fluctuating velocity component by subtracting the time-averaged mean velocity from the instantaneous velocity (e.g. Kawamura et al. 1981, Kawai 1982, Kawamura and Toba

1988). As the present work is more focused on the demonstration of the suitability of the PIV technique for near-surface velocity measurements in the presence of waves, we used the simpler approach and presented different properties of the total fluctuating velocity component, which is comprised of wave-induced and turbulent velocity components (Kato and Sano 1971). That is, for all wind speeds, with and without waves, the total fluctuating horizontal and vertical velocities u_f and v_f were computed by subtracting the mean velocities from their respective instantaneous velocities. The Reynolds stress is computed as $-\overline{u_f v_f}$ and is presented in figure 3.5 versus the height at different wind speeds. Since u_f and v_f include both the wave-induced and turbulent velocities therefore, the computed term $-\overline{u_f v_f}$ represents the total Reynolds stress (Kato and Sano 1971). The plot shows that for the wind speeds range of 1.5 to 3 m s^{-1} where the flow is over smooth water surface, the Reynolds stress increased gradually with the distance from the fluctuating water surface to a certain height and then decreased towards the outer region where it almost vanished. However, at wind speeds of 3.7 m s^{-1} and 4.4 m s^{-1} i.e. the flow over wavy water surface, the Reynolds stress increased sharply up to a vertical distance of 1.12 cm and then decreased with height which indicates that the waves produced strong turbulence in the near surface region. The Reynolds stress distribution over the wavy water surface also indicates that the effect of this turbulence is not restricted to the inner surface region but has also extended to the outer region. Figure 3.5 shows that the increase in Reynolds stress is significant within the vertical distance of 1.5 cm from the fluctuating air-water interface.

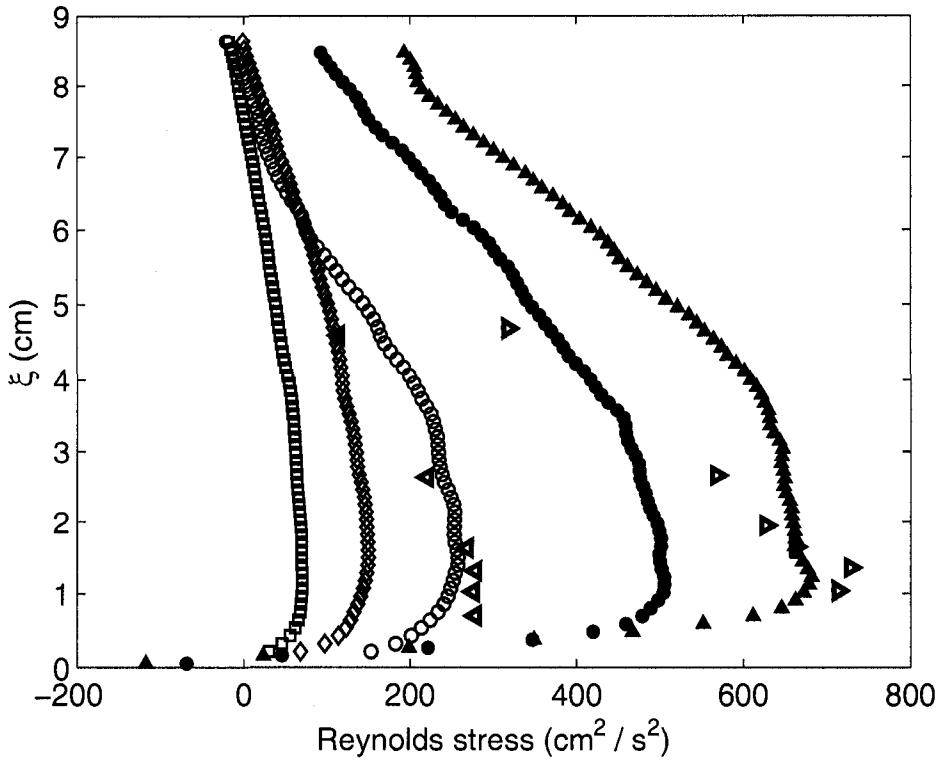

Figure 3.5: Reynolds stress versus height (symbols: ▲, =4.4 m s^{-1}; ●, =3.7 m s^{-1}; ○, =3 m s^{-1}; ◊, =2.1 m s^{-1}; □, =1.5 m s^{-1}). The values are averaged over 5 minutes of data. ◁, = 4.18 m s^{-1}; ▷, = 5.90 m s^{-1} from Kawamura et al. (1981)

Kawamura et al. (1981) investigated the turbulent structure of airflow over wind generated water waves using Pitot static tube and hotwire anemometry. The measurements were taken at a fetch of 3 m and at wind speeds of 4.18 and 5.90 m s^{-1}. At the wind speed of 4.18 m s^{-1} they observed small ripples of negligible wave height (i.e. smooth surface) whereas, at a wind speed of 5.90 m s^{-1}, they observed waves with significant wave height of 0.28 cm (i.e. wavy surface). The Reynolds stress data from Kawamura et al. (1981) is also plotted in figure 3.5 for comparison. Figure 3.5 shows that

for both surface conditions, a good agreement is observed between the present data and that of Kawamura et al. (1981). Their data shows that in the presence of waves at the wind speed of 5.9 m s^{-1}, the Reynolds stress increased with decreasing height except at the lowest measurement point where it decreased. The peak value is observed at a height of 1.35 cm from the water surface which is about 20% higher than the location of the maximum Reynolds stress reported in the present study. This difference could be due to the higher free stream velocity. Kato and Sano (1971) investigated the turbulent structure of airflow over coexisted mechanically generated waves and wind waves using hot wire anemometer. The wave heights were 6 and 7 cm at wind speeds of 6.3 and 9.5 m s^{-1}, respectively. The measurements were taken at a fetch of 18.75 m and at a height of 4 cm and above, the wave crest. They reported that the Reynolds stress increased with decreasing height and have attained maximum value at 5 cm and 8 cm above the wave crest for the wind speed of 6.3 m s^{-1} and 9.5 m s^{-1} respectively. However, below this height the Reynolds stress decreased towards the water surface to the lowest measurement point. This trend is also consistent with the presented results.

The comparison of the Reynolds stress profiles of figure 3.5 also shows that for the flow over smooth water surface, near the interface the Reynolds stress is positive and increased with wind speed. Whereas for the case of flow over the water waves an opposite trend is observed, that is the Reynolds stress close to the interface is negative and the magnitude of the negative Reynolds stress increased with an increase in the wind speed. Kato and Sano (1971) and Kawamura et al. (1981) also reported a decreasing trend in the Reynolds stress from its peak as approaching the water surface. However, due to the limitations of their measurement techniques, they were not able to conduct measurements in the close vicinity of the fluctuating water surface. This could be the

reason why they did not observe negative Reynolds stress at the interface. The observation of the negative Reynolds stress immediately above the water surface in the presence of waves is a unique featured observed in the present study. In general, the positive Reynolds stress indicates the transport of the turbulent part of the momentum flux towards the surface (Friebel 2005). Using the same analogy, the negative Reynolds stress could correspond to the momentum flux transported from the fluctuating water surface to the wind. Hristov et al. (1998) segregated the fluctuations of velocity induced by the waves from that due to the shear driven turbulence and observed positive and negative wave-coherent momentum fluxes. They attributed the positive wave-coherent flux to the momentum transferred from wind to waves and vice versa. This issue is related to the separation of wave-induced component from the fluctuating velocity field. This issue is beyond the scope of the present chapter and is a part of next chapter. The present study demonstrates that the PIV technique enable us capturing the fluctuations in the velocity components accurately in the crest-trough region immediately above the wave.

The rate of energy production is computed using the relation,

$$P = -\overline{u'v'}\frac{dU}{dy} \tag{3.1}$$

where, $-\overline{u'v'}$ is the Reynolds stress and $\frac{dU}{dy}$ is the mean streamwise velocity gradient (Pope 2000). Vertical profiles of the energy production are plotted in figure 3.6 at different wind speeds. The plot shows that for the wind speeds ranging from 1.5 m s^{-1} to 3 m s^{-1} the energy production is large near the water surface. It increased within the height of 3 mm from the interface and then approached zero at heights 4 cm and above. This is due to very small magnitudes of Reynolds stress and mean-velocity gradients in the outer

region. In the presence of waves at wind speeds of 3.7 m s^{-1} and 4.4 m s^{-1}, negative values of the energy production are observed in the region immediately above the wavy water surface. The energy production increased sharply to a maximum positive value at a height of approximately 5 mm and then decreased to zero at the height of approximately 7 cm. The negative value of the energy production at the interface is primarily due to negative Reynolds stress at the interface. The term energy production quantifies the exchange of kinetic energy between the mean flow and the turbulence. Positive energy production represents the energy lost by the mean flow to the turbulence, whereas, the negative energy production indicates the energy lost by the turbulence to the mean flow. A sustainable inverse energy transfer is possible only if any external force acts on both the field of fluctuating velocity and on the velocity derivative (Liberzon et al. 2005). Therefore, the region of negative energy production may be governed by different physical mechanisms, which could be attributed due to the wave-turbulence interaction in the near surface region. The present chapter is mainly focused on the measurement technique used to capture the flow dynamics within crest-trough region above the wave therefore the authors restricted themselves to the basic results.

Figure 3.5 and 3.6 clearly demonstrate that the airflow structure immediately above the crest-trough region of the wave is different from that observed at a certain height above the wave crest. The production profiles in figure 3.6 show that in the presence of waves, the peak energy production lies within a distance less than the significant wave height. This implies that the maximum energy production occurs within the crest-trough region. Thus, any measurement taken above the wave crest may not capture the maximum production.

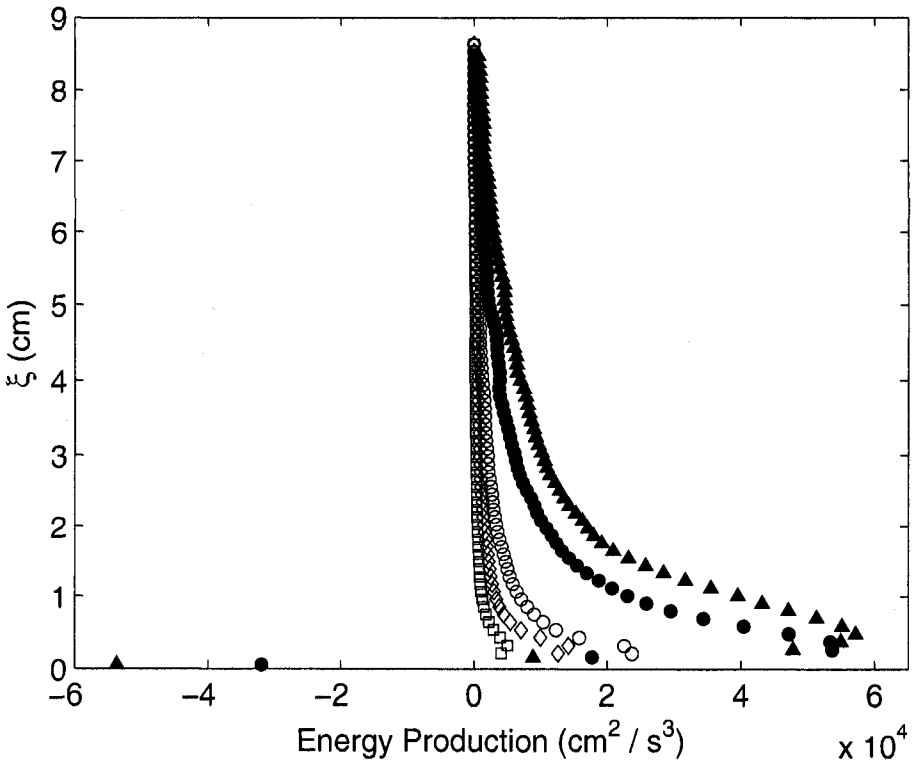

Figure 3.6: Energy Production versus height (symbols: ▲, =4.4 m s^{-1}; ●, =3.7 m s^{-1}; ○, =3 m s^{-1}; ◊, =2.1 m s^{-1}; □, =1.5 m s^{-1}). The values are averaged over 5 minutes of data

Doron et al. (2001) compared different methods of estimating the rate of energy dissipation (ε) using PIV and showed that the method that uses the velocity gradients from the two-dimensional PIV turbulent velocity fields is the most accurate. According to that method, ε can be computed as,

$$\varepsilon = 3\upsilon\left[\overline{\left(\frac{\partial u'}{\partial x}\right)^2} + \overline{\left(\frac{\partial v'}{\partial y}\right)^2} + \overline{\left(\frac{\partial u'}{\partial y}\right)^2} + \overline{\left(\frac{\partial v'}{\partial x}\right)^2} + 2\overline{\left(\frac{\partial u'}{\partial y}\frac{\partial v'}{\partial x}\right)} + \frac{2}{3}\overline{\left(\frac{\partial u'}{\partial x}\frac{\partial v'}{\partial y}\right)}\right] \tag{3.2}$$

where $\frac{\partial u'}{\partial x}$ is the streamwise velocity gradient in the horizontal direction, $\frac{\partial u'}{\partial y}$ is the streamwise velocity gradient in the vertical direction, $\frac{\partial v'}{\partial x}$ is the transverse velocity gradient in the horizontal direction and $\frac{\partial v'}{\partial y}$ is the transverse velocity gradient in the vertical direction. The over bar denotes time averaging (Doron et al. 2001). The profiles of energy dissipation rate are plotted in figure 3.7a, at different wind speeds. The plot shows that the rate of energy dissipation increases with wind speed. At all wind speeds the rate of energy dissipation is maximum near the water surface, decreases with height and become almost constant at heights 1-3 cm above the fluctuating water surface. For the case of flow over smooth water surface at wind speed range of 1.5 m s^{-1} to 3 m s^{-1}, the dissipation rate immediately adjacent to the interface is on average a factor of 4.5 higher than that at heights greater than 2 cm. However in the presence of wave at wind speeds of 3.7 m s^{-1} and 4.4 m s^{-1}, the dissipation rate immediately adjacent to the interface is approximately a factor of 7 higher than that at heights greater than 2 cm. This indicates a significant enhancement in the dissipation rate in the presence of waves in the near-surface region. The data in figure 3.7a also indicates that the influence of near surface turbulence over wavy water surface is extended to greater heights as compare to the smooth water surfaces.

The profiles of the dissipation rate are plotted on the logarithmic scale in figure 3.7b. The plot shows that within the height from approximately 2 mm to 10 mm, all profiles (with and without waves) show similar height dependency where the dissipation rate decays as $\xi^{-4/5}$. Within 2 mm from the surface the dissipation profiles in the presence of waves show a different height dependency where the dissipation rate decays as $\xi^{-1/2}$.

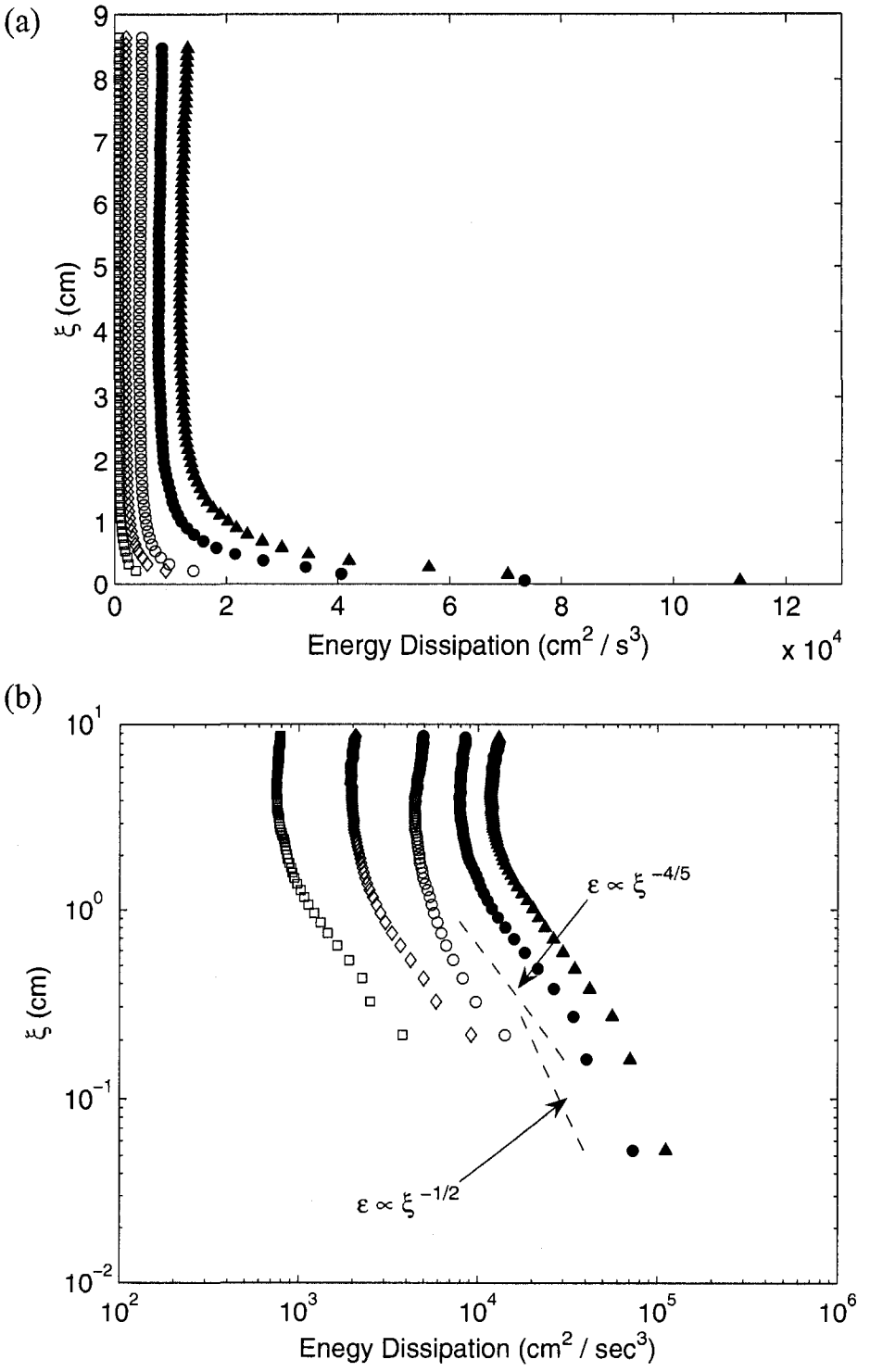

Figure 3.7: Energy dissipation versus height, (a) normal scale (b) logarithmic scale (symbols: ▲, =4.4 m s^{-1}; ●, =3.7 m s^{-1}; ○, =3 m s^{-1}; ◊, =2.1 m s^{-1}; □, =1.5 m s^{-1}). The values are averaged over 5 minutes of data

The behaviour at lower wind speeds (no wave cases) cannot be described in this region due to the unavailability of the data.

As discussed earlier, literature review shows that due to the measurement difficulties, in most of the previous studies, researchers measured velocity at a fixed point located above the wave crest therefore they were not able to quantify significantly enhanced magnitudes of fluctuating velocity gradients and the rate of energy dissipation immediately above the fluctuating air-water interface. The present results show that the dissipation rates are significantly enhanced within the crest-trough region that could not be estimated from the measurements above the wave crest.

The presented results clearly indicate that the waves significantly enhance near surface turbulence. This enhanced turbulence rapidly transfer air to and from the interface, through bursting and sweeping processes (as was observed in figure 3.1). Previous studies provide qualitative evidence that the wind generated waves enhanced airside turbulence in the immediate vicinity of the water surface. However, due to measurement difficulties, the quantitative analysis of turbulence within the crest-trough region above the water surface is not well reported. The present results demonstrate that the non-intrusive PIV technique could accurately measure the velocity field within and above the crest-trough region. The above results also demonstrate that the measurements taken in the far field above the water surface cannot capture the near-surface turbulence dynamics that is responsible for controlling the transport of mass, momentum and heat fluxes between the two fluids.

CHAPTER 4

Wave-induced flow structure over wind-generated water waves

In this chapter various mean, turbulent and wave-induced properties are described in the close vicinity of the wave and their variation is discussed as a function of the phase and height.

4.1. Instantaneous and wave induced velocity fields

The oscillatory motion of the waves modulates the structure of the airflow field above them and therefore, it is different from that over a solid surface. (Grachev and Fairall 2000). The wave-induced velocity quantifies the contribution of the wave motion to the flow field and provides fundamental understanding about the flow pattern induced in the near surface region, immediately above the waves. The phase-averaged wave-induced velocity field at a wind speed of 4.4 m s^{-1} is presented in figure 4.1, as a function of phase. The figure shows that the magnitude of phase-averaged wave-induced velocity is significant in the near surface region, as expected. At a distance of approximately three times the significant wave height from the fluctuating water surface, the wave-induced velocity magnitude becomes negligible. Figure 4.1 shows two distinct flow structures in the near-surface region. The wave-induced velocity vectors over the crest (phase angle from -90° to 90°) are in the direction of the wave propagation whereas the wave-induced velocity vectors over the trough (phase angle from 90° to 270°) are in the direction opposite to the wave propagation.

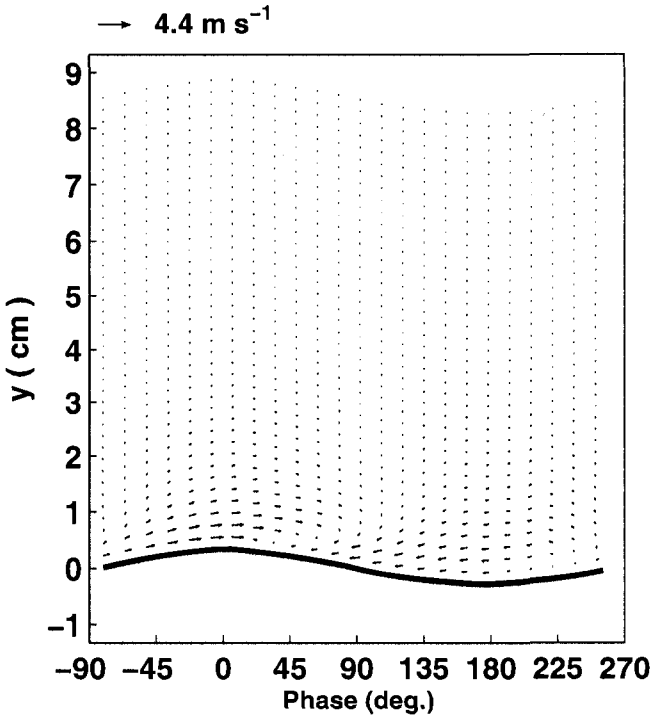

Figure 4.1: Phase-averaged wave induced velocity field at a wind speed of 4.4 m s^{-1}

The PIV data with high spatial resolution in the present study enabled us to capture small-scale structures within and above the crest-trough region, which is very crucial to improve fundamental understanding of the dynamical processes in this region. Figure 4.2a shows an instantaneous velocity field with a wave crest within the field of view, measured at a wind speed of 4.4 m s^{-1}. The plot also shows a burst on the windward side of the crest that is merging into the free stream flow. The flow separation on the leeward side of the wave crest is also visible in the plot, which is attached further downwind of the wave. The sweeping process is also observed in the region where the separated flow re-attaches to the air-water interface (lower right hand side of the plot).

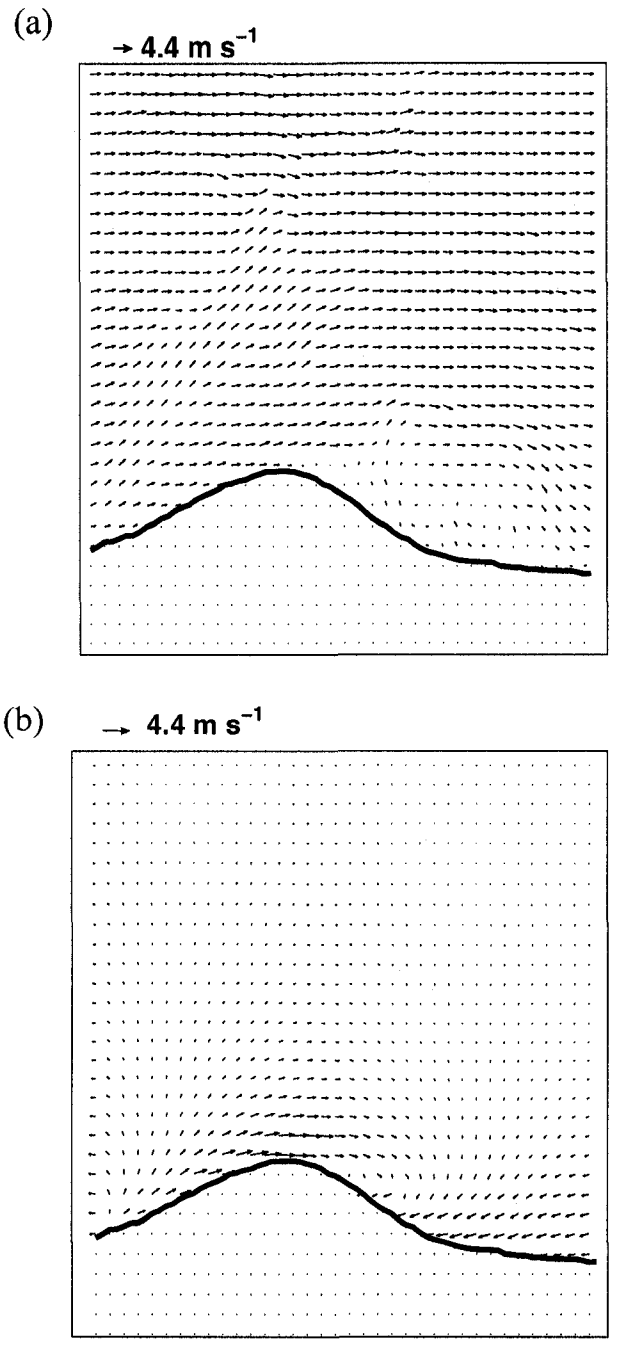

Figure 4.2: (a) An instantaneous velocity field at a wind speed of 4.4 m s^{-1}; (b) corresponding wave induced velocity field.

Shaikh and Siddiqui (2008) presented and discussed the bursting, sweeping and airflow separation processes. They reported that on the windward face of the wave, the

bursts eject as a series of counter rotating vortices. The region occupied by the burst is long and narrow, and appears to grow as it proceeds downstream. A thick layer of strong clockwise vortices was also reported within the separation zone. They observed sweeping process in the region where the separated flow attaches to the water surface and argued that the bursting and sweeping processes over the moving water surface are qualitatively similar to that over the solid wall.

The 2D wave-induced velocity field corresponding to the instantaneous velocity field in figure 4.2a is plotted in figure 4.2b. The plot shows the instantaneous behaviour of the wave-induced velocity field. The behaviour is similar to that observed in figure 4.1 and shows the two distinct flow regimes immediately above the interface.

Figures 4.1 and 4.2b qualitatively describe the spatial structure of the wave-induced velocity fields within and above the crest-trough region. To obtain a better insight into the flow dynamics above the waves, different flow characteristics are analyzed as a function of wave phase. The results are plotted at eight different phases 45° apart that covers the entire waveform. The profile of phase-averaged surface displacement at 4.4 m s^{-1} is also plotted in the figures. This allowed a better perception of the variation in the flow behaviour with respect to the waveform.

4.2. Phase-averaged wave-induced velocity

The vertical profiles of the streamwise component of the normalized phase-averaged wave-induced velocity are presented in figure 4.3, at the two wind speeds. The figure shows that the magnitude of wave-induced velocity is significant only within a distance of one to two wave heights from the surface. At both wind speeds its magnitude

approaches zero at a height equal to or greater than three times the significant wave height above the mean water level. This indicates that in the outer region, the waves have no effect on the flow field.

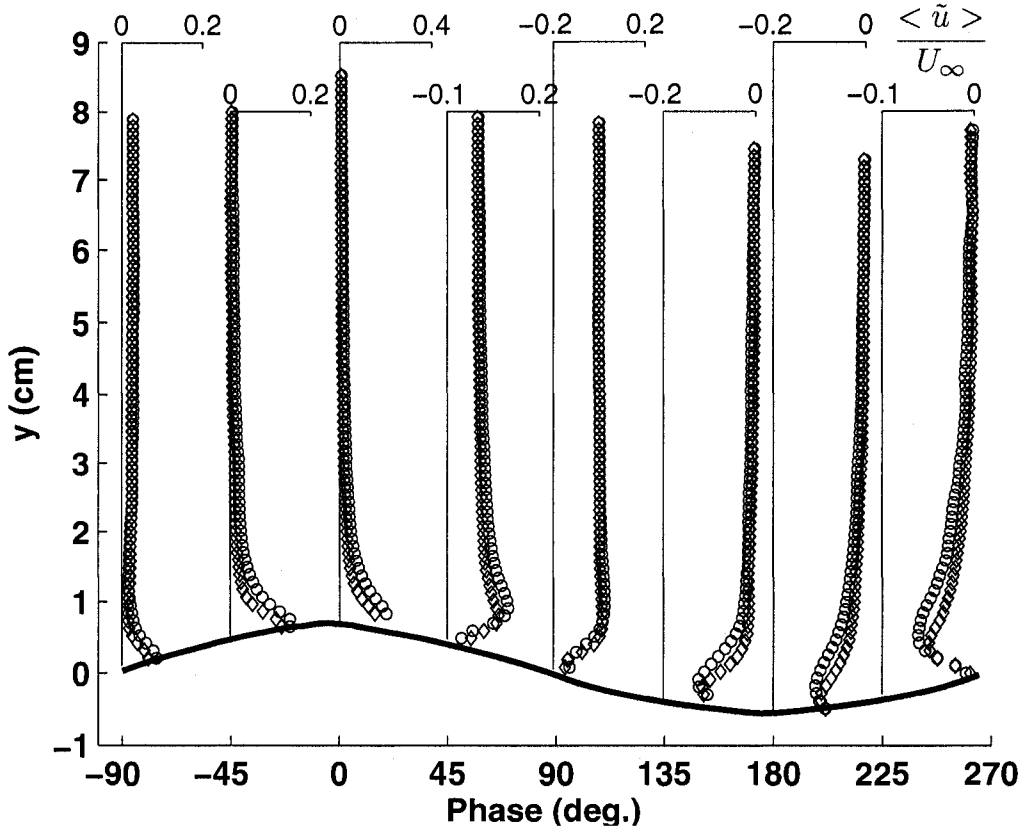

Figure 4.3: Vertical profiles of the normalized phase-averaged wave-induced velocity versus the phase, (Symbols: ○, =4.4 m s^{-1}; ◊, =3.7 m s^{-1}). U_∞ is the free stream velocity.

The figure shows two distinct trends of the wave-induced velocity profiles as shown earlier in figure 4.1. In the near-surface region over the wave crest, the wave-induced velocity is positive whereas, over the wave trough, the wave-induced velocity is negative. The profiles at both wind speeds follow the same trends. The maximum velocity magnitude at each phase occurred within a distance of RMS wave height. At all heights, the largest magnitude of the positive wave-induced velocity is observed at the wave crest and the largest magnitude of the negative velocity is observed at the phase 90° which is the core of the separated flow region. Over the entire waveform, the velocity magnitude is largest at the wave crest at all heights.

4.3. Phase-averaged streamwise velocity

Figure 4.4 shows the phase-averaged streamwise velocity as a function of wave phase and height, at wind speeds of 3.7 and 4.4 m s^{-1}. The plot shows that the magnitude of phase-averaged streamwise velocity decreased monotonically towards the interface, as expected. The maximum streamwise velocity was observed at a phase angle of 0°, immediately above the crest, which is 45% of the free stream velocity, whereas the minimum streamwise velocity was observed at a phase angle of 180°, immediately above the trough which is 20% of the free stream velocity. The figure also shows that within a 1 cm thick layer immediately above to the water surface, the streamwise velocity decreases with the phase on the leeward side (0° to 180°) and increases with the phase on the windward side (180° to 0°).

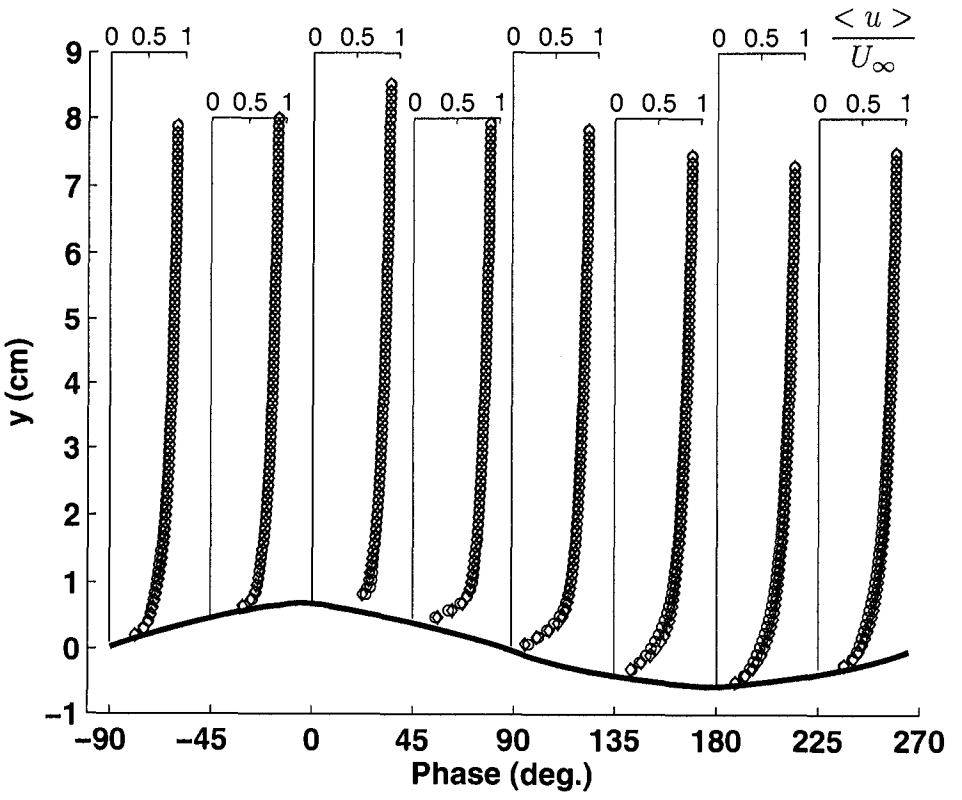

Figure 4.4: Vertical profiles of the normalized phase-averaged streamwise velocity as a function of phase, (Symbols: ○, =4.4 m s^{-1}; ◊, =3.7 m s^{-1})

4.4. Phase-averaged vorticity

The vertical profiles of the phase-averaged vorticity are plotted in figure 4.5 at wind speeds of 3.7 and 4.4 m s^{-1} at different phases. The plot shows that the vorticity profiles at both wind speeds collapsed well, indicating that the vorticity structure is similar at both wind speeds. The magnitude of vorticity is largest near the water surface which decreased with height and became almost negligible 2 cm above the mean water level. This indicates that the enhanced vorticity layer is confined to a small region immediately adjacent to the water surface. The magnitude of vorticity is positive over the entire wavelength indicating that at both wind speeds clockwise vorticity is dominant.

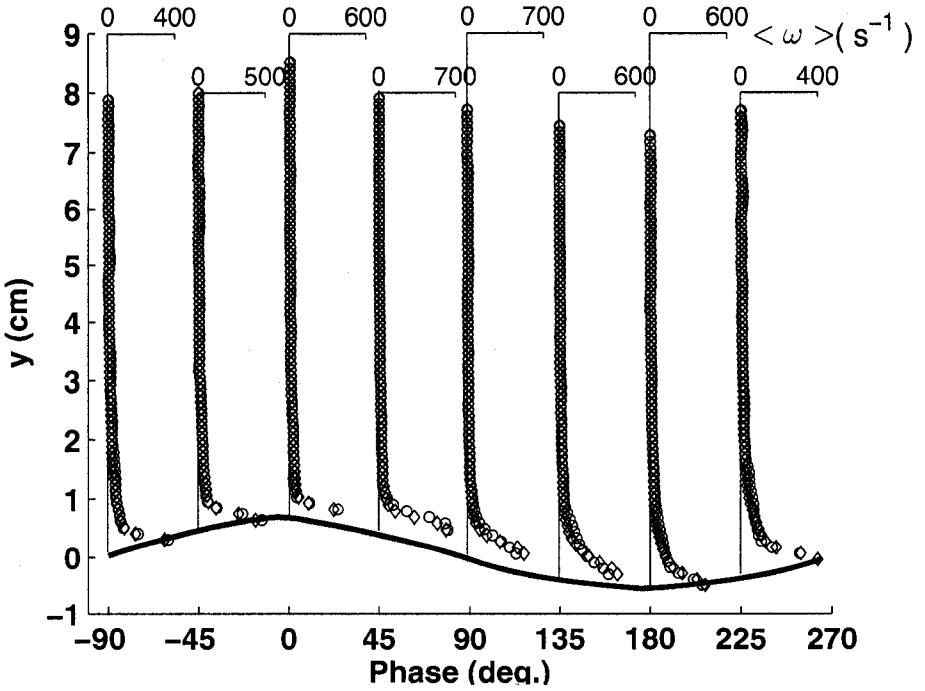

Figure 4.5: Vertical profiles of the phase-averaged vorticity as a function of phase, (Symbols: ○, =4.4 m s^{-1}; ◊, =3.7 m s^{-1})

The plot also shows that the vorticity variation with height is different at different phases. The thickness of the enhanced vorticity layer is minimum above the crest and maximum above the trough. The results also indicate that the vorticity magnitude is largest in the separation zone. The higher vorticity magnitude near the interface indicates the presence of strong vortices, which implies the presence of strong turbulence in the near surface region. These vortices disrupt the concentration and thermal boundary layers thus, enhancing the transfer of mass and heat across the interface. Reul et al. (1999) presented instantaneous snap shots of the PIV velocity and vorticity fields, computed within the crest-trough region above mechanically-generated breaking waves. They also observed strong patches of clockwise vorticity, dominant within the separated flow region downwind of the crest, which is consistent with the results presented in figure 4.5. They

argued that the vorticity field within the separated airflow region demonstrates the mechanism of re-entrainment of stress bearing fluid from the outer part of the shear layer to the interface.

4.5. Phase-averaged wave-induced vorticity

The vertical profiles of the phase-averaged wave-induced vorticity are presented in figure 4.6. The plot shows that at both wind speeds, the wave-induced vorticity is significant only in the near surface region. The plot also shows that at a given phase, the vorticity magnitude increased with height in the region immediately adjacent to the water surface, and then decreased towards zero magnitude at greater heights.

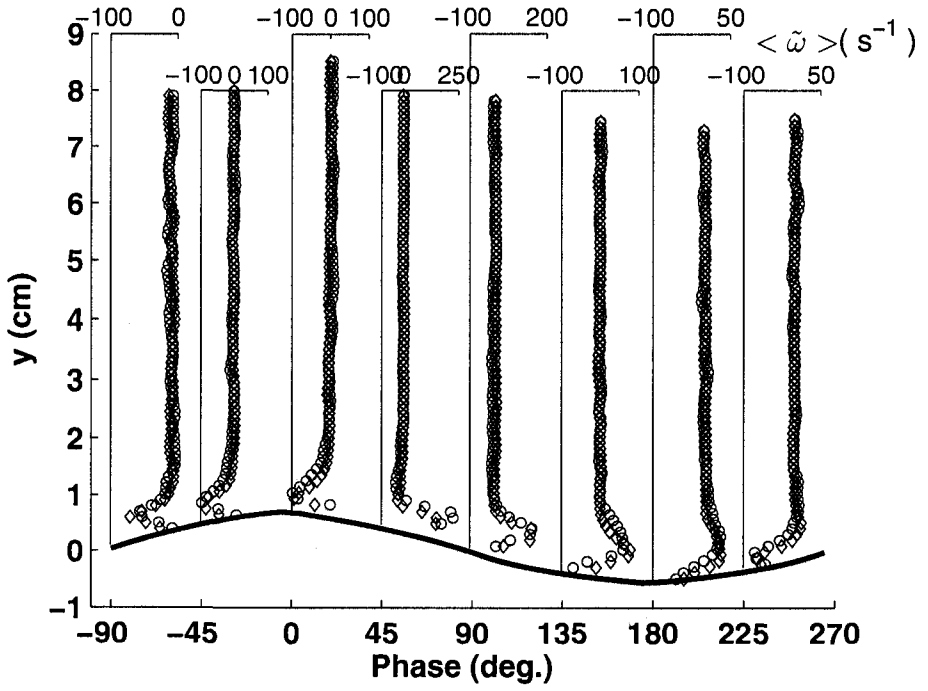

Figure 4.6: Vertical profiles of the phase-averaged wave-induced vorticity as a function of phase, (Symbols: ○, =4.4 m s^{-1}; ◊, =3.7 m s^{-1}).

The peak vorticity occurred at a height approximately equal to 5 mm. It is also observed that the phase-averaged wave-induced vorticity changes its sign systematically with height. The distribution of wave-induced vorticity over the windward face of the wave is different from that observed over the leeward face. As discussed in figures 4.2 and 4.3, it is due to the change in the direction of the wave-induced velocity on the windward and leeward sides of the wave. The figure also indicates similar trends at both wind speeds.

The momentum flux, (or wind stress) is the main focus in many previous laboratory and field studies. For the flow over a solid surface, tangential and turbulent Reynolds stresses describe the transport of momentum from the core to the surface. However, for the flow over a wavy water surface, wave-induced motion gives an additional stress component known as the wave-induced Reynolds stress. In the studies of airflow over wavy water surfaces, one group of researchers have computed both turbulent and wave-induced components of the Reynolds stress (e.g. Hussain and Reynolds 1970, Hsu and Hsu 1983, Mastenbroek et al. 1996, Mate et al. 2002), while the other group of researchers used the conventional method and computed the total Reynolds stress from the so-called fluctuating velocity components, that is, the difference between the instantaneous velocity and the time-averaged mean velocity (e.g. Kawamura et al. 1981, Kawai 1982, Kawamura and Toba 1988). In order to understand the individual contributions of the turbulent and wave-induced components of the Reynolds stress over different phases of the wave, we have analyzed the total Reynolds stress as well as the turbulent and wave-induced components of the total Reynolds stress. The total Reynolds

stress is defined as $-\overline{u_f v_f}$ where the subscript f indicates the fluctuating component obtained by subtracting the mean velocity from the corresponding instantaneous velocity.

4.6. Phase-averaged total Reynolds stress

Figure 4.7 shows the vertical profiles of the phase-averaged total Reynolds stress. Two distinct groups of total Reynolds stress distribution are also observed in figure 4.7 that correspond to the Reynolds stress distribution on the windward and leeward faces. On the leeward face, the total Reynolds stress profiles show the classical trend. That is, the Reynolds stress increased with height within the near-surface (inner) region and then decreased to zero towards the free stream region. On the windward face, the total Reynolds stress is negative within a thin layer, immediately above the interface. The magnitude of the negative Reynolds stress decreases with height and the Reynolds stress becomes positive at heights approximately equal to 5 mm. At greater heights, the Reynolds stress profiles show the classical trend. The positive Reynolds stress indicates the transfer of momentum flux towards the surface, and vice versa (Friebel 2005). The negative Reynolds stress observed along the windward face of the crest indicates that in this portion of the wave, the net transfer of momentum is in the upward direction that is from wave to wind whereas along the leeward face of the crest, the plot indicates downward momentum transfer that is from wind to the wave. Another interesting observation is that in the near surface region, the increase in the magnitude of Reynolds stress with wind speed is more significant between 0° and 135°. This is the region where the flow separation occurs.

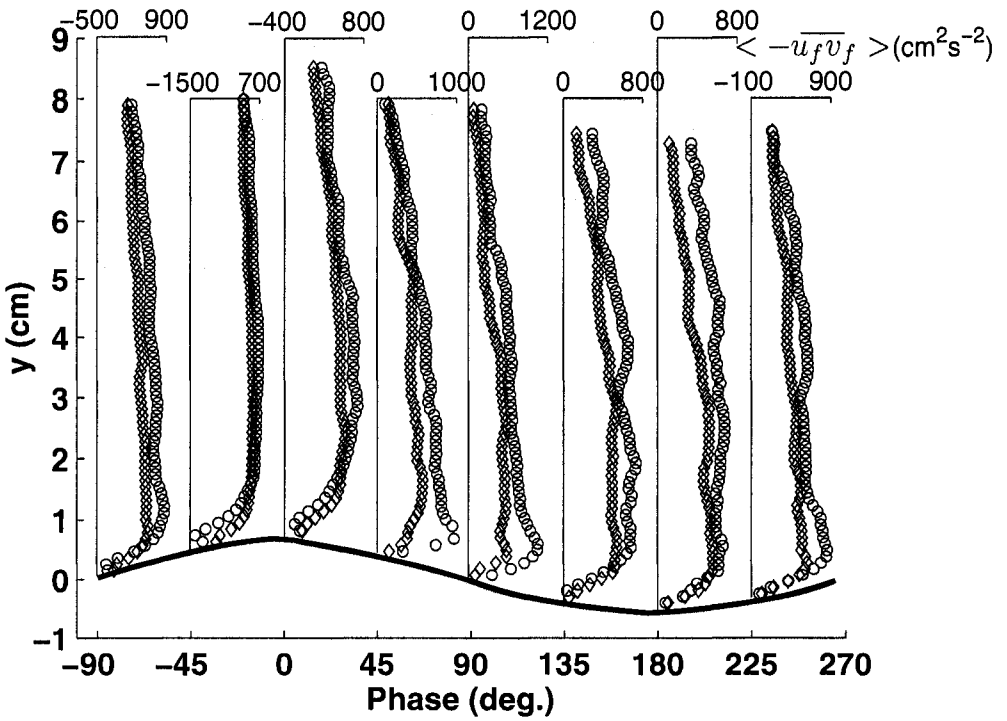

Figure 4.7: Vertical profiles of the phase-averaged total Reynolds stress as a function of phase, (Symbols: ○, =4.4 m s^{-1}; ◊, =3.7 m s^{-1})

We have identified the separated and non-separated flow through a visual inspection of all velocity fields at both wind speeds. It was found that the flow was separated in approximately 45% and 28% of the velocity fields at 4.4 m s^{-1} and 3.7 m s^{-1} wind speeds, respectively. Thus, the significant increase in the Reynolds stress in this region at the higher wind speed is due to a substantial increase in the waves with flow separation. Therefore, it can be argue that the momentum transfer from wind to wave enhances downstream of the crest and it is influenced by the separated flow. Further investigations are needed to understand the physical interaction between the separated flow and the downward momentum transfer.

4.7. Phase-averaged wave-induced Reynolds

The phase-averaged wave-induced Reynolds stress $<-\widetilde{\tilde{u}\tilde{v}}>$ is plotted in figure 4.8 versus height at wind speeds of 3.7 and 4.4 m s^{-1}. The plot shows that at both wind speeds the influence of wave-induced Reynolds stress is limited to a height less than or equal to three times the significant wave height. At both wind speeds and at all phases, the wave-induced Reynolds stress is mainly negative in the near-surface region, indicating that the wave-induced component of the airflow contributes to the upward momentum transfer along the entire waveform.

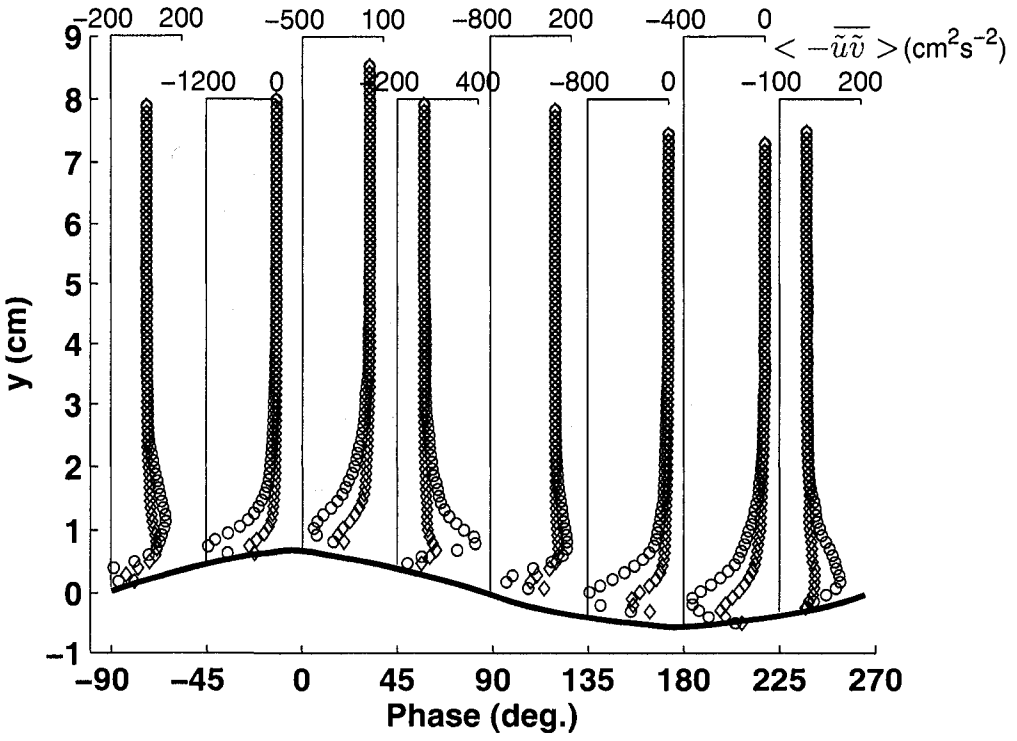

Figure 4.8: Vertical profiles of the phase-averaged wave-induced Reynolds stress as a function of phase, (Symbols: ○, =4.4 m s^{-1}; ◊, =3.7 m s^{-1}).

Hsu and Hsu (1983) computed the wave-induced Reynolds stress above mechanically-generated water waves in the presence of wind at wind speeds ranging from 1.37 to 2.92 m s^{-1}. At most of the wind speeds, they observed negative wave-induced Reynolds stress in the near-surface region whose magnitude decreased towards the surface and became positive in some cases. They argued that the wave-induced Reynolds stress is produced by the stretching and compression of the near surface flow field and therefore the maximum intensity is expected to occur above the wave crest. The present results show that the maximum wave-induced Reynolds stress occurs just upwind of the wave crest.

4.8. Phase-averaged turbulent Reynolds stress

Figure 4.9 shows the vertical profiles of the phase-averaged turbulent Reynolds stress $<-\overline{u'v'}>$ at wind speeds of 3.7 and 4.4 m s^{-1}. The plot shows different behaviour of turbulent Reynolds stress on the windward and leeward faces of the wave. On the leeward face, the profiles of the turbulent Reynolds stress show the classical behaviour i.e. the Reynolds stress magnitude is zero at the interface which increased sharply to a maximum value within a height approximately equal to half of the significant wave height and then decreased gradually to zero towards the free stream region. On the windward face, the Reynolds stress behaviour in the near-surface region is significantly different. That is, the turbulent Reynolds stress is negative in a thin layer immediately above the water surface whose thickness is about 2 mm. With an increase in height, the turbulent Reynolds stress becomes positive attains a certain magnitude which remains almost unchanged to a certain distance, and then gradually decreases to zero towards the free stream region.

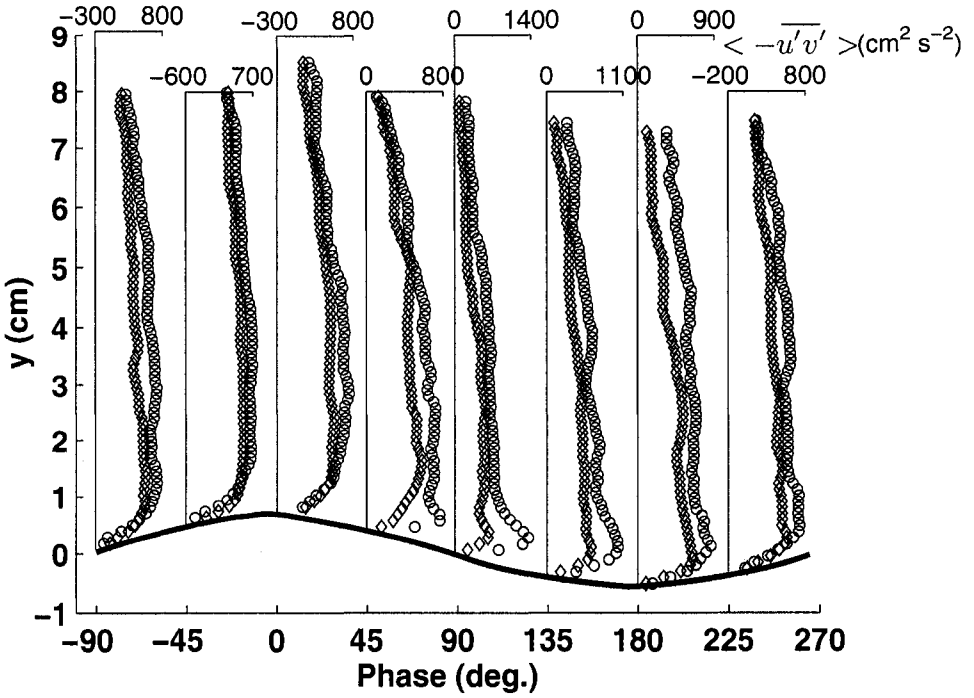

Figure 4.9: Vertical profiles of the phase-averaged turbulent Reynolds stress as a function of phase, (Symbols: ○, =4.4 m s^{-1}; ◊, =3.7 m s^{-1})

It is observed that on the windward side of the wave crest (-45° to 0°), the turbulent Reynolds stress maintains a constant maximum magnitude over a distance of about 3.8 cm that correspond to the distance from one significant wave height to three significant wave heights. Kato and Sano (1971) investigated the turbulent structure of airflow over coexisted mechanically-generated waves and wind waves using hot-wire anemometry. They reported that the time-averaged turbulent Reynolds stress increased with distance from the mean water surface to a certain height and then decreased towards the free stream region. They also stated that the turbulent Reynolds stress distribution over the wavy water surface is comparable to that measured within the boundary layer over a solid wall. However they did not present any comparison.

Shaikh and Siddiqui (2008) computed the fluctuating horizontal and vertical velocities u_f and v_f by subtracting the mean velocities from their respective instantaneous velocities. They compared the vertical profiles of total Reynolds stress $(-\overline{u_f v_f})$ averaged over all phases, in the presence and absence of the waves. They reported that in the absence of waves (1.5 to 3 m s^{-1} wind speeds), the Reynolds stress is positive both near and far from the interface and shows the classical behaviour, whereas, in the presence of surface waves (3.7 and 4.4 m s^{-1} wind speeds), the Reynolds stress close to the interface is negative and the magnitude of the negative Reynolds stress increased with wind speed. The Reynolds stress became positive with an increase in height and showed the classical behaviour.

The present study clearly shows that the total Reynolds stress has two components which are the turbulent and wave-induced Reynolds stresses. The decomposition of these two components in the present study enabled us to investigate the individual contributions of the turbulent and wave-induced components of the Reynolds stress to the momentum exchange between the air and water, particularly in the near surface region. The near surface turbulence enhances the turbulent Reynolds stress causing an increase in the downward momentum transfer whereas the fluctuating nature of water waves create an additional flow pattern in the near surface region which is responsible for the upward momentum transfer from waves to wind.

4.9. Distribution of tangential, wave-induced and turbulent stresses

The tangential stress (τ_v) is computed at each phase angle within the layer immediately above the water surface using the relation,

$$\tau_v = \mu\left(\frac{dU}{d\xi}\right)_{\xi} \tag{4.1}$$

where, μ is the dynamic viscosity of air and $\frac{dU}{d\xi}$ is the phase-averaged streamwise velocity gradient computed between the two heights at 0.5 mm and 1.5 mm from the interface. The distribution of the tangential stress, wave-induced stress and turbulent stress at a height of 0.5 mm above the water surface is plotted in figure 4.10 as a function of wave phase. The figure shows that the magnitude of tangential stress (τ_v) is positive over the entire waveform. However, its distribution is different on the windward and leeward faces. On the windward face (i.e. 180° to 0°), the magnitudes of tangential stress increased gradually with the phase, whereas on the leeward face, the tangential stress increased sharply from 0° to 30° and then decreased gradually to a minimum value at the trough (180°). The sharp increase in τ_v occurred in the flow separation region. The trends of the wave-induced and turbulent stresses in the near-surface region have already been discussed in figures 4.8 and 4.9. The comparison of the magnitudes of all three stress components immediately above the water surface shows that on the windward face of the wave crest (-90° to 0°), the wave and turbulent stresses are negative and significantly larger in magnitude compared to the tangential stress which is positive in the region. Comparison of wave and turbulent stresses shows that in this region, the magnitude of

wave stress is almost twice the magnitude of turbulent stress at both wind speeds and that the distribution of stresses is almost identical.

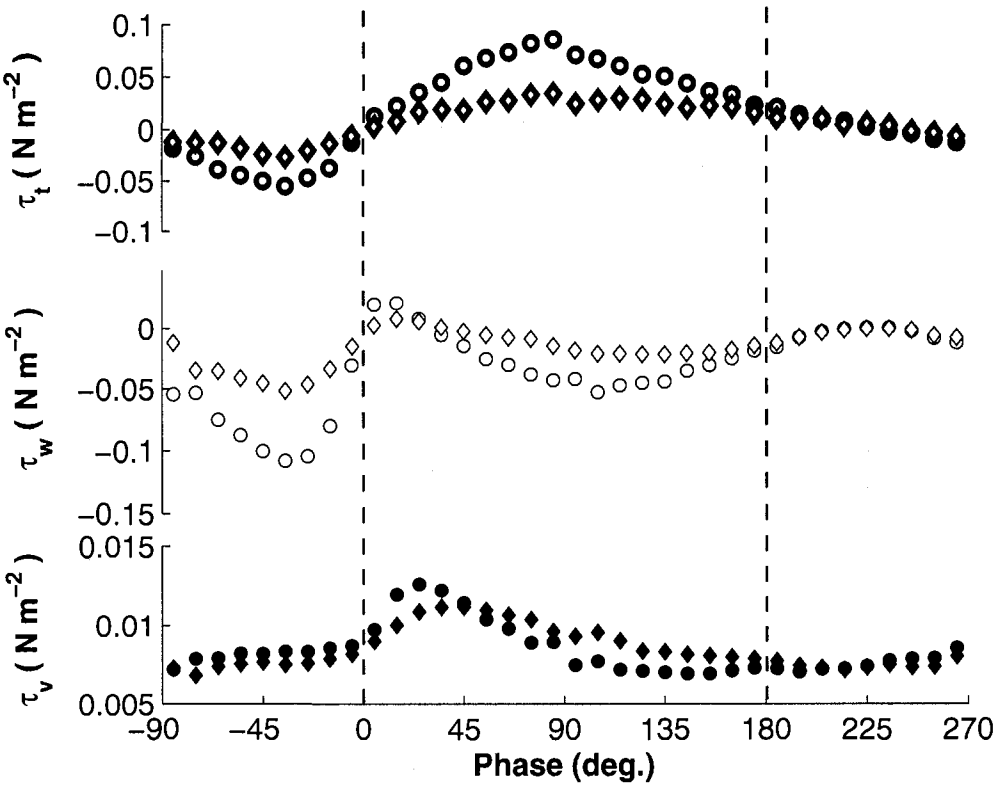

Figure 4.10: Tangential stress (τ_v) , wave-induced stress (τ_w) and turbulent stress (τ_t) at a height of 0.5 mm from the water surface versus the phase (Symbols: ○, =4.4 m s^{-1}; ◊, =3.7 m s^{-1})

The results indicate that the wave-induced stress is the dominant stress component on the windward face of the wave crest and thus, the overall effect is the upward momentum flux in this region. On the leeward face of the wave crest (i.e. 0° to 90°), the tangential and turbulent stresses are positive and wave-induced stress is negative. The

plot shows that on the leeward face of the wave crest, turbulent stress is dominant. The overall effect is the positive stress along the leeward face and thus, a downward momentum flux. In the trough region, the magnitudes of all three stress components are small which indicates that the trough region does not contribute significantly to the momentum exchange.

Figure 4.10 shows the distribution of stress components at a height of 0.5 mm from the surface. At this height, small magnitudes of the tangential stress over the entire waveform indicate that the tangential stress does not provide a major contribution to the total wind stress. However, as approaching towards the interface, the tangential stress is expected to increase significantly. The profiles in figure 4.9 show that the turbulent Reynolds stress approaches zero towards the interface. The wave-induced Reynolds stress (figure 4.8) also shows a decreasing trend as it approaches the interface. Thus, the contribution of the tangential stress would be significant at the surface and for the given experimental conditions, it is expected to be around 50% of the total wind stress (Banner and Peirson 1998).

Kudryavtsev and Makin (2001) investigated the impact of airflow separation on the drag of the sea surface and argued that at low wind speeds, the tangential stress dominates the surface drag while the role of the form drag is negligible. With an increase in the wind speed, the role of the form drag becomes pronounced. At wind speed $U_{10} > 10$ m s^{-1}, the surface drag is mainly supported by the wave form drag. This fact could be due to enhanced surface roughness which generates turbulence and reduces the relative speed of the airflow within few centimeters above the waves. Veron et al. (2007) presented the surface tangential stress (τ_s) of an instantaneous velocity field computed at a height of

0.15 mm from the fluctuating water surface. They observed large surface tangential stresses on the windward side of the wave with its maximum magnitude at the wave crest and argued that at wave crest the tangential stress is the dominant component of the total wind stress. As shown in figure 4.10, the magnitudes of wave-induced and turbulent Reynolds stresses at the wave crest are very small. A quantitative comparison showed that at the crest, the tangential stress is three times larger in magnitude than the wave-induced and turbulent stresses. Therefore, the present results somehow validate the observations of Veron et al. (2007). However, we observed peak tangential stress at a phase of 30° that is 40% larger than the tangential stress observed at the crest. Reul et al. (2008) evaluated the tangential stress, within a distance of 1.2 mm above the mechanically-generated water waves. They compared the tangential stress of two instantaneous PIV velocity fields, for separated and non-separated flows. They reported that the tangential stress over the non-separated flow grows progressively on the windward side from its minimum value at the trough to the maximum value at the crest. Whereas, over the separated flow, they observed that the tangential stress decreased significantly within the separation region and then increased progressively to its maximum value at the next crest. The phase-averaged tangential stress profiles plotted in figure 4.10 are qualitatively in agreement with that reported by Reul et al. (2008). However, we did not observe sudden decrease in the tangential stress profile downwind of the crest. It should be noted that Reul et al. (2008) and Veron et al. (2007) estimated the tangential stress from single instantaneous velocity field for the separated or non-separated condition, whereas, our results are based on the average of 4500 velocity fields at each wind speed that comprised of both separated and non-separated flow conditions.

4.10. Discussion

The phase-averaged properties presented in the preceding section provided a better insight into the airflow structure over the waveform of wind-generated waves. The phase-averaged wave-induced velocity field clearly shows significant magnitudes in the near surface region. At heights greater than three times the significant wave height from the water surface, the magnitude of wave-induced velocity is negligible. This indicates that in the outer region, the waves have no effect on the flow field. Typically, the vertical distance within which the waves influence the flow structure is termed as wave boundary layer (WBL). The present results indicate that at small fetch and low wind speeds, the WBL is limited to a height of approximately three times the significant wave height above the fluctuating water surface. However, to validate the thickness of WBL, more experimental evidences are necessary, especially at higher wind speeds and longer fetches. The results presented in figures 4.1and 4.3 also show that within the WBL, the magnitude and direction of wave-induced velocity is different at different phases. The wave-induced velocity over the crest is in the direction of the wave propagation whereas the wave-induced velocity over the trough is in the direction opposite to the wave propagation. At all heights, the largest positive magnitude of the wave-induced velocity is observed at the 0^{o} phase which is the wave crest whereas, the largest negative magnitude is observed at the 90^{o} phase which is the core of the separated flow region.

The phase-averaged vorticity (figure 4.5) shows that most intense vorticity occurs on the leeward face which is 1.5 to two times larger in magnitude than that on the windward face. The flow separation contributes to the enhancement of vorticity on the leeward side. The results also show that the thickness of the enhanced vorticity layer is

minimum above the crest and maximum above the trough. Reul et al. (2008) investigated the snap shots of the instantaneous velocity and vorticity fields and observed sudden augmentation in the vorticity layer immediately above the separated flow downwind of the breaking crest. They reported that the shear layer of clockwise vorticity departed from the crest and reattached to the interface downwind of the trough. They argued that the strength of the shear layer of clockwise and counterclockwise vorticity is controlled by the crest dynamics and wind forcing intensity. As described in the introduction section, most of the previous studies used point measurement techniques to measure airside velocity field. They typically installed measuring probes at heights ranging from 4 cm to 10 cm above the fluctuating water surface. At this height, the vorticity magnitude is expected to be very small. This could be the reason why previous airside studies did not observe enhanced vorticity layer in the measured velocity fields in the near surface region above the air-water interface. The studies using flow visualization techniques to investigate the flow structure in the near-surface region, however, indicated the presence of high vorticity layer. Kawamura and Toba (1988) and Komori et al. (1993) have qualitatively described the layer of high vorticity as an organized flow patterns immediately above the waves. Shaikh and Siddiqui (2008) compared the vorticity in the presence and absence of the waves and found a significant enhancement in vorticity in the near-surface region in the presence of waves.

Very few studies have reported the total Reynolds stress distribution over the water waves. Shaikh and Siddiqui (2008) have presented the spatially-averaged Reynolds stress profiles from the same dataset and found good agreement with that of Kawamura et al. (1981) who measured the velocity data using point measurement devices. Kato and Sano (1971) computed the total Reynolds stress from the streamwise and vertical

components of the fluctuating velocity and reported an increasing trend with decreasing height that have attained maximum values 5 cm and 8 cm above the wave crest at wind speeds of 6.3 m s^{-1} and 9.5 m s^{-1}, respectively. Below this height, the Reynolds stress decreased towards the water surface. This trend is also consistent with the present dataset. Anisimova et al. (1982) computed the Reynolds stress by integrating the momentum flux spectrum of streamwise and vertical velocity fluctuations, within the frequency range of the dominant waves. They observed negative Reynolds stress at their lowest measurement level that was located 2 cm above the wave crest. They found that the Reynolds stress became positive at greater heights and argued that in the early stages of the wave development, the momentum flux could be upward from water to air in the near-surface region, which is consistent with the present results.

As stated in the introduction section, upward momentum transfer from water to air has been reported in some laboratory (for example; Lai and Shemdin 1971, Kato and Sano 1971) and field studies (for example; Benilov et al. 1974, Antonia and Chambers 1980, Wetzel 1996). They reported that young short gravity waves extract momentum from the wind and the upward momentum transfer is only associated with developed waves. Their conclusion is mainly based on the spike observed around the dominant wave frequency in the co-spectra of the horizontal and vertical velocity fluctuations. The momentum transfer by young short waves is expected to be significantly smaller than the developed waves. Therefore, the spectral energy for young waves is expected to be significantly lower in magnitude than the developed waves in the co-spectrum. However, it does not imply that young waves do not contribute to the upward momentum transfer. The present results clearly show that the momentum exchange between the wind and waves is a two-way process and that young, short gravity waves also transfer momentum

to the air. Furthermore, the present velocity, vorticity and Reynolds stress profiles shows two distinct flow structures over the windward and leeward faces of the wave and also show that the upward momentum transfer occurs on the windward face and downward momentum transfer occurs on the leeward face.

As shown in the snap shot of the instantaneous velocity in figure 4.2a, the bursting, sweeping and airflow separation are intermittently observed immediately above the waves. A burst is defined as a streak of low speed fluid, that rises upward from the interface and eventually merges into the free stream flow (Willmarth and Lu 1972). During the breakup of a burst, significant chaotic motion occurs in the flow. Shaikh and Siddiqui (2008) have shown bursting and sweeping process above the wind waves. It was observed that the bursts originates from the windward side of the wave crest and merge into the free stream flow within a distance of three to four times the significant wave height from the mean water level. Other researchers such as, Komori et al. (1993) and Kawamura and Toba (1988) have also observed the bursting process on the windward side through flow visualization. As observed in figure 4.9, the height over which the magnitude of turbulent Reynolds stress remained large and constant on the windward side coincides with the bursting region and thus, this large magnitude is attributed to the bursts generated over the wind waves. The profiles in figure 4.9 also show that the largest magnitude of turbulent Reynolds stress over the entire waveform occurs in the near-surface region on the leeward face of the wave. This region corresponds to the separated flow region. As mentioned earlier, the flow separation was observed more frequently at the higher wind speed. Thus, the magnitude of the turbulent Reynolds stress in this region at the higher wind speed is significantly large compared to the lower wind speed. The results in figure 4.9 indicate that the most intense turbulence is generated on the leeward

side of the wave within a distance of one significant wave height from the water surface. As mentioned above, on the windward face, negative turbulent Reynolds stress is observed in a very thin layer adjacent to the water surface which is changed to positive stress as the distance increases. This indicates that within the thin layer on the windward side, the mean flow extracts energy from the turbulence.

Mete et al. (2002) reported significantly large magnitudes of wind stress over wavy water surface than that over the smooth water surface. They argued that the enhanced wind stress is a consequence of surface waves on the wind field close to the interface. They anticipated that the increase of wind stress is due to the wave-induced stress. Lai and Shemdin (1971) reported strong turbulence over the wavy water surface and concluded that the enhanced wind stress over the waves is due to the enhanced near surface turbulence and the wave-induced stress. The present study provides the quantitative assessment of the contributions of different components of the stress as a function of wave phase. The results show that in the near-surface region over the entire waveform, the magnitude of wave-induced Reynolds stress is on average a factor of 4 and 2 higher than the tangential stress at wind speeds of 4.4 and 3.7 m s^{-1}, respectively. Whereas, the magnitude of turbulent Reynolds stress is on average a factor of 2 and 0.9 of the tangential stress at wind speeds of 4.4 and 3.7 m s^{-1}, respectively. Therefore, it can be argued that the wave-induced Reynolds stress is the main contributor to the total wind stress in the near-surface region. However, its magnitude decreases towards the surface where the contribution of tangential stress also becomes significant.

CHAPTER 5

Flow characteristics over separated and non-separated flow fields

5.1. Introduction

When air flows over steep water waves, it detaches from the interface on the leeward side of the crest and reattaches on the windward side of the following crest. Researchers have used flow visualization techniques and qualitatively described flow separation as a vortex trapped within the crest-trough region immediately above the water surface. Flow visualization only provides qualitative observations of the instantaneous behaviour of the flow separation. Kawai (1982) examined the dependability of the separated and non-separated airflow structures on the steepness of the wave. He computed the maximum wave surface gradient for a sample of 79 wave profiles, using the photographs of the airflow field over water waves. He suggested that the flow separation occurs over the wave crest if the maximum wave slope, $S_{max} > 0.6$. Reul et al. (2008) also reported that the flow separation systematically occurs downwind of the wave. They argued that the flow separation requires a maximum local wave slope of 35^{o} which is also in agreement with the critical slope for the airflow separation of 0.6 reported by Kawai (1982). Reul et al. (2008) and Kawai (1982) reported the relation between the wave steepness and the air-flow separation. However, to date, the quantitative contribution of the airflow separation to the near surface turbulence is not reported in the literature. The short coming is attributed to the measurement difficulties within the crest-trough region as well as the techniques employed in the analysis.

This chapter focuses on the quantitative comparison of the flow characteristics over separated and non-separated velocity fields over wind-generated water waves. We have developed a scheme to automatically detect separated and non-separated velocity fields within the dataset. This scheme was applied to the datasets at 3.7 and 4.4 m s^{-1} wind speeds as the waves were observed only at these two wind speeds.

5.2. Separation Scheme

As mentioned in chapter 2, at each wind speed, 4500 velocity fields were obtained. A threshold-based algorithm was developed to segregate the velocity fields with flow separation downwind of the steep water waves. As mentioned earlier, the flow separation occurs over the steep water waves. The steepness of the waves is based on the wave slope along the leeward face of the wave. In the present technique, all the wave-profiles in which the phase between 0^{o} and 180^{o} i.e. the crest-to-trough region (leeward face) was visible were segregated from the rest of the wave profiles at a given wind speed. As shown in Table 5.1, at wind speeds of 3.7 and 4.4 m s^{-1} the crest-to-trough region was identified in 47% and 52% of the total wave profiles, respectively. For each of the segregated wave profile, the local wave slopes were computed as the gradient of the wave surface displacement ($d\eta/dx$) over a horizontal distance of 0.3 mm (5 pixels) at equally spaced points along the leeward face (from the crest to the trough). The maximum wave slope (S_{max}) was then computed based on the local wave slopes for each wave. The wave slope of 0.6 was selected as the threshold, which is based on the observations of the previous studies (Reul et al. 2007, Kawai 1982). All the waves with $S_{max} \geq 0.6$ were

considered as the waves over which the flow separation occurred and the corresponding velocity fields were assigned as the separated velocity fields. The total number of separated velocity fields identified by the algorithm is presented in Table 5.1 at both wind speeds. The values indicate that at wind speeds of 3.7 and 4.4 m s^{-1}, the flow separation occurs in 18% and 47% of the wave profiles having crest-to trough region (0^o to 180^o phase) visible in the image, respectively.

TABLE 5.1. Summary of number of wave profiles (N_t total number of velocity fields, N number of wave profiles contain crest-to-trough region, $N_{0.6}$ number of separated velocity fields having wave slope greater than or equal to 0.6, $N_{0.4-0.6}$ total number of velocity fields having wave slope greater than 0.4 and less than 0.6, $N_{0.4}$ number of velocity fields having wave slope less than or equal to 0.4, $n_{0.4-0.6}$ number of separated velocity fields having wave slope greater than 0.4 and less than 0.6, excluded from the calculation.

U_∞ (m s^{-1})	3.7	4.4
N_t	4500	4500
N	2123	2344
$N_{0.6}$	382	1103
$N_{0.4-0.6}$	438	634
$N_{0.4}$	1303	607
$n_{0.4-0.6}$	132	390

The separated flow detection scheme was validated based on the visual inspection of the instantaneous velocity fields at the wind speeds of 3.7 and 4.4 m s^{-1}. In visual inspection, 4500 velocity fields were visually inspected at each of the two wind speeds. When flow separation was observed in any velocity field, the corresponding frame number and the maximum of the local wave slope downwind of the crest were recorded. The visual inspection shows that flow separation starts at $S_{max} \approx 0.4$ and the percentage of wave with separated flow increased with an increase in the wave slope. The results also shows 98 % of the waves with $S_{max} \geq 0.6$ caused the flow separation. Therefore, the visual inspection somehow validates the scheme used to identify the separated velocity fields. The inspection of the velocity fields also indicated that at both wind speed, the instantaneous velocity within the separation zone is as small as 10% of the free stream velocity. It was also observed that the separation region contains counter-clockwise vortices that were bounded from the top and bottom by the layers of clockwise vortices. However, the size, shape and magnitude of counter-clockwise vortices varied from field to field. This variation could be related to the variation of the profile of individual wave crests.

As stated above, some of the velocity fields having S_{max} greater than or equal to 0.4 and less than 0.6 contain flow separation, that was identified in a smaller region compared to the flow separation observed in the velocity fields having $S_{max} > 0.6$. The flow separation over the waves having S_{max} greater than or equal to 0.4 and less than 0.6 could be the residues of the flow separation associated with previous velocity fields. These fields could neither be considered as the active flow separation region nor they be

classified as non-separation regions. Therefore, in order to make a true comparison between the separated and non separated velocity fields it was necessary to identify and exclude these velocity fields from further analysis. A scheme was developed, to segregate these velocity fields. In this scheme, as a first step, the frame numbers of the velocity fields were binned according to the maximum wave slope computed within the crest to trough region (S_{max}). As shown in Table 5.1, at wind speeds of 3.7 and 4.4 m s^{-1}, the velocity fields with $0.4 \leq S_{max} < 0.6$ were identified in 20% and 27% of the of the wave profiles, whereas, the wave profiles with $S_{max} < 0.4$ were identified in 60% and 25% of the of the wave profiles having crest-to trough region visible in the image, respectively. As stated above, the flow separation contains counter clockwise vortices (negative vorticity) therefore, to identify the separated flow within the velocity fields with $0.4 \leq S_{max} < 0.6$, the presence of negative vorticity was considered as the criterion. That is, the negative vorticity was searched at each grid point from crest to the trough within a layer equal to the significant wave height from the surface. When the negative vorticity was observed at any of the grid point, the streamwise component of the instantaneous velocity at that point and at four neighbouring points was examined. If the streamwise velocity was found to be less than or equal to the 10% of the free stream velocity at five or less grid points (depending on the location of the given point with reference to the water surface), then that velocity field was recorded. The total number of separated velocity fields with $0.4 \leq S_{max} < 0.6$ is presented in Table 5.1. The values indicate that at wind speeds of 3.7 and 4.4 m s^{-1}, these velocity fields correspond to 6% and 15% of the wave profiles having crest-to trough region visible in the image, respectively.

5.3. Results

To obtain a better insight into the flow dynamics, different flow characteristics are analyzed as a function of wave phase. The procedure to compute flow properties as a function of phase are already described in Chapter 4. The results are plotted at eight different phases 45° apart that covers the entire waveform. The profiles of phase-averaged surface displacement for the separated and non-separated fields are presented in figure 5.1a and 5.1b, at wind speeds of 4.4 and 3.7 m s^{-1}, respectively. The plots show that at both wind speeds, the phase-averaged profiles of surface displacement for the separated and non-separated fields are not exactly sinusoidal. However, the profiles of the non-separated waves are more close to the sinusoidal behaviour than the profiles of separated waves. This indicates that the nonlinear behaviour of the waves also contributes to the flow separation. For both type of flows and at both wind speeds, the vertical distance from mean position to the crest is greater than the vertical distance from mean position to the trough. The plots also show that for both wind speeds, the height of the waves with flow separation is greater than the height of the waves with no flow separation. Quantitatively, at wind speeds of 4.4 and 3.7 m s^{-1}, the height of the waves with flow separation is 40% and 15% higher than that for the non-separated flow respectively. This shows that the flow separation occurs over the waves with larger amplitude and slope. Kawai (1982) compared the maximum wave heights of the 79 samples of the instantaneous photographs of separated and non-separated flows and reported that the flow separation occurs over the higher and steeper waves. However he didn't suggest any

quantitative value of the maximum wave height and argued that the wave height is not the sufficient condition for the flow separation.

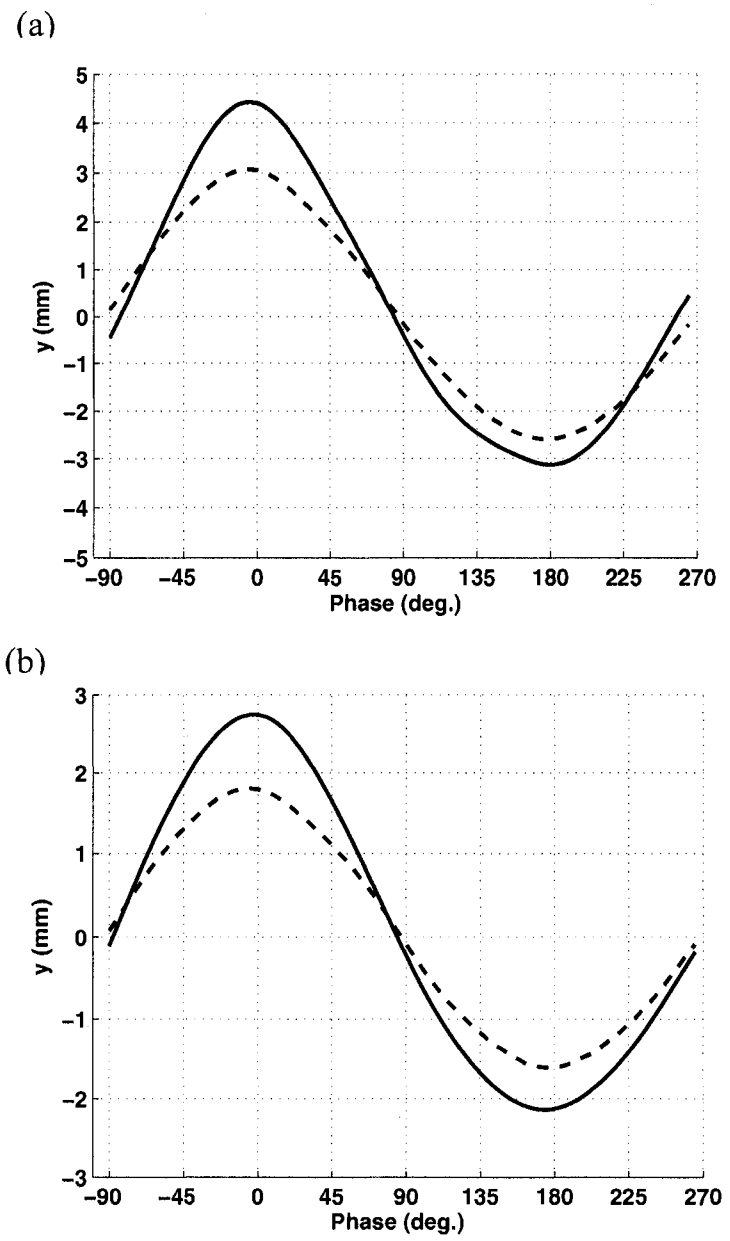

Figure 5.1: Phase-averaged wave amplitude for the separated and non-separated velocity fields, at wind speeds of, (a) 4.4 m s^{-1}, (b) 3.7 m s^{-1}. (Symbols: solid, =separated; dash, =non-separated)

Figure 5.2a and 5.2b compare the normalized phase-averaged streamwise velocities for the separated and non-separated fields, as a function of height and wave phase at wind speeds of 4.4 and 3.7 m s^{-1}, respectively. Both plots show that the flow separation influences the mean streamwise velocity only along the leeward side of the crest. At the windward side of the crest, the magnitudes of mean streamwise velocities are approximately the same for separated and non-separated types of flows. The figures also show that along the leeward face, the magnitude of streamwise velocity is significantly lower for the separated flow than that for the non-separated flow. The difference between the magnitudes of streamwise velocities for separated and non-separated flows increased from 0^{o} to 135^{o} and decreased from 135^{o} to 270^{o}. This is due to the reason that when the flow gets separated off the wave crest, clockwise separation vortex is generated on the leeward side. This causes a flow reversal which results in a lower mean streamwise velocity. Comparison of figures 5.2a and 5.2b shows that the decrease in the magnitude of mean streamwise velocity for the separated flow is large at the higher wind speed. This is due to the generation of stronger separation vortex at the higher wind speed. It was also observed that at both wind speeds, the maximum deviation in the streamwise velocity occurred at the phase of 135^{o}, where the maximum reduction of the streamwise velocity is 72% and 65% at 4.4 and 3.7 m s^{-1}, respectively. This indicates that the core of the separated region is at a phase of 135^{o}. The figures also show that the thickness of the fluid layer influenced by the flow separation increased with the phase angle which reached a thickness equal to two times the significant wave height in the trough.

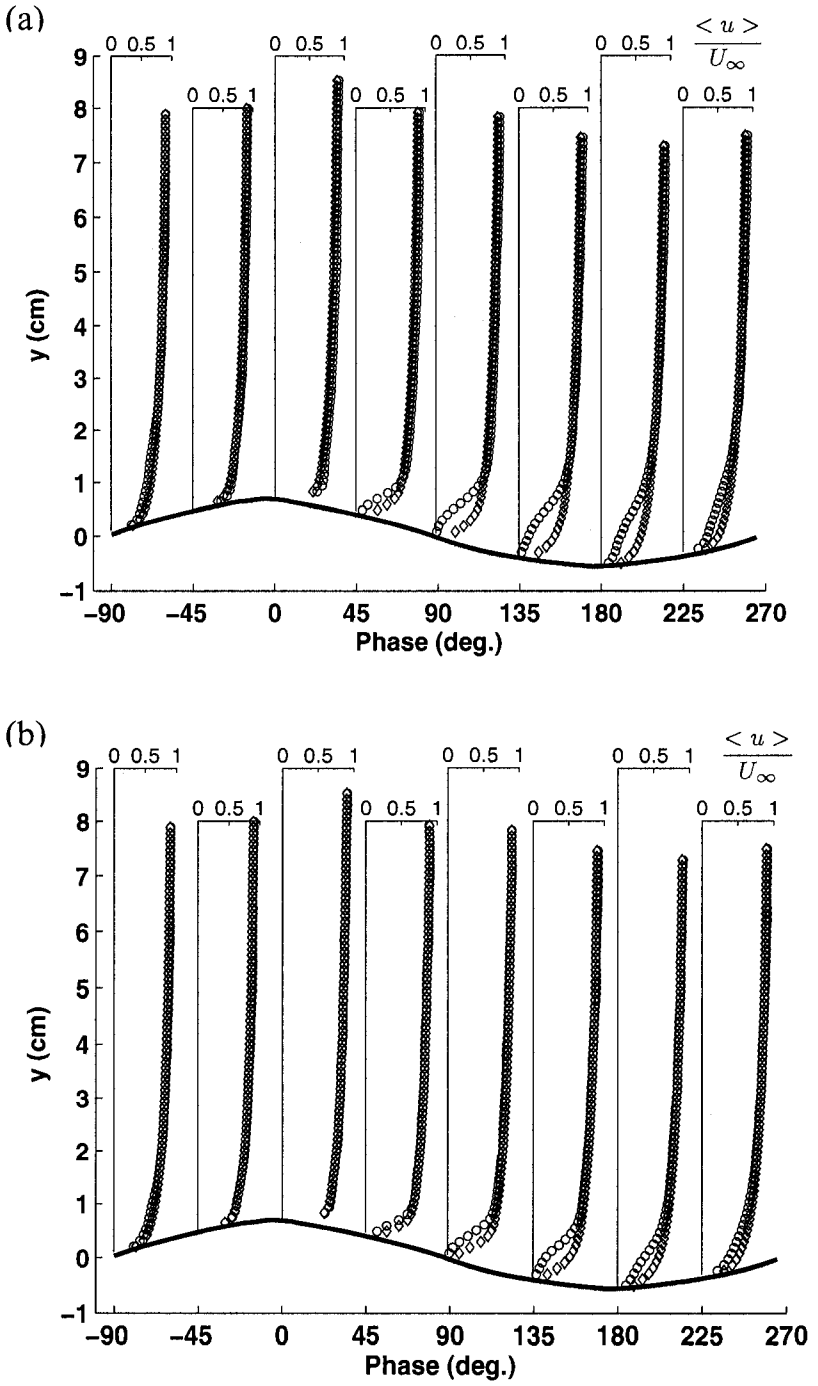

Figure 5.2: Vertical profiles of the normalized phase-averaged velocity as a function of phase at wind speeds of (a) =4.4 m s^{-1}, (b) =3.7 m s^{-1} (Symbols: ○, =separated; ◊, =non-separated)

The vertical profiles of the phase-averaged vorticity for the separated and non-separated flows are shown plotted in figure 5.3a and 5.3b at wind speeds of 4.4 and 3.7 m s^{-1}, respectively. The results show that similar to the phase-averaged streamwise velocity, the influence of flow separation on the average vorticity is mainly restricted to the leeward side of the wave. The vorticity profiles in the non-separation zone shows that the vorticity magnitude increased towards the water surface which is due to the increase in the mean velocity gradients towards the water surface. However, in the separation zone, the peak vorticity magnitude is observed at a height close to the significant wave height, which then decreased towards the surface. This indicates that the core of the separation vortex lies at a distance approximately equal to the significant wave height from the surface. Comparison of separated and non-separated flows also shows that for the non-separated flow, the thickness of the enhanced vorticity layer immediately above the water surface remains almost the same along the entire waveform, except at the crest where it is decreased. Whereas, for the separated flow, the thickness of the enhanced vorticity layer is increased in the separation zone.

The vertical profiles of the normalized phase-averaged wave-induced streamwise velocity for separated and non-separated flows are plotted in figure 5.4a and 5.4b, at wind speeds of 4.4 and 3.7 m s^{-1}, respectively. The plots show that unlike the phase-averaged velocity, the flow separation significantly influenced the wave-induced component of the streamwise velocity over the entire waveform. The results in Chapter 4 show that the wave-induced velocity for the fields (i.e. combined separated and non-separated fields) is positive in the crest region and negative in the trough region.

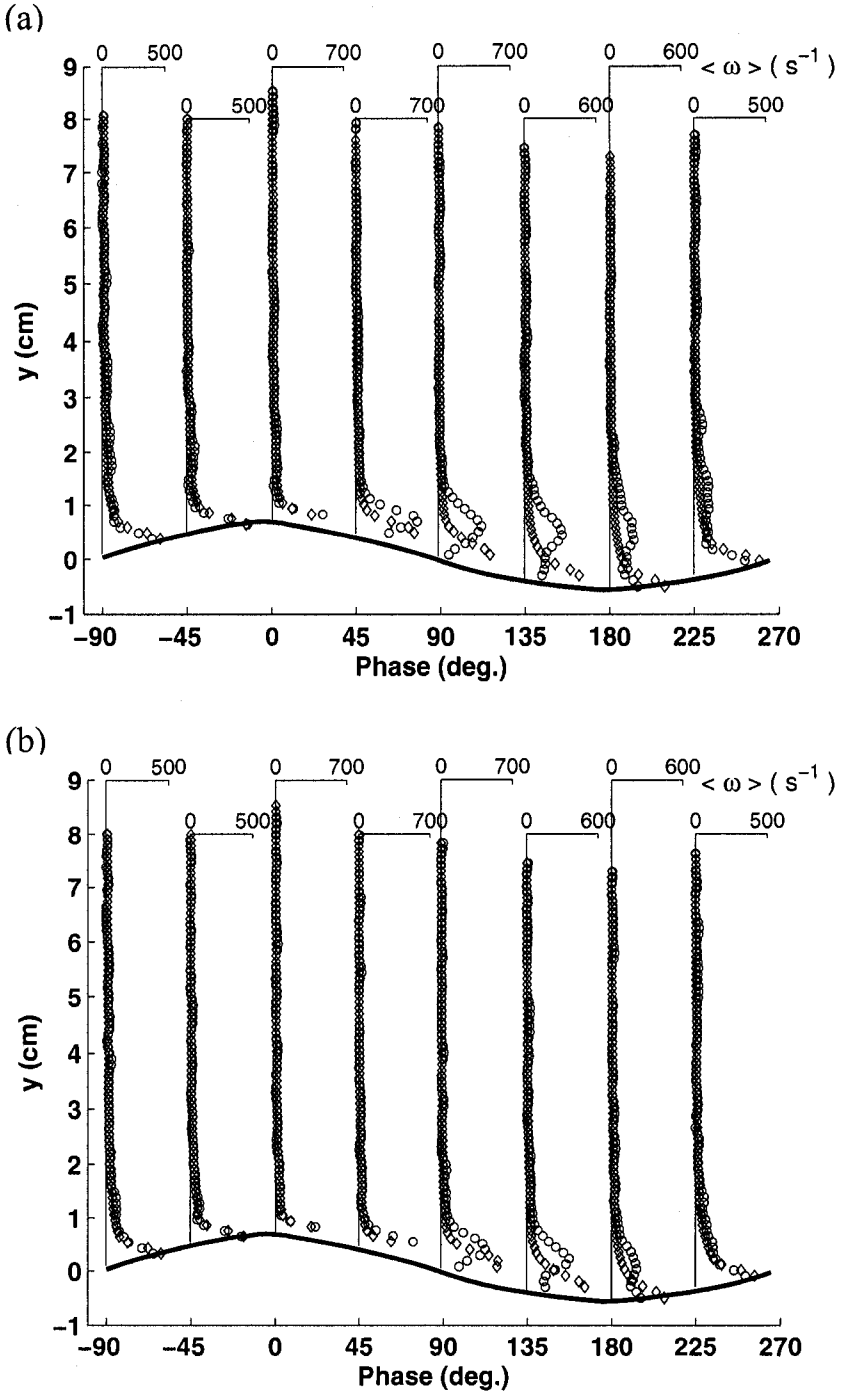

Figure 5.3: Vertical profiles of the phase-averaged vorticity as a function of phase at wind speeds of (a) =4.4 m s^{-1}, (b) =3.7 m s^{-1} (Symbols: ○, =separated; ◊, =non-separated)

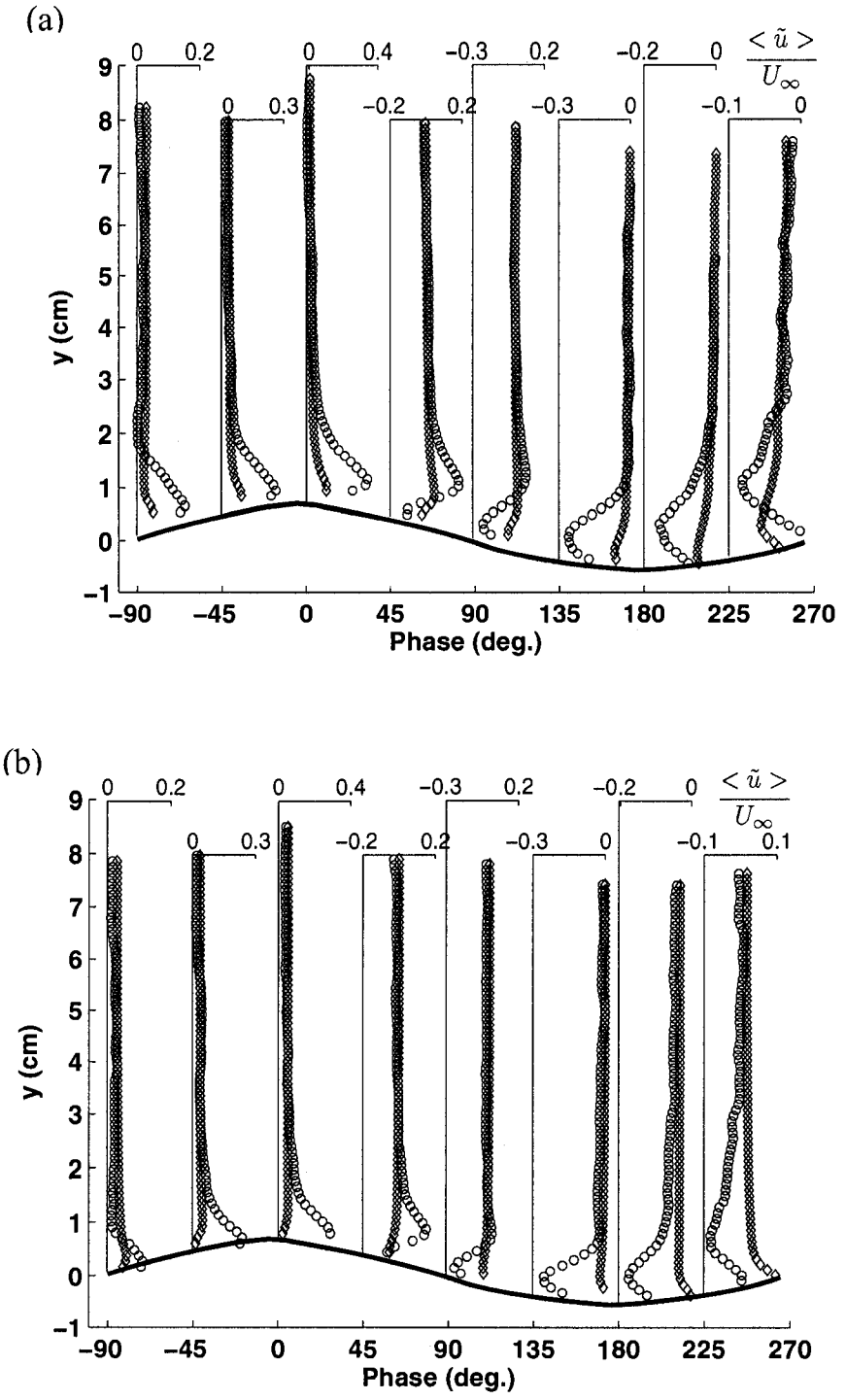

Figure 5.4: Vertical profiles of the normalized phase-averaged wave-induced velocity as a function of phase at wind speeds of (a) =4.4 m s^{-1}, (b) =3.7 m s^{-1} (Symbols: ○, =separated; ◊, =non-separated)

The results in figure 5.4 show that the separated and non-separated flows also show the similar trend, however, the magnitude of the wave-induced velocity significantly enhanced for the separated flows at both wind speeds. The enhancement was found to be of the same order of magnitude over the entire waveform, with the largest enhancement above the wave crest. On average over the waveform, the wave-induced component was enhanced by factor of 5.2 and 4.8 at 4.4 and 3.7 m s^{-1} wind speeds, respectively. The results also show that the thickness of the layer influenced by the wave-induced velocity is also increased for the separated flow. The thickness of this layer increased on the downwind side with the maximum thickness of three times the significant wave height at the phase of 225°.

The vertical profiles of the phase-averaged wave-induced vorticity for the separated and non-separated flows are presented in figures 5.5a and 5.5b, at wind speeds of 4.4 and 3.7 m s^{-1}, respectively. The plots show that for separated flow, the magnitude of the wave-induced vorticity increased with height in the region immediately adjacent to the water surface, reached a maximum value and then decreased towards zero magnitude at greater heights. Whereas, for non-separated flow, the magnitude of the wave-induced vorticity is significantly lower than that for the separated flow although the trends are similar. The plots also show that the location of the peak vorticity is higher for the separated flow compared to the non-separated flow. The peak magnitude of the near surface vorticity is observed at the phase of 0°, which is a factor of approximately 30 and 10 larger for the separated flow compared to the non-separated flow, at wind speeds of

4.4 and 3.7 m s^{-1}, respectively. Whereas, in the core of the separation region, the peak vorticity is observed at a phase of 90°, which is a factor of approximately 20 and 10 larger for the separated flow compared to the non-separated flow, at wind speeds of 4.4 and 3.7 m s^{-1} respectively. It is also observed that the thickness of the wave-induced vorticity layer is approximately 1.5 times the significant wave height when the flow is separated which is significantly larger than that for the non-separated flow.

The vertical profiles of phase-averaged wave-induced Reynolds stress $<-\widetilde{\widetilde{u}\widetilde{v}}>$ for the separated and non-separated flows are plotted in figures 5.6a and 5.6b, at wind speeds of 4.4 and 3.7 m s^{-1}, respectively. The plots show that for both types of flow, at all phases, the wave-induced Reynolds stress is mainly negative in the near surface region, which become negligible at heights greater or equal to three times the significant wave height. As discussed earlier in Chapter 4, this negative Reynolds stress indicates the upward momentum transfer from waves to wind. The comparison of $<-\widetilde{\widetilde{u}\widetilde{v}}>$ for separated and non-separated flows shows that at all phases, the magnitude of wave-induced Reynolds stress for the separated flow is significantly larger and extended to greater heights than that for the non-separated flow. For separated flow, the maximum wave-induced Reynolds stress is observed on the windward side (-45° phase angle) which is a factor of 10 and 4 higher than that for the non-separated flow at wind speeds of 4.4 and 3.7 m s^{-1}, respectively. Whereas, within the core of the separation region (at the phase of 90°), the maximum wave-induced Reynolds stress for the separated flow is a factor of 17 and 3 higher than that for the non-separated flow at wind speeds of 4.4 and 3.7 m s^{-1}, respectively.

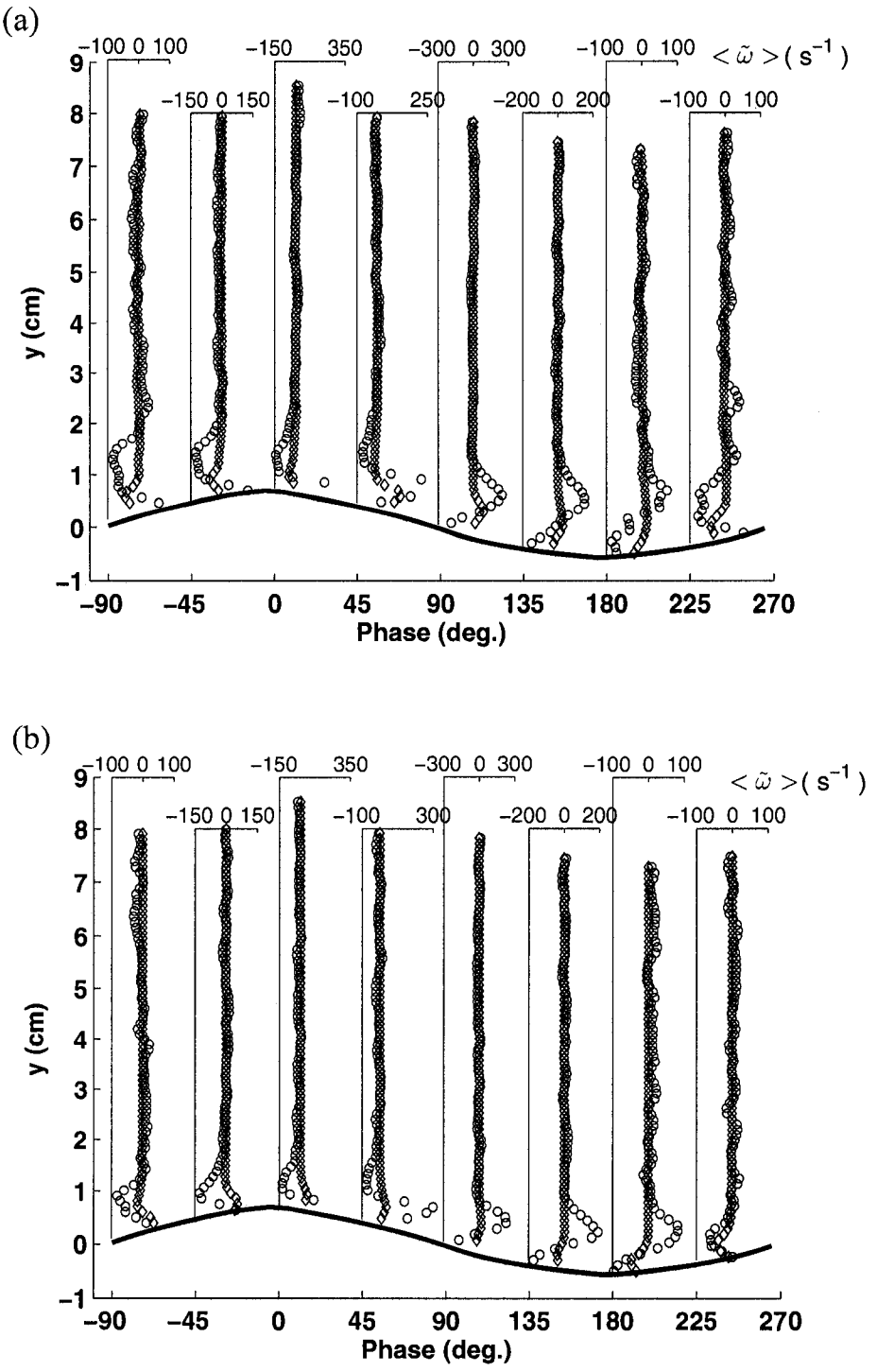

Figure 5.5: Vertical profiles of the normalized phase-averaged wave-induced vorticity as a function of phase at wind speeds of (a) =4.4 m s^{-1}, (b) =3.7 m s^{-1} (Symbols: ○, =separated; ◊, =non-separated)

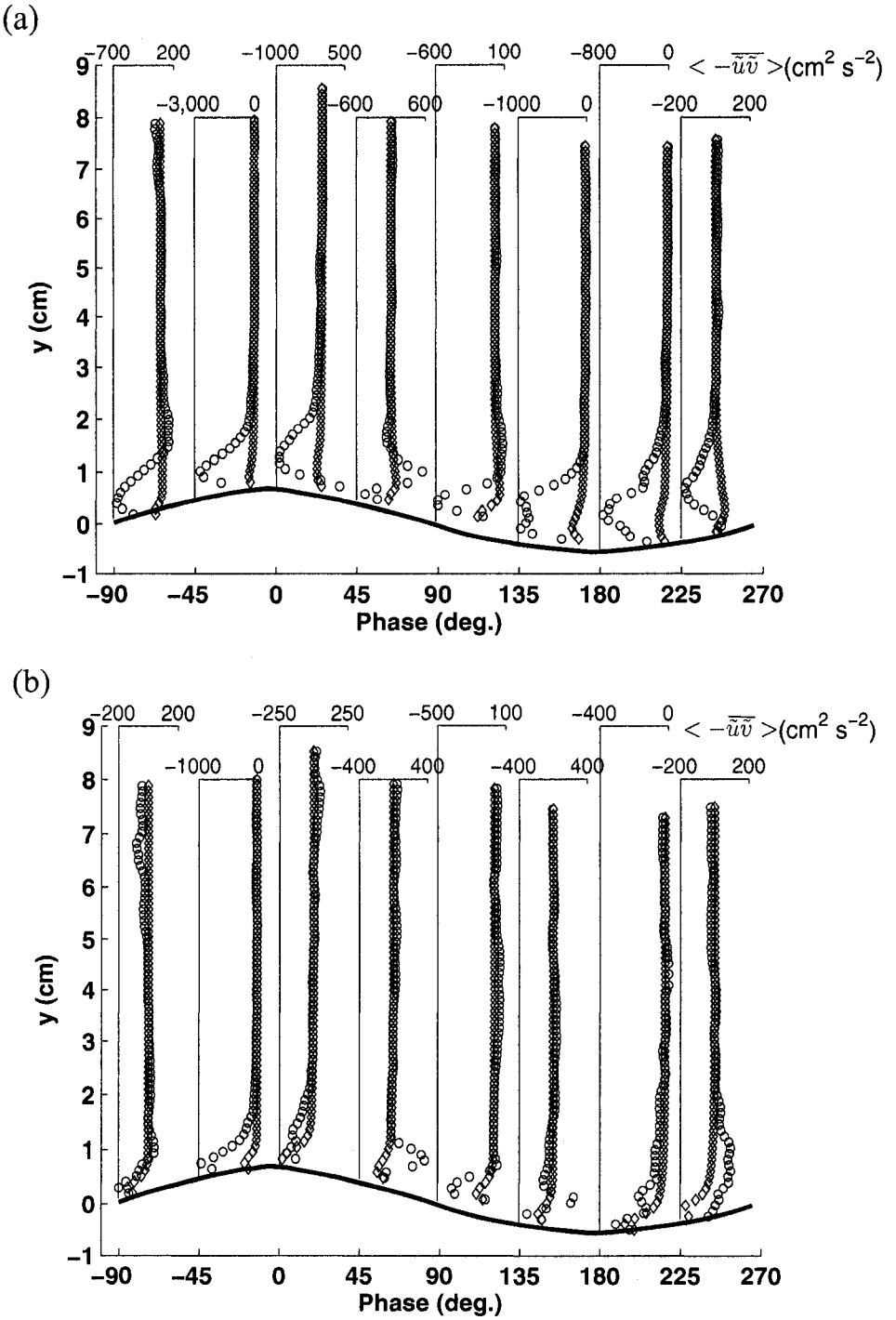

Figure 5.6: Vertical profiles of the normalized phase-averaged wave-induced Reynolds stress as a function of phase at wind speeds of (a) =4.4 m s^{-1}, (b) =3.7 m s^{-1} (Symbols: ○, =separated; ◊, =non-separated)

Figure 5.7a and 5.7b show the phase-averaged turbulent Reynolds stress $<-\overline{u'v'}>$ for the separated and non-separated flows, at wind speeds of 4.4 and 3.7 m s^{-1}, respectively. Both plots show that over the entire waveform, the turbulent Reynolds stress is following the same trend for the separated and non-separated types of flow. That is the turbulent Reynolds stress has minimum magnitude at the closest point from the interface, increased with height to a certain distance and then decreased towards the free stream region. The plots also show that on the windward face of the wave, the magnitudes of the turbulent Reynolds stress for the separated and non-separated flows are approximately the same in both the near surface region and above in the free stream region. Whereas, on the leeward face of the wave, the magnitude of turbulent Reynolds stress in the near-surface region is significantly larger for the separated flow than that for the non-separated flow. For the separated flow, the turbulent Reynolds stress increased sharply to a maximum value within a height approximately equal to half of the significant wave height and then decreased towards the free stream region. Both plots also show that at a height of two times the significant wave height from the mean water surface, the magnitudes of the turbulent Reynolds stress for the separated and non-separated flows are approximately the same, indicating that the effect of flow separation to the near surface turbulence is limited to distance within two significant wave heights. The figures also show that at both wind speeds, the maximum turbulent Reynolds stress is observed at a phase of 135° and at a height of approximately 1 cm from the mean water surface, that is a factor of 4.5 and 2.5 higher for the separated flow than that for the non-separated flow.

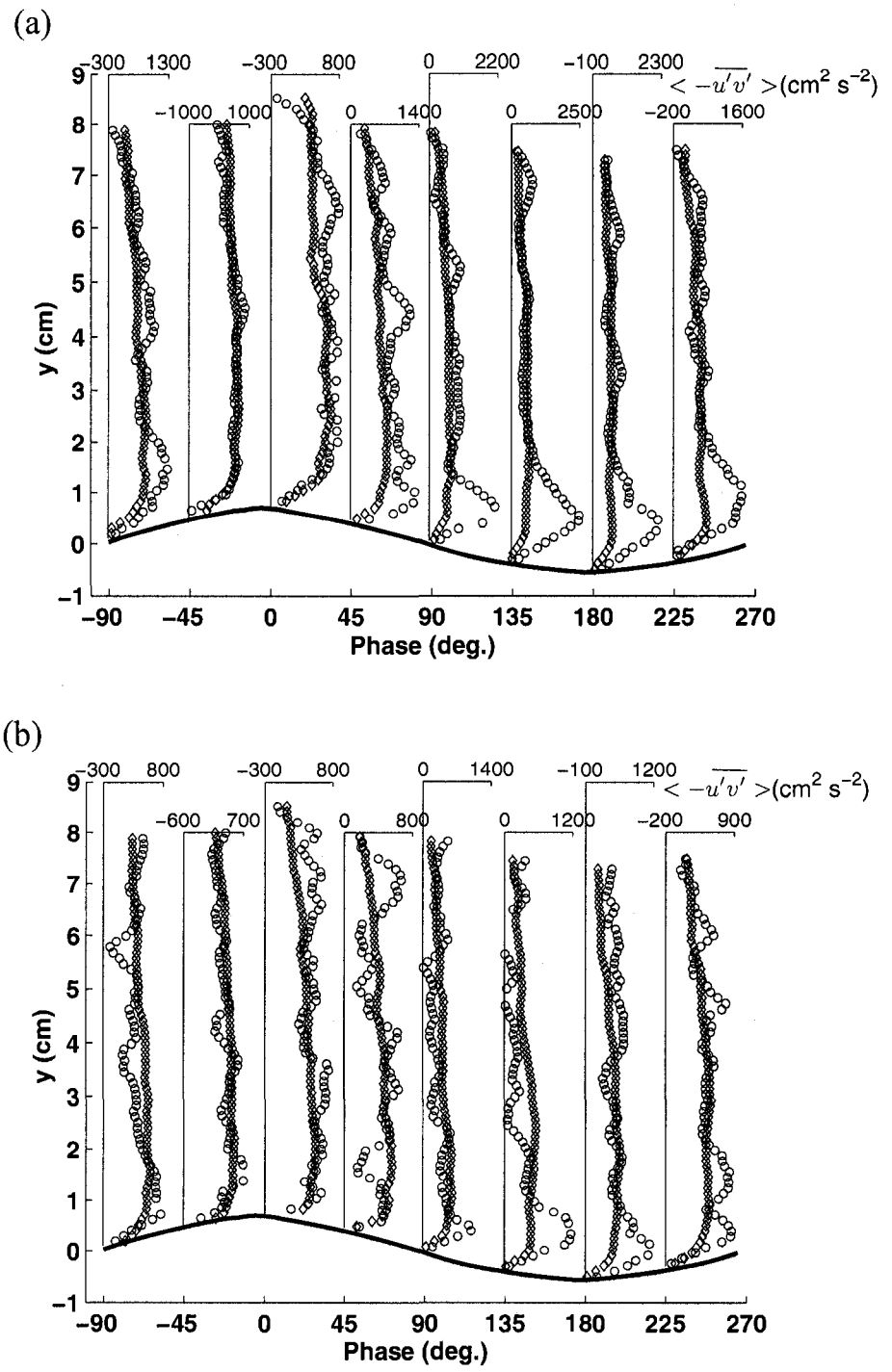

Figure 5.7: Vertical profiles of the normalized phase-averaged turbulent Reynolds stress as a function of phase at wind speeds of (a) =4.4 m s^{-1}, (b) =3.7 m s^{-1} (Symbols: ○, =separated; ◊, =non-separated)

The vertical profiles of the rate of turbulent kinetic energy production for separated and non-separated flows are plotted in figure 5.8a and 5.8b at 4.4 and 3.7 m s^{-1} wind speeds, respectively. The plots show that the rate of energy production is significantly higher for the separated flow on the leeward side and in the wave trough. The most significant increase in the energy production is observed at phases of 90^{o} and 135^{o}, where the peak energy production was enhanced by a factor of 15 and 5 at 4.4 and 3.7 m s^{-1} wind speeds, respectively. Another interesting observation is that on the leeward side, the location of the peak energy production is moved to a greater height for the separated flow which is approximately equal to the significant wave height. This shows that the flow separation enhances turbulence and also increases the thickness of the enhanced turbulence layer. The results also show that on the windward side near the wave crest, the turbulence production is not significantly influenced by the flow separation.

The vertical profiles of the rate of turbulent kinetic energy dissipation (ε) for separated and non-separated flows are plotted in figure 5.9a and 5.9b at 4.4 and 3.7 m s^{-1} wind speeds, respectively. The energy dissipation profiles show the classical behaviour for the non-separated flow over the entire waveform and for the separated flow on the windward side. That is, the dissipation rate increased with the decrease in the distance from the water surface, with the largest dissipation rate closest to the water surface. However, the dissipation profiles for the separated flow on the leeward side show peak dissipation at a distance of approximately one significant wave height from the surface. That is, the maximum dissipation occurs in the core of the separation zone, although the magnitude of peak dissipation remains almost the same for separated and non-separated flows. Comparison of the dissipation magnitude for separated and non-separated flows

shows that the separated flows influence the energy dissipation rate only on the leeward side, where the thickness of the enhanced dissipation layer is significantly increased.

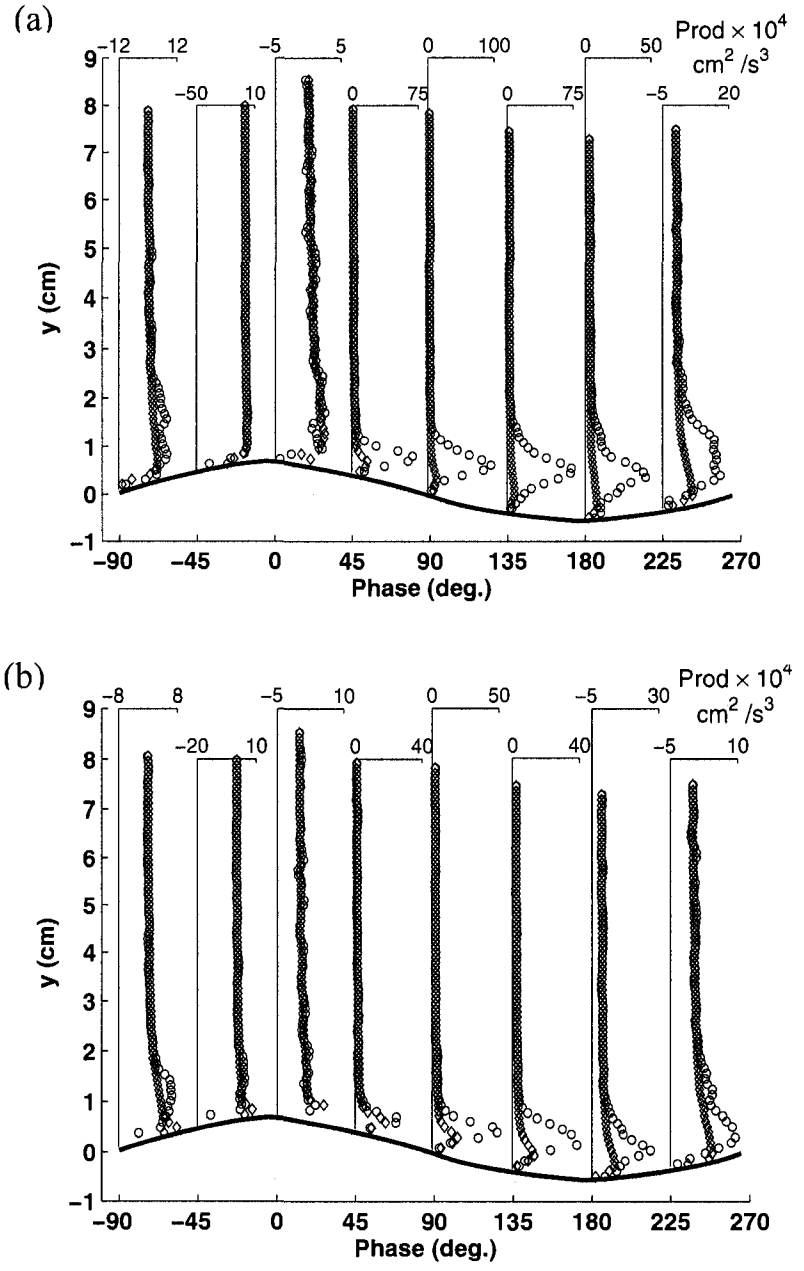

Figure 5.8: Vertical profiles of the normalized phase-averaged turbulent kinetic energy production as a function of phase at wind speeds of (a) =4.4 m s^{-1}, (b) =3.7 m s^{-1} (Symbols: ○, =separated; ◊, =non-separated)

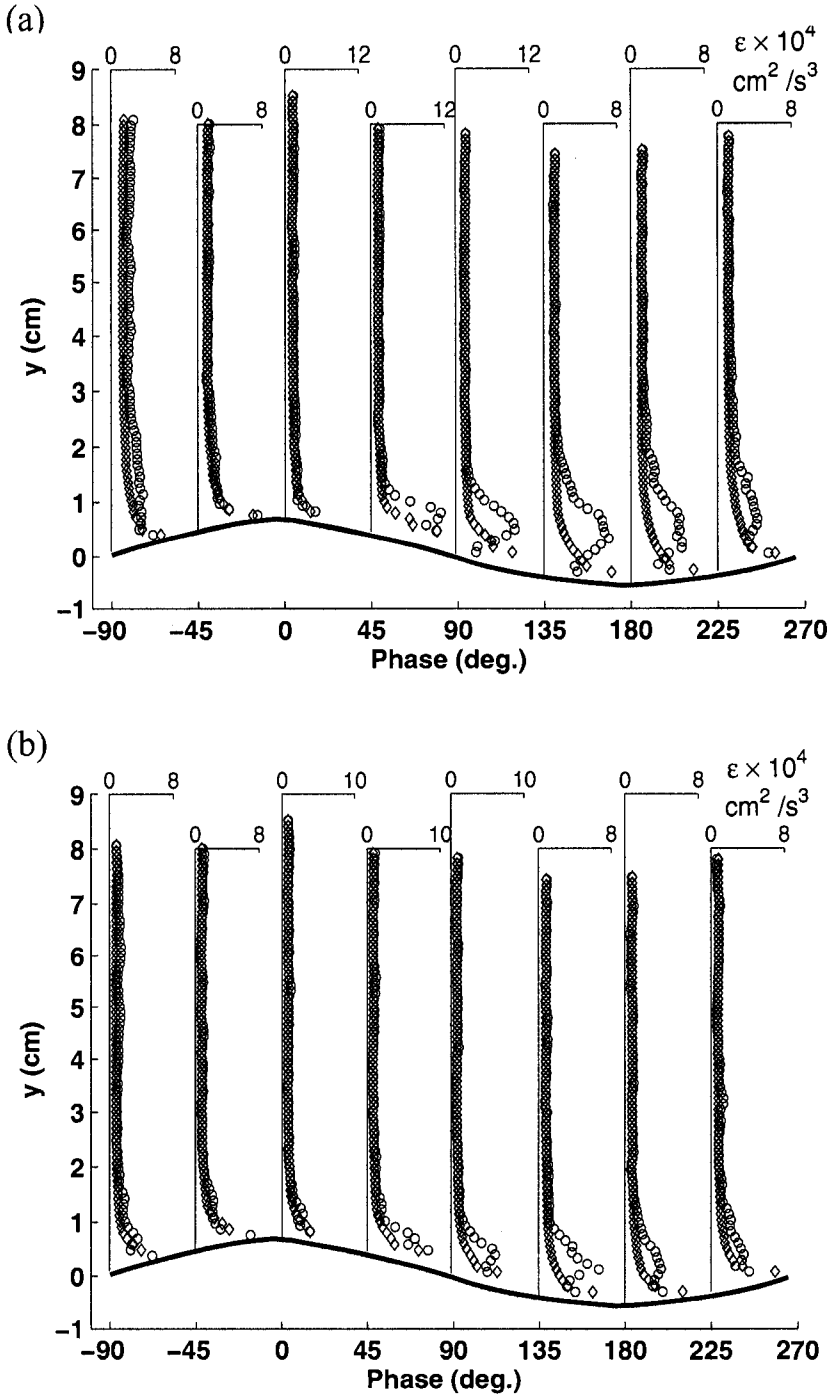

Figure 5.9: Vertical profiles of the normalized phase-averaged turbulent kinetic energy dissipation as a function of phase at wind speeds of (a) =4.4 m s^{-1},(b) =3.7 m s^{-1} (Symbols: ○, =separated; ◊, =non-separated)

5.4. Discussion

The results presented in this Chapter provided the first quantitative comparison of the mean, wave-induced and turbulent properties for the separated and non-separated flows over wind generated water waves at two different wind speeds. The results show that the waves over which the flow separation occurs are steeper and larger in amplitude than the waves with no flow separation. The results also show that the influence of flow separation is mainly restricted on the crest-to-trough region, i.e. leeward side of the wave and the wave trough (0^{o} to 270^{o} phase angles). The difference between the flow characteristics of the separated and non-separated flows typically increased with the phase angle from 0^{o} to 135^{o} and, decreased with the phase angle from 135^{o} to 270^{o} (-90^{o}). The maximum difference between the flow characteristics of the two types of flow is observed within the phase angles from 90^{o} to 135^{o} that is the core of the separation region. Within the separation region lower magnitudes of the streamwise velocity and higher magnitudes of the vorticity were observed for the separated flow. The results also show that within the separation zone, the turbulence is significantly enhanced and its effect is also extended to greater heights. However, the flow separation did not influence the turbulence behaviour and magnitude on the windward side of the wave. The profiles of the turbulent Reynolds stress show significant enhancement on the leeward side and in the wave trough. The enhanced Reynolds stress is positive in this region, which indicates that the separated flow enhances the downward momentum transfer on the leeward side and in the trough and its magnitude increases with the wind speed.

The profiles of the wave-induced velocity and Reynolds stress show that the flow separation influences the wave-induced characteristics over the entire waveform. The trends remain almost the same for the separated and non-separated flows but the flow separation enhances the magnitudes of the wave-induced properties within the distance of one to two significant wave heights from the water surface. The enhanced wave-induced Reynolds stress is negative, which shows that the waves with flow separation contribute significantly to the upward momentum transfer and this contribution increases with the wind speed.

CHAPTER 6

Near surface flow over air-liquid and air-solid interfaces

In this chapter the mean and turbulent characteristics over smooth and wavy water surfaces are compared with that over smooth and wavy walls.

6.1. Instantaneous velocity fields

The instantaneous velocity fields for the three configurations are shown in figure 6.1 to illustrate the overall flow dynamics. Figure 6.1a shows the instantaneous velocity field over a smooth wall (second configuration) at a wind speed of 4.4 m s^{-1}. The plot shows fairly uniform flow as expected. The velocity field over the wavy solid wall is shown in figure 6.1b at a wind speed of 4.4 m s^{-1}. The plot shows the flow separation and the separation vortex in the trough region. The velocity field over a water wave at a wind speed of 4.4 m s^{-1} is shown in figure 6.1c. The plot shows the flow separation off the wave crest and the separation zone within the trough. A burst is also observed on the windward face of the wave near the upstream end of the plot.

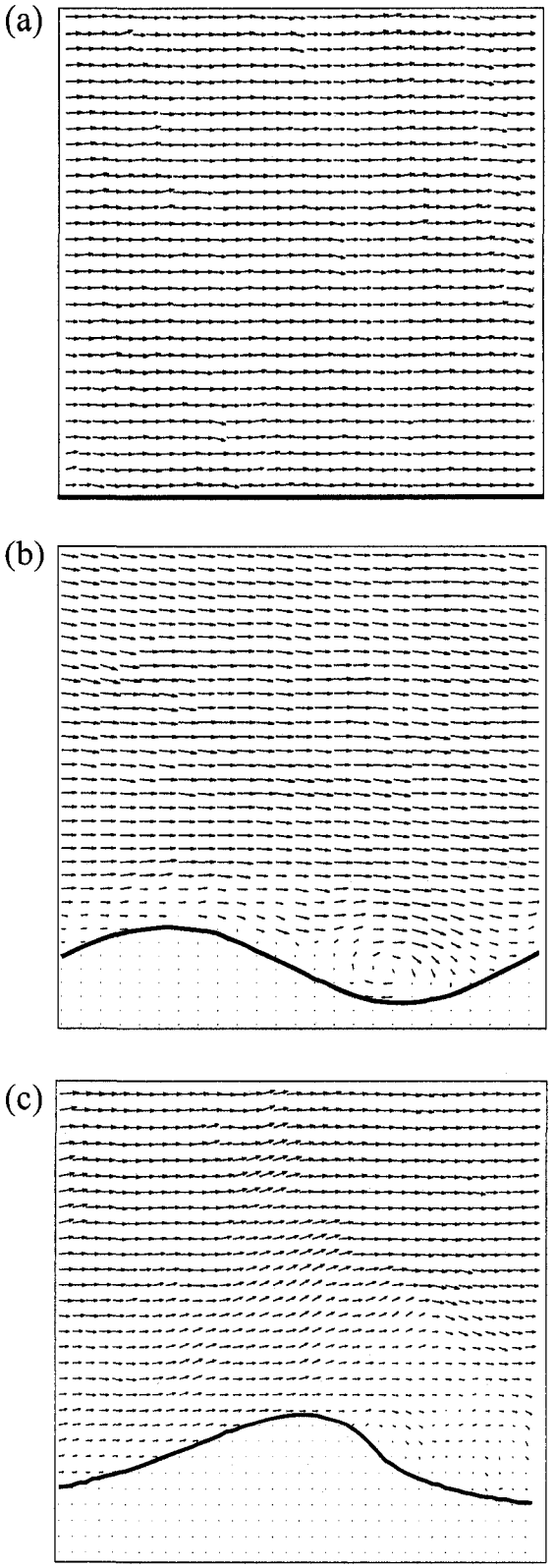

Figure 6.1. A snap short of instantaneous velocity fields at a wind speed of 4.4 m s^{-1}, (a) over the smooth wall, (b) over the wavy solid wall, (c) over the water wave

6.2. Mean streamwise velocity

The mean streamwise velocities were computed by time-averaging five minutes of the velocity data at each grid point and then by spatially averaging the time-averaged velocities at each height. The vertical profiles of the normalized mean streamwise velocity over the water and solid surfaces are shown in figure 6.2a, at different wind speeds. For all configurations, the plot shows that the magnitude of the streamwise velocity decreased monotonically towards the interface, as expected. For the flow over smooth and wavy walls at all wind speeds, the normalized profiles of mean streamwise velocity merged into their respective groups. However, for the flow over the water surface, the velocity profiles distribute into two distinct groups. One group corresponds to the wind speeds at which waves were not observed i.e. wind speeds ranging from 1.5 to 3 m s^{-1}. The other group corresponds to the wind speeds of 3.7 and 4.4 m s^{-1}, where surface waves were observed. The results show that the magnitude of the normalized velocity in the absence of waves is almost identical to that over the smooth wall. However, in the presence of water waves, the normalized velocity magnitudes are lower than that over the smooth wall and higher than that over the wavy wall. Quantitatively at wind speeds of 3.7 and 4.4 m s^{-1}, the magnitudes of mean streamwise velocity over the water waves are 6% and 13% lower than that over the smooth wall whereas, 25% and 85% higher than that over the wavy wall, respectively. The similarity in the normalized velocity profiles over the smooth wall and over the smooth water surface could be attributed to the similar nature of the shearing mechanism in the near-surface region. In both cases, the total stress in the near-surface region is the tangential or shear stress.

Whereas, when the waves appear on the water surface, a part of the stress is utilized as the waveform drag, which results in the reduction of the mean velocity than that over the smooth wall (Stewart 1970).

Banner and Peirson (1998) measured viscous stresses beneath the water surface. They found that at short fetches and lower wind speeds, the viscous stress constitutes almost 50% of the total stress. They further observed that this fraction decreases with an increase in fetch and wind speed. Kudryavtsev and Makin (2001) investigated the drag on the sea surface and argued that at low wind speeds, the viscous stress dominates the surface drag while the role of the form drag is negligible. With the increase of the wind speed the role of the form drag becomes pronounced. At wind speed $U_{10} > 10$ m s^{-1}, the surface drag is mainly supported by the wave induced and turbulent stresses. This fact is due to enhanced surface roughness which creates turbulence and decreases the relative speed of the airflow within few centimeters above the water-waves. The profiles in figure 6.2a show that the drag over the wavy wall is larger than that over the water surface.

The profiles of the mean streamwise velocity were used to estimate the friction velocity (u_*) by using the logarithmic law (Wu 1975). The values of u_* for all cases are presented in Table 6.1. Kawamura et al. (1981) computed the friction velocity by fitting the logarithmic law to the mean velocity profile. At a wind speed of 4.18 m s^{-1}, they reported the values of the friction velocity equal to 18.9 cm s^{-1}. Their friction velocity estimate was comparable to the present study (see Table 1). Stewart (1970) estimated the friction velocity equal to 10.10 cm s^{-1} at a fetch of 3.96 m and wind speed of 2.27 m s^{-1}, which is also consistent with the present study.

TABLE 6.1. Friction velocity at five different wind speeds

Mean Wind velocity (m/s)	Friction Velocity (cm/s)		
	Flow over smooth wall	Flow over wavy wall	Flow over water surface
1.5	8.63	15.75	6.39
2.1	12.43	23.75	9.03
3	16.98	32.29	12.22
3.7	20.53	39.38	14.94
4.4	24.32	47.68	17.48

The non-dimensional wall coordinates u^+ and y^+ were computed using the relations,

$$u^+ = \frac{(U - U_s)}{u_*} \tag{6.1}$$

$$y^+ = \frac{\xi u_*}{\nu_a} \tag{6.2}$$

where, U_s is the surface velocity and ν_a is the kinematic viscosity of air. For the flow over the water surface the values of U_s were estimated by using the relation $U_s = 0.55 \times u_*$ (Wu 1975), whereas for the flow over the solid surface due to no-slip condition the value of U_s was taken as zero. Figure 6.2b shows the mean velocity profiles in wall coordinates for all configurations.

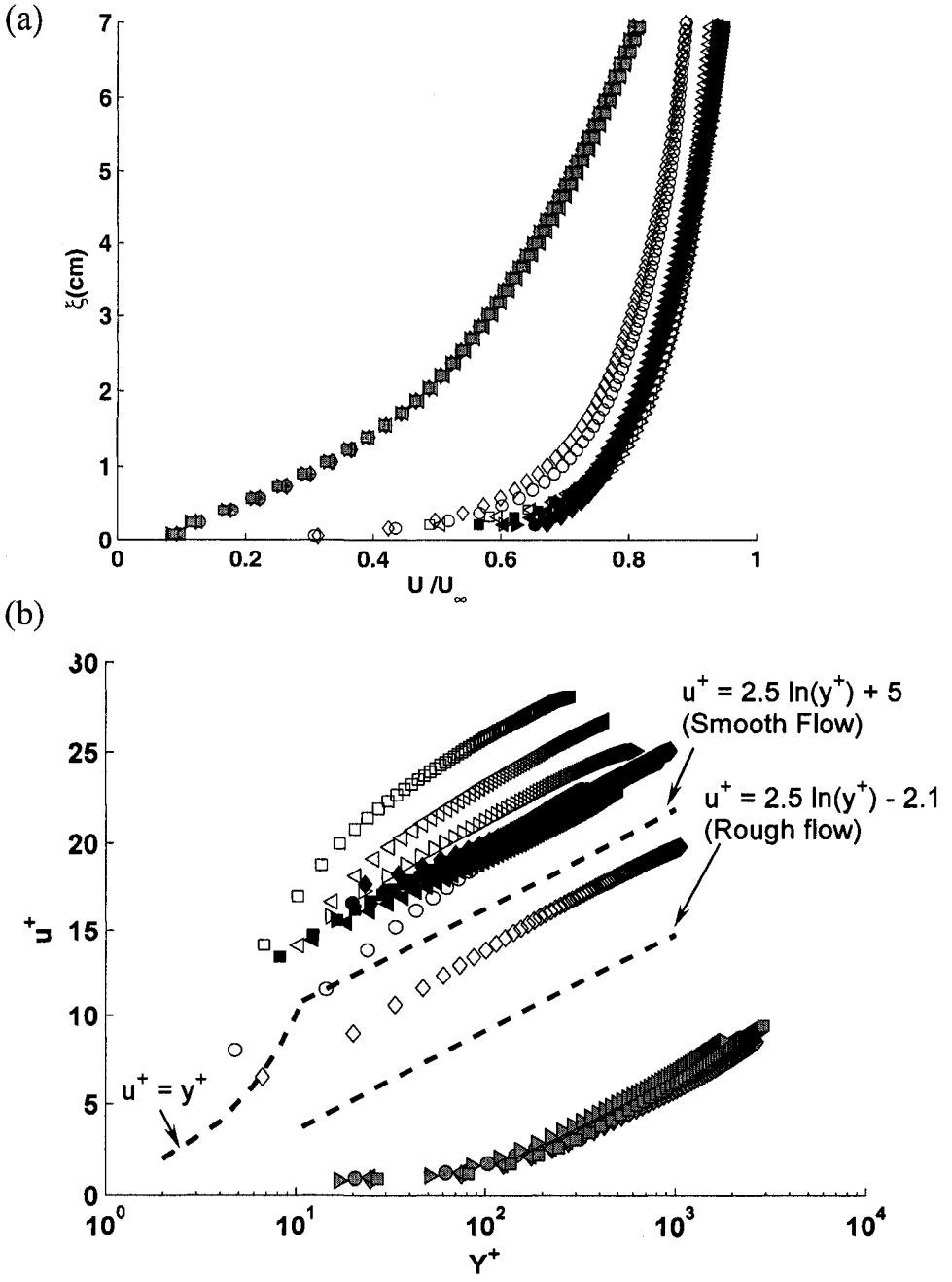

Figure 6.2: Normalized profiles of (a) mean streamwise velocities,(b) mean streamwise velocity in wall co-ordinates, averaged over 5 minutes of data, open symbols show flow over water surface and close (black) symbols show flow over solid wall, close (gray) symbols show flow over solid waves (symbols: □, =1.5 m s^{-1}; ◁, =2.1 m s^{-1}; ▷, =3 m s^{-1}; ○, =3.7 m s^{-1}; ◊ , =4.4 m s^{-1})

The theoretical lines representing the hydraulically smooth and rough flow regimes are also plotted for comparison. The plot shows that the flow over smooth wall falls in the smooth regime, while the flow over wavy solid wall was in the rough regime as expected. Another interesting observation is that unlike the profiles over solid wall which collapsed for each of the two configurations, the mean profiles over the water surface did not collapse but rather show a varying trend. The velocity profiles tend to move towards the rough regime with the increase in the wind speed. At the wind speed of 4.4 m s^{-1}, the mean velocity profile over water waves was in the transition regime. These results indicate that the hydrodynamic behaviour of the air velocity field over the water surface changes with the wind speed. Siddiqui and Loewen (2007) also observed a varying trend of the mean velocity profiles beneath water waves.

Several previous studies have also investigated the similarity between the airflow over wavy water surface and that over solid surface by comparing their mean velocity profiles. Stewart (1970) reported that the velocity profile over water waves is quantitatively similar to the profile over a rough plate. Hsu et al. (1981) argued that the mean airflow follows the waveform so in the wave-following system, the water waves could not be regarded as the surface roughness. They concluded that the mean velocity profile over the water surface is similar to that over a smooth wall. Dattari et al. (1977) stated that the airflow over the water surface corresponds to the turbulent flow over rough walls. One common feature observed in all of these studies is the logarithmic behaviour of the mean velocity profiles which led to the argument about the similarity between the flow above water waves and that over a solid wall. However, the presence of logarithmic velocity distribution in the boundary layer can be described based on the dimensional

arguments (Kundu 1990) and it does not necessarily imply the similarity between the flow adjacent to the water and solid surfaces (Siddiqui and Loewen 2007). Krogstad et al. 1992 and Krogstad and Antonia (1999) reported the influence of wall roughness on the mean velocity profiles within the boundary layer over a solid wall. They compared the flow properties for two surface conditions. The roughness of the surfaces was designed to produce the same effect on the mean velocity profiles. They reported that the surface geometry significantly affects the turbulent transport characteristics (Reynolds stress distribution, turbulent energy production and turbulent diffusion) of the flow, even when the two different roughness geometries have the same effect on the mean velocity. Therefore, it is reasonable to argue that the similarity between the mean velocity profiles is inadequate to relate the flow over undulating water surface to that over the solid wall. A comprehensive turbulent analysis is vital to understand if similarity exists between the flows over two different types of interfaces.

Various turbulent characteristics were computed from the turbulent velocity fields and a comparison is made for the flow over smooth and wavy water surfaces with the flow over smooth and wavy walls at different wind speeds. Note that the procedure of computing the turbulent velocity fields for all three configurations is already described in chapter 2.

6.3. Root-mean-square turbulent velocities

The profiles of normalized streamwise root-mean-square (RMS) turbulent velocities for all configurations are presented in figure 6.3a versus height, at different

wind speeds. The plots show that the data for each configuration falls into a distinct group indicating that the magnitude of horizontal turbulent velocity with respect to their respective velocity scale is influenced by the surface condition. The results show that with respect to their velocity scale (u_*), the horizontal turbulent velocity over the wavy solid wall has the lowest magnitude, while the flow over water surface has the largest horizontal turbulent velocity magnitude which is twice of that over the wavy solid wall. The magnitude of the horizontal turbulent velocity over the smooth wall is in between the two. The plot in figure 6.3a also shows that the trends of horizontal turbulent velocity in the near-surface region are different over the water and solid surfaces. Above the wavy solid wall, the horizontal turbulent velocity increased sharply over a height of 1.5 cm (i.e. the wave height of the solid wall) and then gradually decreased towards the free stream region. The profiles above the smooth solid wall also shows similar overall trend. As expected, the sharp increase in the horizontal turbulent velocity was not present which was attributed to the wavy solid wall. Over the water surface in the presence of waves, the horizontal turbulent velocity increased sharply immediately above the interface followed by a relatively sharp decrease within a height of less than 1 cm. Small variations were observed at greater heights. The profiles in the absence of water waves show a decreasing trend within a height of 1 cm from the surface followed by a gradual increase and then decrease in the velocity magnitude. Note that, the sharp increasing trend immediately above the water surface as observed in the presence of water waves was not found in the absence of waves which could be due to the unavailability of data in the immediate vicinity of the interface for the no wave cases. As mentioned earlier, the closest velocity vector was located at a height of 0.5 mm and 0.8 mm from the water and solid waves

respectively, while for the flow over smooth water (no waves) and smooth solid surfaces, the nearest velocity vector was located on average at a height of 2 mm from the surface. The difference in trends over water and solid surfaces indicates that the structure of horizontal turbulent velocity in the near-surface region is different for two surface configurations. One plausible reason for this behaviour is the difference in the hydrodynamic boundary condition for the horizontal velocity component. At the solid wall, the horizontal velocity should reach zero, while a non-zero horizontal velocity magnitude exists at the air-water interface.

The profiles of the RMS vertical turbulent velocity are plotted in figure 6.3b for all three configurations. The profiles for each configuration collapsed well into distinct groups. The profiles show a similar trend for all configurations however, in the presence of water waves, enhancement in vertical turbulent velocity is observed in the near-surface region. This indicates that water waves modify the vertical turbulent velocity structure in the near-surface region. Comparison of the magnitudes shows a trend similar to the horizontal turbulent velocity. That is, with respect to their velocity scale (u_*), the vertical turbulent velocity over the wavy solid wall has the lowest magnitude, while the flow over water surface has the largest vertical turbulent velocity magnitude. The magnitude of the vertical turbulent velocity over the smooth wall is in between the two.

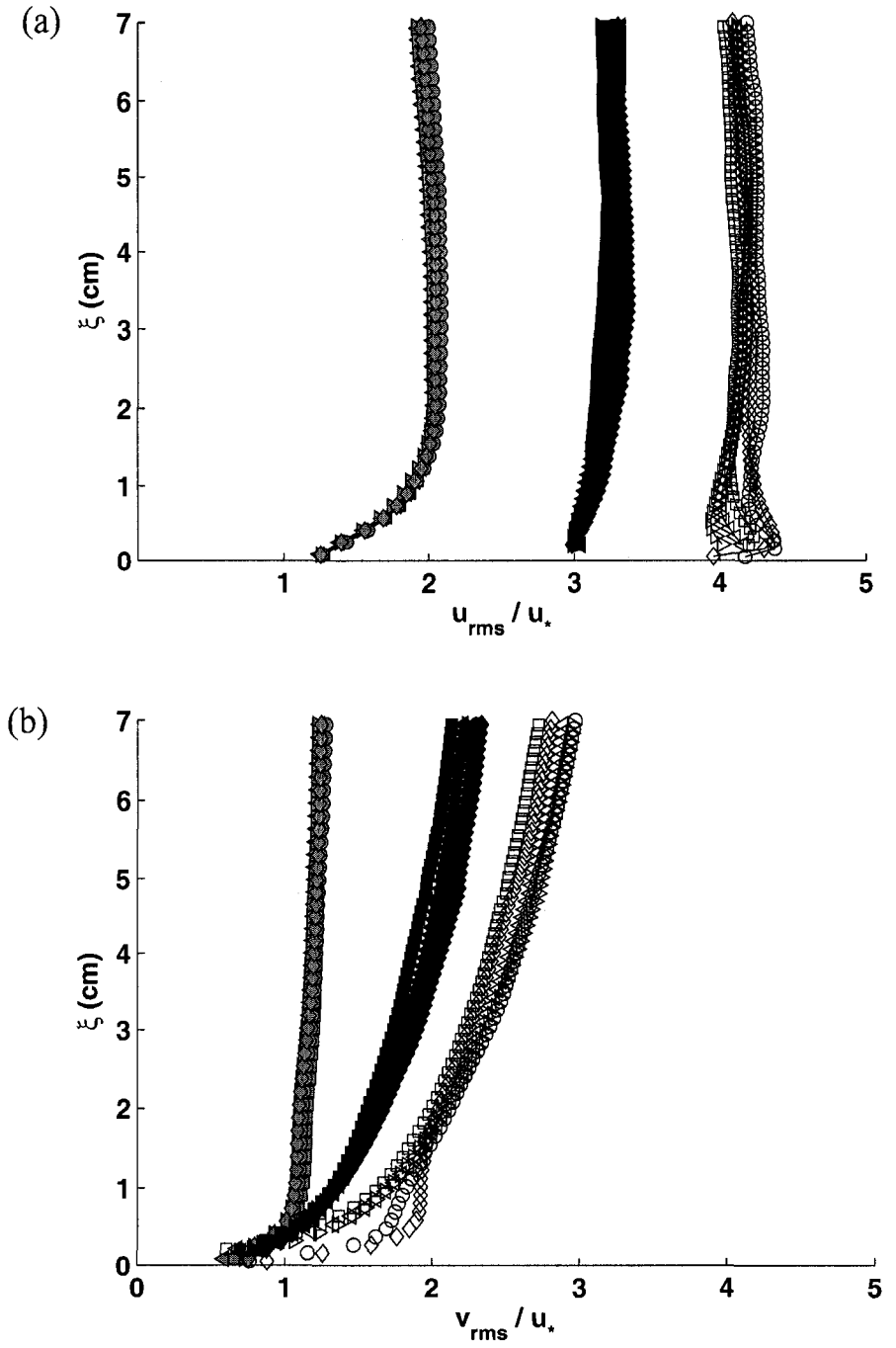

Figure 6.3: Normalized profiles of (a) Root-mean-square streamwise turbulent velocities, (b) Root-mean-square vertical turbulent velocity, averaged over 5 minutes of data, open symbols show flow over water surface and close (black) symbols show flow over solid wall, close (gray) symbols show flow over solid waves (symbols: □, =1.5 m s^{-1}; ◁, =2.1 m s^{-1}; ▷, =3 m s^{-1}; ○, =3.7 m s^{-1}; ◊ ,=4.4 m s^{-1})

The comparison of profiles in figure 6.3a and 6.3b shows that for all configurations, the magnitude of streamwise turbulent velocity is much larger than the vertical turbulent velocity. The profiles of horizontal and vertical turbulent velocities over the wave and smooth solid walls did not collapse into a single group. This is likely due to the reason that the roughness height for the wavy solid surface (1.5 cm) is several orders of magnitude larger than the roughness height of the smooth wall (of the order of microns). Furthermore, the height of the measurement region is about five times the roughness height. Thus, the effect of roughness is expected to be significant in this region for the wavy wall even if Townsend's (1976) similarity hypothesis is in effect.

6.4. Turbulent Reynolds stress

The vertical profiles of normalized Reynolds stress $(-\overline{u'v'})$ are presented in figure 6.4 for all configurations. All profiles show the classical behaviour i.e. a rapid increase in the Reynolds stress in the near-surface region (up to a height of approximately 1 cm from the surface) and then a gradual decrease towards zero in the free stream region. The profiles over the wave and smooth solid walls collapsed into their respective groups, whereas, the profiles over the water surface formed two distinct groups that correspond to the presence and absence of water waves. The magnitudes of the normalized Reynolds stress for the flow over wavy and smooth solid walls are comparable but lower than that over the water surface. Over the water surface, the magnitude of Reynolds stress is higher in the presence of waves. On average, the peak values of the normalized Reynolds stress

over the smooth and wavy water surfaces are 75% and 135% greater than that over the smooth or wavy wall, respectively, which indicates strong turbulence over the water surface than that over the smooth and wavy walls. The Reynolds stress distribution over the water surface also indicates that the effect of this turbulence is not restricted to the inner surface region but has also extended to the outer region.

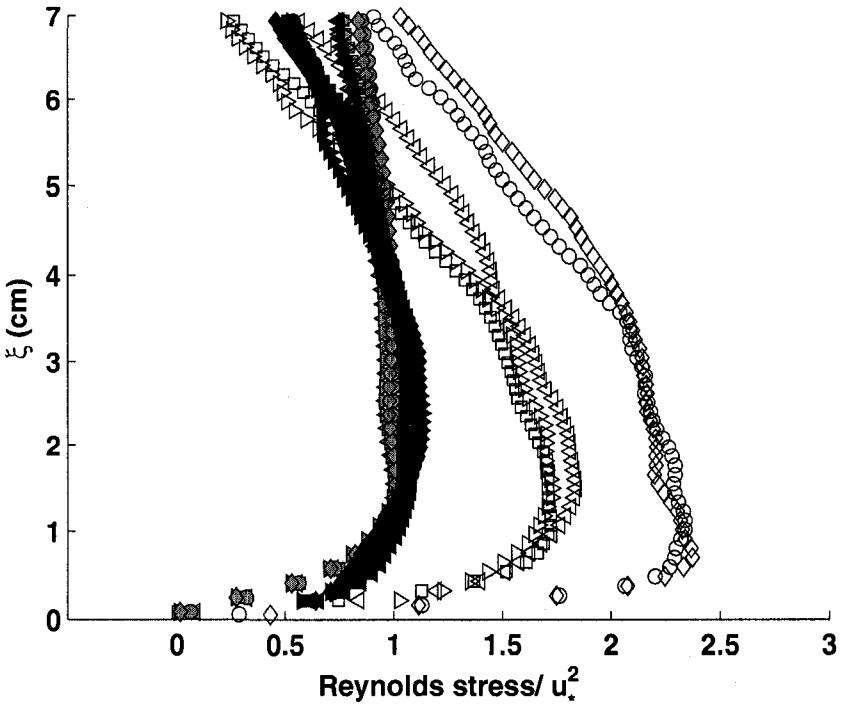

Figure 6.4: Normalized profiles of turbulent Reynolds stress for all three configurations, averaged over 5 minutes of data, open symbols show flow over water surface and close (black) symbols show flow over solid wall, close (gray) symbols show flow over solid waves (symbols: □, =1.5 m s^{-1}; ◁, =2.1 m s^{-1}; ▷, =3 m s^{-1}; ○, =3.7 m s^{-1}; ◊ ,=4.4 m s^{-1})

Reynolds stress is a quantitative measure of the turbulent part of the momentum flux towards the surface. Higher magnitudes of Reynolds stress over the water surface also indicate enhanced momentum flux from air to the water as compared to air to solid

wall. The results in figure 6.4 also suggest that the dynamic roughness (water waves) has a significant influence on the Reynolds stress in the near-surface region and it contributes to the enhancement of the momentum transfer. No such effect was observed over the solid wall. Based on the above results it can be argued that the Reynolds stress behaviour over the water surface is different from that over the solid surface under identical free-stream conditions.

6.5. Turbulent energy production

The turbulent kinetic energy production is computed using the equation 3.1. The data is normalized with the fetch and the corresponding friction velocities. The normalized profiles of turbulent kinetic energy production are plotted in figure 6.5 at different wind speeds. The profiles show similar grouping as for the Reynolds stress, i.e., each configuration over the solid wall has a distinct group, while over the water surface the grouping is based on the presence and absence of water waves. Profiles for all configurations show the classical behaviour i.e. peak production magnitude in the near surface region that decreased to zero in the free stream region. Significantly higher production magnitudes are observed over the water surface compared to the solid surface. The energy production over the water surface was found to be further enhanced in the presence of water waves. The enhanced energy production over water surface especially in the presence of water waves is likely due to the enhancement of the Reynolds stress.

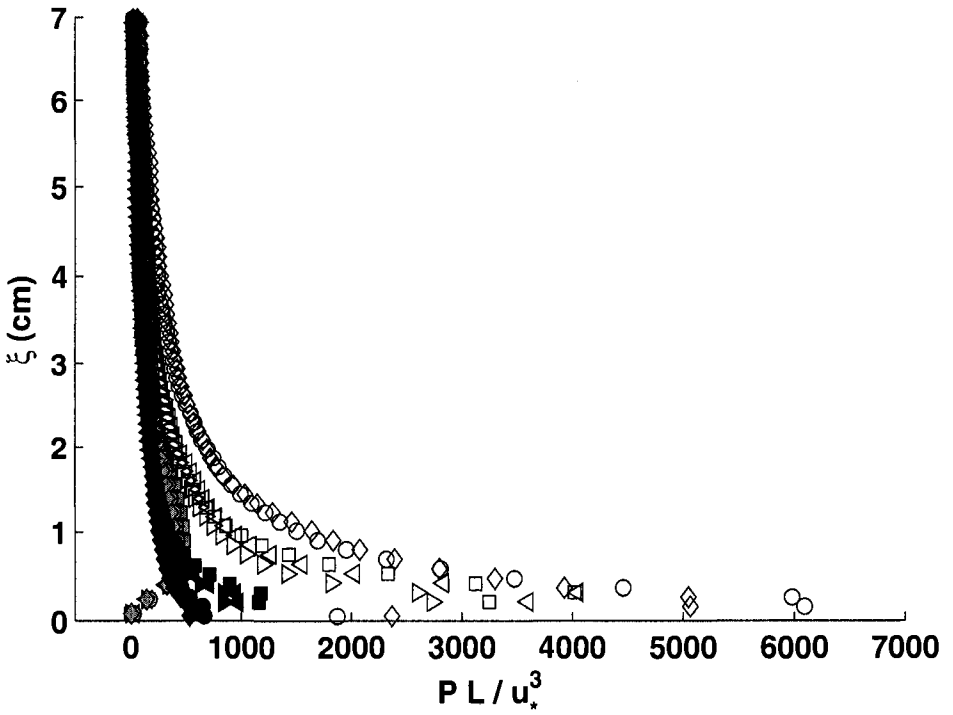

Figure 6.5: Normalized profiles of turbulent energy production, averaged over 5 minutes of data, open symbols show flow over water surface and close (black) symbols show flow over solid wall, close (gray) symbols show flow over solid waves (symbols: □, =1.5 m s^{-1}; ◁, =2.1 m s^{-1}; ▷, =3 m s^{-1}; ○, =3.7 m s^{-1}; ◇ ,=4.4 m s^{-1})

6.6. Turbulent Energy Dissipation

The rate of turbulent kinetic energy dissipation was computed using the equation 3.2. The profiles of the turbulent energy dissipation normalized by the fetch and the friction velocity are plotted in figure 6.6 as a function of height. The figure shows that for each configuration, the dissipation profiles collapsed into distinct groups. In all configurations, the maximum energy dissipation is observed adjacent to the surface which decreased rapidly in the near-surface region and then become almost constant. The

comparison shows that the higher magnitudes of normalized dissipation above the water surface, while the lower magnitudes over the wavy solid wall and the smooth solid wall in between the two. The results also show that the enhancement of dissipation magnitude from the outer region towards the surface is larger over the water surface as compared to that over both solid surfaces. The dissipation rate immediately adjacent to the smooth and wavy water surface is approximately a factor five higher than that at heights greater than 3 cm.

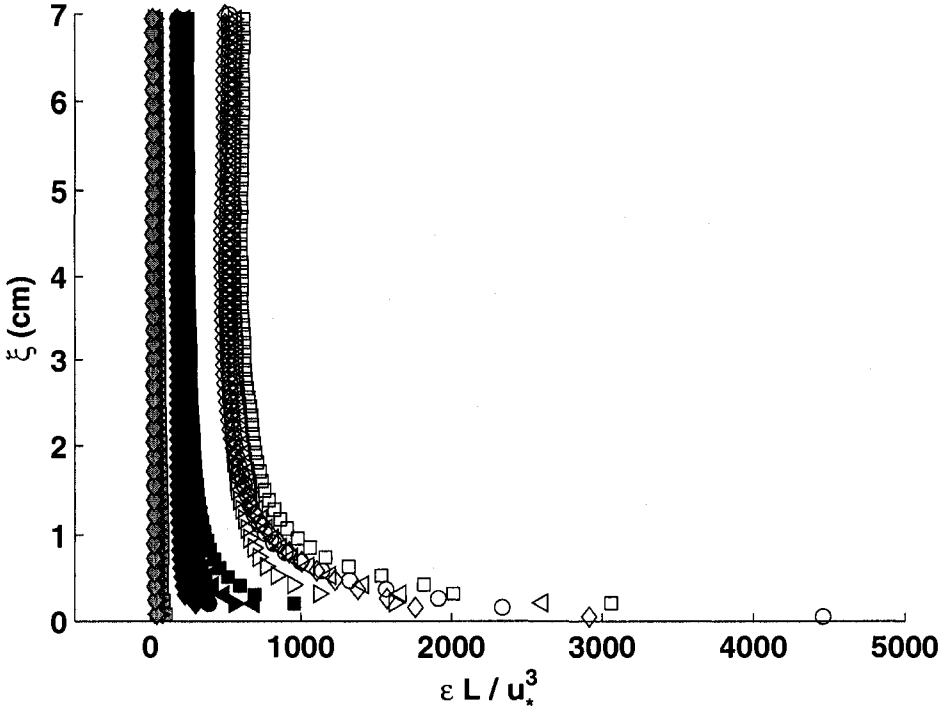

Figure 6.6: Normalized profiles of turbulent energy dissipation, averaged over 5 minutes of data, open symbols show flow over water surface and close (black) symbols show flow over solid wall, close (gray) symbols show flow over solid waves (symbols: □, =1.5 m s^{-1}; ◁, =2.1 m s^{-1}; ▷, =3 m s^{-1}; ○, =3.7 m s^{-1}; ◊ , =4.4 m s^{-1}))

The results in figure 6.6 also indicate that the influence of enhanced dissipation over air-water interface is extended to a height twice of that over air-solid interfaces. The profiles of dissipation over the water surface did not show distinct grouping for wavy and smooth water surfaces. Larger magnitudes of dissipation and a layer of enhanced dissipation immediately adjacent to the interface show that the dissipation behaviour over the water surface is different from that over the solid surface under identical free-stream conditions.

6.7. Root-mean-square turbulent vorticity

The turbulent vorticity was computed by using a central difference scheme at each grid point in the turbulent velocity field. The RMS turbulent vorticity (ω_{rms}) was computed at each height. The normalized RMS turbulent vorticity is plotted in figure 6.7 as a function of height. Kinematic viscosity and the friction velocity were used as normalizing parameters. The plot shows that the turbulent vorticity profiles are collapsed into distinct groups correspond to each configuration. Similar trends are observed in all cases i.e. the larger magnitudes of ω_{rms} close the surface which decreased rapidly in the near-surface region and then remained almost constant at greater heights. Similar to other turbulent characteristics, the results in figure 6.7 also show that the magnitudes of normalized ω_{rms} are larger above the water surface and lower above the wavy solid wall. Similar to the dissipation rate, the enhancement of the vorticity magnitude from the outer region towards the interface is larger over the water surface, particularly in the presence of waves. This indicates that the near-surface vortices over the water surface especially in

the presence of waves are much stronger than that in the outer region compared to that over the solid surfaces. The results also show that the maximum RMS vorticity observed near the wavy water surface is more than a factor of two larger than the one observed close to the solid wall. The vortices are the characteristic features of the turbulent flows and they play a significant role in the transport processes. The results in figure 6.7 suggests higher interfacial transport rate (e.g. interfacial heat transfer rate) over the water surface compared to the solid wall under the identical free stream conditions.

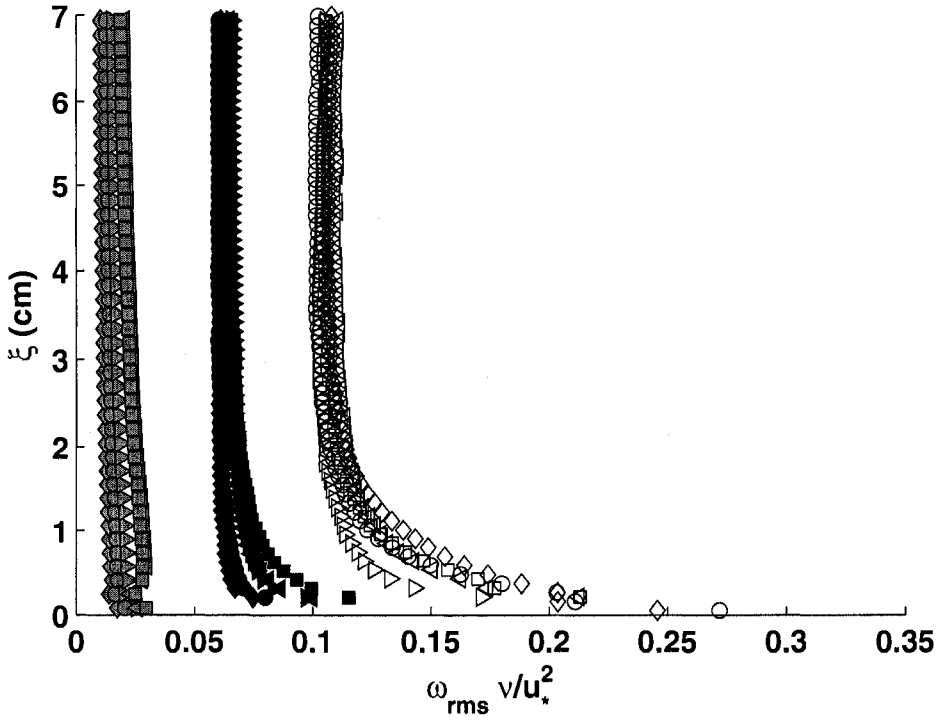

Figure 6.7: Normalized profiles of root-mean-square turbulent vorticity, averaged over 5 minutes of data, open symbols show flow over water surface and close (black) symbols show flow over solid wall, close (gray) symbols show flow over solid waves (symbols: □, =1.5 m s^{-1}; ◁, =2.1 m s^{-1}; ▷, =3 m s^{-1}; ○, =3.7 m s^{-1}; ◇, =4.4 m s^{-1})

6.8. Discussion

The results presented in the preceding section described the flow structure over water and solid surface for smooth and wavy conditions under identical free stream velocities. The mean velocity profiles for all surface configurations show the logarithmic behaviour. The profiles over the smooth solid wall collapsed in a narrow band and showed hydrodynamically smooth flow whereas, the profiles over wavy solid wall showed hydrodynamically rough condition and also collapsed in a narrow band. The flow over the water surface showed variation in the hydrodynamic behaviour with the change in wind speed. The flow in the absence of water waves (i.e. smooth water surface) were in the smooth regime, which shifts towards the rough regime with an increase in wind speed. These results show that the hydrodynamic behaviour over the water surface changes with wind speed due to the change in the surface condition. Thus, at a given free stream velocity, the hydrodynamic behaviour over the fixed roughness (solid wall) and dynamic roughness (water surface) is not necessarily similar.

The influence of surface condition on the flow behaviour was clearly visible in the profiles of various turbulent properties. The results show distinct groups that correspond to different surface conditions. The flow over the wavy and smooth solid walls formed distinct groups and did not collapse into a single group and as mentioned earlier, it is likely due to the reason that within the measurement height, the roughness height for the wavy solid wall (1.5 cm) is expected to have an influence, while for the smooth wall, the roughness effects are expected to be restricted within a very thin layer whose height is less than the nearest velocity grid point located at a distance of 2 mm from the surface.

The plots show that the normalized magnitudes of turbulent properties are largest over the water surface and smallest over the wavy solid wall, while the smooth solid wall is in between. Although in the absolute terms for a given wind speed, the magnitudes of turbulent properties over the wavy solid wall are larger in both inner and outer regions compared to that over smooth solid wall and water surface. The absolute magnitudes of turbulent properties are comparable over the smooth solid wall and water surface in the outer region and larger over the water surface in the near-surface region.

The normalized plots represent the relative magnitude of the given property with respect to the magnitude of a characteristic scale. For the turbulent characteristics in boundary layer flows, friction velocity (u_*) is considered as the characteristic velocity scale (Pope 2000). The results in Table 1 shows that the friction velocity magnitudes above the wavy solid wall are largest, followed by that over the smooth wall and then that over the water surface. The friction velocity is a measure of the shear stress at the interface or in other words, the force exerted by the fluid on the surface. The above results show that under identical free-stream velocities, the stresses exerted by the fluid on the surface are largest over the wavy solid wall and lowest over the water surface. From the turbulence perspective, the present results show that with respect to the surface stresses, the magnitude of the turbulent properties over the water surface is largest followed by the smooth wall and then the wavy solid wall. The results also show that over the water surface, the magnitude of turbulent properties increases significantly in the near-surface region when waves appear on the water surface. Thus, it can be argued that with respect to the surface stresses, the turbulence is enhanced over the wavy water surface while its magnitude is reduced over the wavy solid surface. Another feature that distinct the flow

behaviour over the solid and water surfaces is the level of turbulence enhancement in the near-surface region. The above results show that the level of enhancement of the dissipation rate and RMS turbulent vorticity from the outer region to the near-surface region is higher over the water surface especially in the presence of waves as compared to that over the solid surface.

The above results and discussion showed that there are similarities and dissimilarities in the structure of flow above water and solid interfaces. Although the trends in profiles over water and solid surfaces are mostly similar, the relative magnitudes of turbulent properties and their level of enhancement towards the surface are different over water and solid surfaces. In particular, due to the significant difference in the turbulence magnitudes with respect to the surface stresses, the models for the flow over solid surfaces may not accurately predict the flow properties over the water surface especially the near-surface transport processes.

CHAPTER 7

Conclusions and future recommendations

7.1. Summary

The interaction of waves and wind is a two-way process. Due to the coupling between wind and waves, the region immediately above the water surface plays a crucial role in controlling the fluxes of momentum, heat and mass. The visual inspections showed that the airflow structure within the near-surface region is very complex and different from the flow structure at greater heights. The dynamical processes in the near-surface region include airflow separation immediately adjacent to the water surface (Kawai 1981), coherent structures (Komori et al. 1993), a high shear layer and active bursting and sweeping phenomena (Kawamura and Toba 1988). However the evidence of the existence of these dynamical processes is mainly based on qualitative observations. Several laboratory studies have been conducted to study the flow structure above the waves. Majority of these studies used point measurement techniques and measured airside velocity at a fixed height from the wave crest. Point measurement techniques can provide a time history of the flow but it is not capable of providing instantaneous spatial structure of the flow. In addition, this technique cannot be used for measurements in the region between the wave crest and trough, where any particular spatial location lies sometimes in water and sometimes in air.

Due to the unavailability of the accurate measurements close to the surface, the theoretical models available in the literature show substantial disagreement. The oceanographers and meteorologists ignore the near surface turbulence and consider this region as a black box (Edson et al. 1999). Furthermore, the climate models (that are used to calculate the global heat and mass transfer) are based on the bulk formulae in which air properties are measured at a height of 10 m above the water surface. However, the assumption that the air properties at 10 m height are good representative of the properties at the surface is questionable and leads to inaccurate flux estimates. The empirical relation developed to estimate the turbulent characteristics in the near wall region are often used to estimate the desired turbulent quantities over the water surface where direct measurement is very difficult. However the use of these empirical relations for the flow over the water surface is questionable (Perry et al. 1987).

Due to the challenging nature, not enough work has been done in the near surface region above the wave. Recently, few researchers (Reul et al. 1999, Veron et al. 2007, Reul et al. 2008) used PIV technique and reported quantitatively, the instantaneous structure of velocity and vorticity fields in the crest trough region. However, none of these studies reported the mean and turbulent properties within the crest-trough region, specifically in the separation zone, and the influence of airflow separation on the process of momentum transfer across the air-water interface. A detailed investigation of the flow structure in this region is vital in order to obtain the understanding of the fundamental transport processes.

This thesis has reported on a series of laboratory experiments to investigate the airflow structures above wind waves especially within the crest-trough region. Detailed quantitative comparison is also made between the flow structure immediately over air-water and air-solid interfaces. PIV technique was used to measure the instantaneous two-dimensional velocity field over different types of interfaces at the same location, under identical flow conditions. A novel approach is used to separate the wave-induced component from the instantaneous velocity fields. In addition, the mean, turbulent and wave-induced properties were presented as a function of wave phase. The results provided the first direct evidence of the downward and upward momentum transfer from wind to waves and vice-versa. To the best of our knowledge this is the first study, reporting the quantitative analysis of the airflow structure in the immediate vicinity of the air-water interface, specifically within the crest-trough region. This research is aimed to improve the fundamental understanding of the physical processes that influence the air-water mass, heat and momentum exchange.

The experimental setup, measurement technique and the procedure used to compute the surface wave profiles were described in Chapter 2. The experiments were conducted in the same wind wave flume for three different configurations. In the first configuration, the lower half of the flume was filled with clean tap water. In the second configuration, the lower half of the flume was covered with a 5 mm thick hardboard panel, which was considered as a smooth wall. In the third configuration, a corrugated sheet with wave height of 1.5 cm is place on the hardboard panel, which was considered

as the wavy solid wall. For all three configurations, the velocity fields were measured at the same wind speeds ranging from 1.5 m s^{-1} to 4.4 m s^{-1} and at a fetch of 2.1 m.

In Chapter 3, the instantaneous, mean and turbulent flow characteristics were described immediately above the wind-sheared water surface in the presence and absence of surface water waves. The results show that the surface waves significantly influence the near-surface airside velocity fields. The mean velocity magnitudes and the tangential stresses are decreased when waves appeared on the water surface. The results also show that the flow dynamics within the region bounded between the wave crest and trough are significantly different from that at greater heights. Within a 2 cm layer adjacent to the water surface, the vorticity was enhanced by approximately an order of magnitude and the energy dissipation rate was enhanced by a factor of seven at all wind speeds. The maximum energy production was also observed within a distance equal to the significant wave height from the surface. These results also provide the quantitative evidence of the enhanced vorticity layer immediately adjacent to the water surface which was speculated in the previous study through qualitative visualizations. The busting and sweeping processes similar to that over the solid wall were also observed above the surface waves. The present results demonstrate that the flow characteristics and the associated physical processes occurring within the layer immediately adjacent to the water surface whose thickness is of the order of the significant wave height, cannot be predicted from measurements taken at greater heights.

In Chapter 4 various turbulent and wave-induced properties were described as a function of phase and height in the immediate vicinity of the waves. The results show that the flow behaviour varies significantly over the waveform in the near-surface region. At heights greater than three times the significant wave height from the water surface, the wave-induced effects become negligible. The phase-averaged velocity, vorticity and Reynolds stress profiles indicate different types of flow structures on the windward and leeward faces of the wave. Along the windward side of the crest, the wave-induced velocity is in the direction of wave propagation whereas, along the leeward side of the crest, the wave-induced velocity is in the direction opposite to the wave propagation. The thickness of the vorticity layer is minimum above the crest and maximum above the trough. The largest magnitudes of vorticity are observed within the separation zone on the leeward side. The results also show that the wave-induced Reynolds stress contributes to the upward momentum transfer along the entire waveform whereas the turbulent Reynolds stress mainly supports the downward momentum transfer. On the windward face of the crest, a layer of constant turbulent Reynolds stress is observed within the bursting region whereas on the leeward face of the crest, significantly high magnitudes of turbulent Reynolds stress is observed within the separated flow region. In the immediate vicinity of the air-water interface, the momentum is transferred from waves to wind along the windward side, whereas, the momentum transfer is from wind to waves along the leeward side.

The results presented in Chapter 5, provided the first quantitative comparison of the mean, wave-induced and turbulent properties for the separated and non-separated

flows over wind-generated water waves at two different wind speeds. A threshold-based algorithm was developed to identify the velocity fields with flow separation. The results show that the waves over which the flow separation occurs are steeper and larger in amplitude than the waves with no flow separation. The results also show that the influence of flow separation is mainly restricted on the crest-to-trough region. The turbulence is significantly enhanced within the separation zone. However, the flow separation did not influence the turbulence behaviour and magnitude on the windward side of the wave. The results also show that the separated flow enhances the downward momentum transfer on the leeward side and in the trough. The flow separation influences the wave-induced characteristics over the entire waveform. The trends remain almost the same for the separated and non-separated flows but the flow separation enhances the magnitudes of the wave-induced properties within the distance of one to two significant wave heights from the water surface. The enhanced wave-induced Reynolds stress is negative, which shows that the waves with flow separation contribute significantly to the upward momentum transfer and this contribution increases with the wind speed.

Chapter 6 is focused on a detailed quantitative comparison between the airflow structures over smooth and wavy water and solid surfaces. The mean velocity profiles for all surface configurations show the logarithmic behaviour. The results show that the flow over smooth wall falls in the smooth regime and the flow over wavy wall was in the rough regime as expected, whereas the flow over the water surface shows variable trend. The flow in the absence of water waves were in the smooth regime, which shifts towards the rough regime with an increase in wind speed. Thus, at a given free stream velocity,

the hydrodynamic behaviour over the fixed roughness and dynamic roughness is not necessarily similar. The influence of surface condition on the flow behaviour was clearly visible in the profiles of various turbulent properties. The magnitude of turbulent properties increases significantly in the near-surface region when waves appear on the water surface. Thus, it can be argued that the turbulence is enhanced over the wavy water surface compared to that over the wavy solid surface. The results also show that the level of enhancement of the dissipation rate and RMS turbulent vorticity from the outer region to the near-surface region is higher over the water surface especially in the presence of waves as compared to that over the solid surface. These results showed that there are similarities and dissimilarities in the structure of flow above water and solid interfaces. Although the trends in profiles over water and solid surfaces are mostly similar, the relative magnitudes of turbulent properties and their level of enhancement towards the surface are different over water and solid surfaces. In particular, due to the significant difference in the turbulence magnitudes with respect to the surface stresses, the models for the flow over solid surfaces may not accurately predict the flow properties over the water surface especially the near-surface transport processes.

7.2. Research contributions

The main contributions of this research to the scientific knowledge and techniques can be listed as follows:

- Measurement of the two-dimensional velocity field within the crest-trough region over wind-generated water waves.
- Development of the scheme to compute the location of the fluctuating air-water interface in both time and space.
- Provided the first quantitative evidence of the enhanced vorticity layer immediately adjacent to the water surface which was speculated in the previous study through qualitative visualizations.
- Provided the first direct evidence of the upward momentum transfer from young wind waves to the atmosphere.
- Developed a novel technique to separate the wave-induced component from the instantaneous two-dimensional velocity fields.
- Quantified the contribution of the near surface turbulence and wave-induced motion to the process of momentum transfer across the air-water interface.
- Developed an algorithm to segregate the separated and non-separated velocity fields.
- Provided the first quantitative comparison of the mean, wave-induced and turbulent properties for the separated and non-separated flows over wind-generated water waves.

- Provided the first detailed quantitative comparison between the airflow structures immediately over smooth and wavy water and solid surfaces.

7.3. Recommendations for future work

The results presented in this research are unique and a step towards improving our fundamental understanding of the airside turbulent structure over wind-sheared water surfaces. However, there are many issues which still need further consideration. Following are some recommendations for future work.

1. Low wind speeds and short fetch were the limitations of this study. Therefore PIV measurements at higher wind speeds and longer fetch are recommended for future work.
2. The surface waves develop with fetch. The present measurements were conducted at a fixed fetch. To investigate the fetch dependency on the turbulent flow characteristics over wind-sheared water surface, the measurements at different fetches are recommended.
3. The present measurements were conducted under neutral condition. That is, the air and water were at the room temperature. In order to investigate the influence of the temperature gradient on the process of momentum transfer, it is recommended that the airside velocity measurement should be taken in the presence of temperature gradient between the two fluids.
4. Simultaneous air and water side measurements are also recommended that will help in a better understanding of the interfacial transport phenomenon.

7.4. Publications

7.4.1. Refereed Journals

1. Shaikh N. and Siddiqui K., (2008): "An experimental investigation of the near surface flow over air-liquid and air-solid interfaces", Physics of Fluids, (submitted)

2. Shaikh N. and Siddiqui K., (2008): "Wave-induced flow structure over wind-generated water waves", Journal of Fluid Mechanics, (submitted)

3. Shaikh N. and Siddiqui K., (2008): "Airside velocity measurements over the wind-sheared water surface using Particle Image Velocimetry", Ocean Dynamics, 58, 58-79

4. Nasiruddin and Siddiqui K., (2007): "Heat transfer augmentation in a heat exchanger tube using a baffle", International Journal of Heat and Fluid Flow, 28, 318-328

5. Shaikh N. and Siddiqui K., (2008): "An experimental analysis of the separated and non-separated flow fields over wind generated water waves" (in preparation)

7.4.2. Conferences

1. Shaikh N. and Siddiqui K., "An experimental Investigation of the Reynolds stress distribution over wind generated water waves" 22nd Canadian Congress of Applied Mechanics, Halifax, May 31-June 4, 2009 (submitted)

2. Shaikh N. and Siddiqui K., "An experimental Investigation of the airflow structure over solid and wind generated water waves" 22nd Canadian Congress of Applied Mechanics, Halifax, May 31-June 4, 2009 (submitted)

3. Shaikh N. and Siddiqui K., "Wave-induced effect on the airside velocity field above the wind generated water waves", ASME Fluid Engineering Division Summer Conference, Florida, August 10-14, 2008

4. Gajusingh S.T., Shaikh N. and Siddiqui, K., "The impact of the vortex induced by a baffle on the turbulent structure", ASME Fluids Engineering Division Summer Conference, Florida, August 10-14, 2008

5. Shaikh N. and Siddiqui K., "An Experimental Investigation of the Flow Structure over Air-Water and Air-solid Interfaces", Canadian Society for Mechanical Engineering, Ottawa, June 5-8, 2008

6. Shaikh N. and Siddiqui K., "Airside velocity measurement above the wind-generated water waves", 5th ASME_JSME Joint Fluids Engineering Conference, San Diego, California, July 30-August 2, 2007

7. Shaikh N. and Siddiqui K., "Velocity and vorticity distribution within the airside boundary layer over the wind-sheared water surface" 21st Canadian Congress of Applied Mechanics, Toronto, June 3-7, 2007

8. Shaikh N., Gajusingh S.T. and Siddiqui , K. "Flow variations in a channel due to the presence of a baffle", 21st Canadian Congress of applied Mechanics, Toronto, June 3-7, 2007

9. Siddiqui, K. and Shaikh, N. "Turbulent structure above wind-sheared air-water interface" 59th Annual Meeting of the Division of Fluid Dynamics, American Physical Society, Tampa Bay, Florida, November 19-21, 2006

REFERENCES

Anisimova Y. P., Makova V. I., Nikitina Y. A. and Speranskaya A. A., (1982): "Momentum flux spectrum above a developing wind wave", *Atmospheric and Oceanic Physics*, **18**, 435-439.

Antonia R. A. and Chambers A. J., (1980): "Wind wave induced disturbances in the marine surface layer", *J. Physical Oceanography*, **10**, 611-622.

Anotonia R. A. and Krogstad R. A., (2001): "Turbulence structure in boundary layers over different types of surface roughness", *Fluid Dynamics Research*, **28**, 139-157.

Balint J. L., Wallace J. M. and Vukoslavcevi P., (1991): "The velocity and vorticity fields of a turbulent boundary layer Part 2 statistical properties", *J. Fluid Mech.*, **288**, 53-86.

Banner M. L. and Melville W. K., (1976): "On the separation of air flow over water waves", *J. Fluid Mech.*, **77**, 825-842.

Banner M. L. and Peirson W. L., (1998): "Tangential stress beneath wind-driven air-water interfaces", *J. Fluid Mech.*, **364**, 115-145.

Benilov A. Y., Kouznetsov O. A. and Panin G. N., (1974): "On the analysis of wind wave-induced disturbances in the atmospheric turbulent surface layer", *Boundary Layer Meteorology*, **6**, 269-285.

Chambers A. J. and Antonia R. A., (1980): "Wave induced effect on the Reynolds shear stress and heat flux in the marine surface layer", *J. Physical Oceanography*, **11**, 116-121.

Cowen E. A. and Monismith S. G., (1997): "A hybrid digital particle tracking velocimetry technique", *Exp. Fluids*, **22**, 199-211.

Csanady G. T., (1984): "The free surface turbulent shear layer", *J. Physical Oceanography*, **14**, 402-411.

Dattatri J., Shankar J. and Raman H., (1977): "Wind velocity distribution over wind generated water waves", *Coastal Engineering*, **01**, 243-260.

Davidson K. L. and Frank A. J., (1973): "Wave related fluctuations in the airflow above natural waves", *J. Physical Oceanography*, **3**, 102-119.

Davis R. E., (1970): "On the turbulent flow over a wavy boundary", *J. Fluid Mech.* **42**, 721-731.

Donelan M. A., Babanin A. V., Young I. R. and Banner M. L., (2006): "Wave-follower field measurements of the wind input spectral function. Part II: Parameterization of the wind input", *J. Physical Oceanography*, **36**, 1672-1689.

Doron P., Bertuccioli L., Katz J. and Osborn T. R., (2001): "Turbulence characteristics and dissipation estimates in the coastal ocean bottom boundary layer from PIV Data", *J. Physical Oceanography*, **31**, 2108-2134.

Edson J., Paluszkiewicz T., Sandgathe S., Vincent L., Goodman L., Curtin T., Hollister J. and Colton M., (1999): "Coupled Marine Boundary Layers and Air-Sea interaction Initiative: Combining Process Studies, Simulations, and Numerical Models", *Office of Naval Research*, Revision **5.0**.

Fincham A. M. and Spedding G. R., (1997): "Low cost, high resolution DPIV for measurement of turbulent fluid flow", *Exp. Fluids*, **23**, 449-462.

Frederick K. A. and Hanratty T. J., (1988): "Velocity measurements for a turbulent non separated flow over solid waves", *Exp. Fluids*, **6**, 477-486.

Friebel H. C., (2005): "Air-sea momentum flux measurements in the surf zone over breaking waves", *Ph.D. thesis*, Stevens Institute of Technology, Hoboken, NJ.

Grachev A. A. and Fairall C. W., (2000): "Upward momentum transfer in the marine boundary layer", *J. Physical Oceanography*, **31**, 1698-1711.

Hare J. E., Hara T., Edson J. B. and Wilczak J. M., (1997): "A similarity analysis of the structure of air flow over surface waves", *J. Physical Oceanography*, **27**, 1018-1037.

Harris D. L., (1966): "The wave-driven wind", *Atmospheric Science*, ***23***, 688-693.

Hidy G. M. and Plate E. J., (1966): "Wind action on water standing in a laboratory channel", *J. Fluid Mech.* **26**, 651-687.

Hristov T., Friehe C. and Miller S., (1998): "Wave-coherent fields in air flow over ocean waves: identification of cooperative behaviour buried in turbulence", *Physical review letters*, **81** (23), 5245-5248.

Hsu C. T., Hsu E. Y. and Street R. L., (1981): "On the structure of turbulent flow over a progressive water wave: theory and experiment in a transformed, wave-followed co-ordinate system", *J. Fluid Mech.*, **105**, 87-117.

Hsu C. T. and Hsu E. Y., (1983): "On the turbulent flow over a progressive water wave: theory and experiment in a transformed wave following coordinate system. Part 2", *J. Fluid Mech.*, **131**, 123-153.

Hussain A. K. M. F. and Reynolds W. C., (1970): "The mechanics of an organized wave in turbulent shear flow", *J. Fluid Mech.*, **41**, 241-258.

Ichikawa H. and Imasato N., (1976): "The wind field over wind waves", *Oceanographical Society of Japan*, **32**, 271-283.

Janssen P. A. E. M., (1989): "Wave induced stress and drag of air flow over sea waves", *J. Physical Oceanography*, **19**, 745-754.

Kato H. and Sano K., (1971): "An experimental study of the turbulent structure of wind over water waves", *Report of the Port and Harbour Research Institute*, **10**, 3-42.

Kawai, S., (1981): "Visualization of airflow separation over wind wave crest under moderate wind", *Boundary Layer Meteorology*, **21**, 93-104.

Kawai S., (1982): "Structure of air flow separation over wind wave crests", *Boundary Layer Meteorology*, **23**, 503-521.

Kawamura H., Okuda K., Kawai S. and Toba Y., (1981): "Structure of turbulent boundary layer over wind waves in a wind wave tunnel", *Tohoku Geophysical Journal*, **28**, 69-86.

Kawamura H. and Toba Y., (1988): "Ordered motion in the turbulent boundary layer over wind waves", *J. Fluid Mech.*, **197**, 105-138.

Keirsbulck L., Labraga L., Mazouz A. and Tournier C., (2002): "Surface roughness effects on turbulent boundary layer structures", *J. Fluids Engg.*, **124**, 127-135.

Komori S., Nagaosa R. and Murakami Y., (1993): "Turbulence structure and mass transfer across a sheared air-water interface in wind-driven turbulence", *J. Fluid Mech.*, **249**, 161-183.

Krogstad P. A., Antonia R. A. and Browne L. W., (1992): "Comparison between rough and smooth wall turbulent boundary layers", *J .Fluid Mech.*, **245**, 599-617.

Krogstad P. A. and Antonia R. A., (1999): "Surface roughness effects in turbulent boundary layers", *Exp. Fluids*, **27**, 450-460.

Kudryavtsev V. N. and Makin V. K., (2001): "The impact of air-flow separation on the drag of the sea surface", *Boundary Layer Meteorology*, **98**, 155-171.

Kundu P. K., (1990): "Fluid Mechanics" *Academic Press.*

Lai R. J. and Shemdin O. H., (1971): "Laboratory investigation of air turbulence above simple water waves", *J. Geophysical Research*, **76** (30), 7334-7350.

Liberzon A., Luthi B., Guala M. and Kinzelbach W., (2005): "Experimental study of the structure of flow regions with negative turbulent kinetic energy production in confined three-dimensional shear flows with and without buoyancy", *Phys. Fluids*, **17** (9): 1-11.

Makin V. K., Kudryavtsev V. N. and Mastenbroek, C., (1994): "Drag of the sea surface", *Boundary Layer Meteorology*, **73**, 159-182.

Mastenbroek C., Makin V. K. Garat M. H. and Giovanangeli J. P., (1996): "Experimental evidence of the rapid distortion of turbulence in the air flow over water waves", *J. Fluid Mech.*, **318**, 273-302.

Mete B. U., Donelan M. A., Hara T. and Bock E. J., (2002): "Laboratory studies of wind stress over surface waves", *Boundary Layer Meteorology*, **102**, 301-331.

Miles J. W., (1957): "On the generation of the surface waves by shear flows", *J. Fluid Mech.*, **6**, 568-582.

Monin A. S. and Obukhov A. M., (1954): "Basic laws of turbulent mixing in the surface layer of the atmosphere", *Tr. Akad. Nauk SSR, Geofiz Inst.*, **151**, 163-187.

Obukhov A. M., (1946): "Turbulence in an atmosphere with a non uniform temperature", *Boundary Layer Meteorology*, **2**, 7-29.

Papadimitrakis Y., Hsu E. and Street R., (1986a): "The structure of the turbulent boundary layer over a mobile and deformable boundary", *Exp. Fluids*, **4**, 97-106.

Papadimitrakis Y. A., Hsu E. Y. and Street R. L., (1986b): "The role of wave induced pressure fluctuations in the transfer processes across an air-water interface", *J. Fluid Mech.*, **170**, 113-137.

Peirson W. L., (1997): "Measurement of surface velocities and shears at a wavy air-water interface using particle image velocimetry", *Exp. Fluids*, **23**, 427-437.

Peirson W. and Banner M., (2003): "Aqueous surface layer flows induced by microscale breaking wind waves", *J. Fluid Mech.*, **479**, 1-38.

Perry A. E., Lim K. L. and Henbest S. M., (1987): "An experimental study of the turbulence structure in smooth- and rough-wall boundary layers", *J. Fluid Mech.*, **177**, 437-466.

Phillips O. M., (1957): "On the generation of the surface waves by turbulent wind" *J. Fluid Mech.*, **2**, 417-445.

Pope S.B., (2000): "Turbulent Flows", *Cambridge University Press New* York, N.Y.

Prasad A. K., Adrian R. J., Landreth C. C., and Offutt P. W., (1992): "Effect of resolution on the speed and accuracy of particle image velocimetry interrogation", *Exp. Fluids*, **13**, 105-116

Qiu B., Chen, S. and Hacker, P., (2004): "Synoptic-scale air-sea flux forcing in the western North Pacific: Observations and their impact on SST and the mixed layer", *J. Physical Oceanography*, **34**, 2148-2159.

Reul N., Branger H. and Giovanageli J. P., (1999): "Air flow separation over unsteady breaking waves", *Phys. Fluids*, **11**, 1959-1961.

Reul N., Branger H. and Giovanageli J. P., (2008): "Air flow separation over short-gravity breaking waves", *Boundary Layer Meteorology*, **126**, 477-505.

Shaikh N. and Siddiqui M. H. K., (2008): "Airside velocity measurements over the wind-sheared water surface using particle image velocimetry", *Ocean Dynamics*, **58**, 58-79

Siddiqui M. H. K., Leowen M. R., Richardson C., Asher W. E. and Jessup A. T., (2001): "Simultaneous particle image velocimetry and infrared imagery of micro-scale breaking waves", *Phys. Fluids*, **13**, 1891-1903.

Siddiqui M. H. K. and Leowen M. R., (2007): "Characteristics of the wind drift layer and microscale breaking waves", *J. Fluid Mech.*, **573**, 417-456.

Stewart R. H., (1970): "Laboratory studies of velocity field over deep-water waves", *J. Fluid Mech.*, **42**, 733-754.

Takeuchi K., Leavitt E. and Chao S. P., (1977): "Effects of water waves on the structure of turbulent shear flow", *J. Fluid Mech.*, **80**, 535-559.

Townsend A. A., (1976): "The Structure of Turbulent Shear Flow", *Cambridge University Press*, Cambridge.

Veron F., Saxena G. and Misra S. K., (2007): "Measurements of the viscous tangential stress in the airflow above wind waves", *Geophysical Research Letters*, **34**, 1-5.

Volkov (1970): "Turbulent flux of momentum and heat in the atmospheric surface layer over a disturbed sea surface", *Atmospheric Oceanic Physics*, **6**, 770-774.

Wetzel S. W., (1996): "An investigation of wave induced momentum flux through phase averaging of open ocean wind and wave fields", *M. Sc. thesis*, B. S. E. Princeton University.

Willmarth W. W. and Lu S. S., (1972): "Structure of the Reynolds stress near the wall", *J. Fluid Mech.*, **55**, 65-92.

Wu J., (1975): "Wind-induced drift current", *J. Fluid Mech.* **68**, 49-70.

Appendix I

Error estimate for the PIV measurements

The total error in the PIV measurements is the sum of the errors due to gradients, particle density, particle diameter, out-of-plane motion, dynamic range, peak locking and AGW interpolation (Cowen and Monismith 1997). The non-dimensional particle diameters in the present study were 0.015, 0.008 and 0.005 pixels/pixel for first second and third configurations respectively. Particles smaller than one pixel always occupy one pixel area in a PIV image. Therefore, the true position of the particle within a pixel cannot be resolved. Furthermore the particle diameters less than one pixel also increases the peak locking errors. Peak locking refers to the bias that occurs when the estimated location of the correlation peak is shifted towards the nearest integer value. According to Fincham and Spedding (1997) peak locking occurs in any type of Image Velocimetry technique where sub-pixel determination of the correlation peak is attempted. However, it can be minimized by using a suitable peak-fitting scheme. Cowen and Monismith (1997) tested several different sub-pixel peak fitting schemes including the three-point Guassian, parabolic and center-of-mass estimators and found that the three-point Guassian estimator performed the best.

The largest errors are expected to occur in the top 2 cm layer of air at the highest wind speeds since the velocity gradients are largest here. We used the results of Cowen and Monismith (1997) and Prasad et al. (1992) to estimate the error in the PIV data. The errors were estimated for all three configurations separately, using the raw displacement

data in the top 2 cm layer of air at the wind speed of 4.4 m s^{-1}. A detailed step-by-step procedure to estimate errors in the PIV data in the first configuration is given below.

1. The mean values of the largest velocity gradients in the stream wise and vertical direction were computed from the raw PIV data. For all three configurations, the largest mean velocity gradient was $\frac{\partial u}{\partial y}$ with the value of 0.307%. Thus this gradient was used to estimate the errors in the streamwise velocities of each configuration.

2. The errors due to velocity gradient were estimated using figure 5(e) in Cowen and Monismith (1997). This figure gives the approximate error due to velocity gradients and is based on a particle size of 2.0 pixels. The total error due to velocity gradients is the sum of the mean and RMS errors. The errors due to velocity gradient were estimated to be,

$$\varepsilon_u = 0.06 pixels \tag{A.1}$$

where ε_u is the error associated with the streamwise velocity.

3. As mentioned earlier, for the first configuration, the particle diameter in the present study was 0.0154 pixels therefore the error due to smaller particle diameter should be accounted for. We used figure 5(a) in Cowen and Monismith (1997), which is the plot of the errors as a function of the particle size. The errors due to the particle diameter of 1.0 pixel were estimated, since this was the smallest particle diameter that Cowen and Monismith (1997) was considered. The errors for a particle diameter of 1.0 pixel and the same velocity gradients were,

$$\varepsilon_u = 0.2 pixels \tag{A.2}$$

4. The errors corresponding to the particle diameter of 0.015 pixels were estimated using figure 13 in Prasad et al. (1992), which shows the variation in the bias (peak locking error) and RMS errors as a function of particle diameter. Using this figure, we estimated that the errors associated with a particle diameter of 0.015 pixels would be 20% larger than the errors associated with a particle diameter of 1.0 pixel. The estimates of Prasad et al. (1992) were based on a center of mass peak-fitting scheme, which is the scheme most susceptible to peak-locking errors (Fincham and Spedding 1997). The errors in the present case would be smaller since we used a three-point Gaussian estimator, which is much less susceptible to peak locking than the center of mass scheme (Cowen and Monismith 1997). Therefore, a more realistic estimate of the increase in the error is 20% due to the small particle size. hence, the final error estimate based on a 20% increase in errors was,

$$\varepsilon_u = 0.0713 pixels \tag{A.3}$$

5. The in-plane vertical displacement based on the mean and standard deviation of the vertical displacement was estimated to be,

$$v = \bar{v} + \sigma_v = 0.232 pixels \tag{A.4}$$

The out-of-plane motion was expected to be less than or equal to the vertical displacement. Since the thickness of the laser light sheet was approximately 200 μm, the out-of-plane motion in the present case was assumed to be negligible.

6. The error due to AGW interpolation was estimated from figure 5(f) in Cowen and Monismith (1997) and it was 0.08 pixels.

Thus the total error in the streamwise velocity was estimated to be,

$$\varepsilon_u = 0.0713 + 0.08 = 0.15125 pixels \tag{A.5}$$

We assumed that the errors in the vertical velocity (v) were the same as the error in the streamwise velocity (u). Since the larger gradients in the vertical direction (i.e. $\partial u / \partial y$) will produce errors in both u and v. Therefore, the error in V, where $V = \sqrt{u^2 + v^2}$ is,

$$\varepsilon_V = 2.38 pixels \tag{A.6}$$

Hence, the average RMS error in the velocity estimates is $\pm$2.38 pixels. The uncertainty in the velocity measurements was calculated by dividing the RMS error with the resultant (V) of the mean velocity components u and v in the measurement region and found to be 7%. The same procedure was addopted for the second and third configurations and the uncertainty in the velocity measurement was found to be 5% and 6% respectively.